Technische Universität München

Physik Department

MPQ

Electric Trapping and Cooling of Polyatomic Molecules

Martin G. W. Zeppenfeld

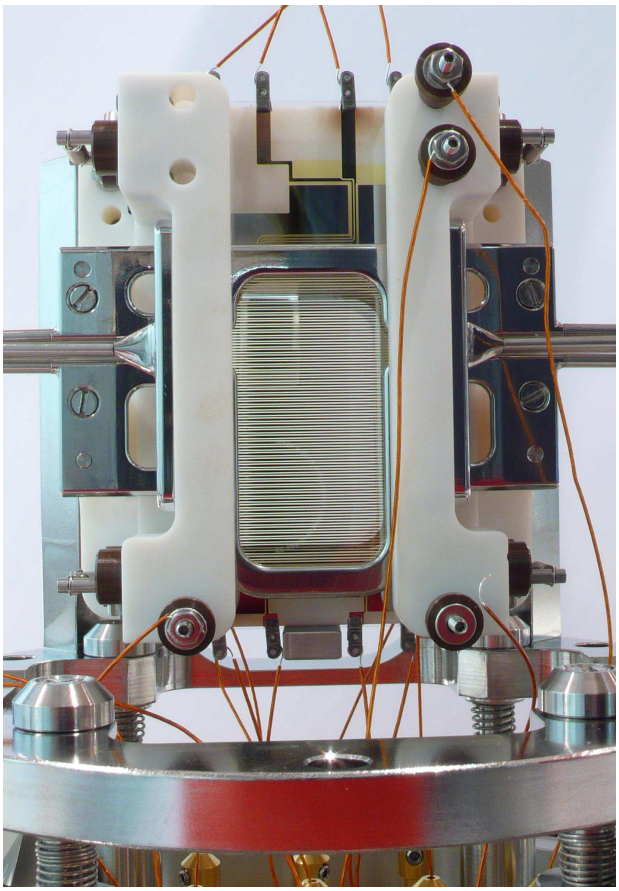

Dissertation

Max-Planck-Institut für Quantenoptik, Garching
und Physik Department, Technische Universität München

September 2013

Technische Universität München
Max-Planck-Institut für Quantenoptik

Electric Trapping and Cooling of Polyatomic Molecules

Martin G. W. Zeppenfeld

Vollständiger Abdruck der von der Fakultät für Physik der Technischen Universität München zur Erlangung des akademischen Grades eines

Doktors der Naturwissenschaften (Dr. rer. nat.)

genehmigten Dissertation.

Vorsitzende(r) :		Univ.-Prof. Dr. W. Zwerger
Prüfer der Dissertation :	1.	Hon.-Prof. Dr. G. Rempe
	2.	Univ.-Prof. Dr. R. Kienberger

Die Dissertation wurde am 12.09.2013 bei der Technischen Universität München eingereicht und durch die Fakultät für Physik am 14.11.2013 angenommen.

Abstract

Ensembles of cold and ultracold molecules promise fascinating applications, from quantum information to the investigation of fundamental physics. One approach to cool molecules to the desired temperature is optoelectrical Sisyphus cooling. Here, state-dependent potentials for molecules are produced by spatially varying electric fields in a trap. By optically pumping molecules from weakly trapped states to strongly trapped states near the center of the trap and from strongly trapped states to weakly trapped states near the edge of the trap, the energy of an ensemble of molecules can be reduced.

The work culminating in this thesis spanned the entire developement of opto-electrical Sisyphus cooling, from the conception of the original idea (preceded by the investigation of several alternative approaches) to the experimental realization. This thesis focuses on two aspects of this work. First, a key element in the successful implementation of optoelectrical cooling was the developement of a novel electric trap for polar molecules. This trap combines several features. First, molecules can be continuously loaded and accumulated from an electric quadrupole guide. Second, trap losses are reduced to the point where trap lifetimes achieved for previous electric traps are exceeded by over an order of magnitude. Third, homogeneous electric fields are achieved in a large fraction of the trap volume which is crutial for the targeted manipulation of internal molecular states. Achieving these features required a highly complex trap design which is described in detail.

The second focus of this thesis is on the original experimental results for optoelectrical cooling obtained with CH_3F molecules in the rotational states $|K| = 2,\ J = 2, 3$. This is in contrast to the results ultimately published which were obtained with molecules in the rotational states $|K| = 3,\ J = 3, 4$. In the second case, several times larger signals were obtained due to larger Stark shifts, additional rotational sublevels, and a factor of two higher hyperfine degeneracy. We were nonetheless able to obtain irrefutable evidence for cooling with molecules in $|K| = 2$ states. As these results are otherwise likely to remain unpublished, they are included in this thesis.

Contents

Chapter 1

Introduction

Predicting and controlling the behavior of physical systems lies at the heart of physics. For this purpose, performing experiments at reduced temperatures has proven to be a highly versatile technique. Fundamentally, low temperature means that a given change in thermal energy of a system must be accompanied by a large change in entropy. The most direct consequence of this is that at lower temperatures, less thermal energy is available. This results in benefits such as reducing thermal fluctuations or slowing down the velocity of a thermal beam of particles, allowing it to be observed more precisely.

The greatest benefits of lower temperatures, however, originate from the combination with quantum mechanics. For a two level system with some energy separation, the increase in entropy from populating both levels equally compared to populating only one level is a fixed amount, $k_B \ln 2$. As a result, for sufficiently low temperature, the entropy gain from populating the upper level no longer compensates the thermal energy required to do so, and the system becomes confined to the lower level. Extended to larger systems, this effect ensures that any finite system is confined predominantly to the absolute ground state for a sufficiently low temperature. While this temperature is unobtainably low for sufficiently large systems, individual degrees of freedom generally become frozen, i.e. confined to their lowest level, at much higher temperature. Thermal fluctuations for frozen degrees of freedom are eliminated entirely. Moreover, frozen degrees of freedom no longer play a role in the dynamics of the system, often leading to simplifications which allow a system to be understood and controlled in the first place.

The freezing of the degrees of freedom of a system at low temperature not only affects the internal states but also the translational motion. Thus, for sufficiently low energy, collisions and chemical reactions between particles can be described as involving a single partial wave, representing unsurpassable quantum control of the process. Moreover, the three probably most well known phenomena at low temperatures, superconductivity, superfluidity and Bose-Einstein condensation, are all manifestations of the motion of each of an ensemble of particles being predominantly confined to a single quantum state.

Exploring low temperatures is taken to the extreme in the field of ultracold atoms, where temperatures below 1 nK have been reached [1]. Here, techniques such as laser cooling and optical pumping have resulted in unprecedented quantum control over atomic systems.

This is of course exemplified by the generation of the first Bose-Einstein condensate in an ensemble of Rb atoms in 1995 [2], but also, for example, by the isolation in the absolute motional ground state and a single internal state of individual atomic ions [3], and more recently, of individual neutral atoms [4, 5].

The extreme control which has been attained over ensembles of atoms has motivated substantial effort to obtain similar control of other forms of matter. A first example is the investigation of micromechanical oscillators coupled to electrical or optical devices [6, 7]. Here, a major recent success was the cooling of an optically coupled oscillator to the lowest vibrational level via sideband cooling [8]. As a second example, the promise of quantum computing with quantum controlled matter has motivated the development of various types of "artificial atoms", solid state systems allowing coherent manipulation in a discrete set of quantum levels [9]. In contrast to real atoms, artificial atoms are very flexible concerning the properties of the quantum levels and might easily be scaled to large systems in analogy to integrated circuits.

A third example for extending quantum control of matter beyond atoms, which is the focus of this thesis, is the field of cold and ultracold molecules. In basically all ways but one, molecules have the same favorable properties that make atoms into such versatile tools to explore low temperature physics. In particular, molecules are also sufficiently simple to in principal allow full quantum control over all degrees of freedom. Moreover, molecules can easily be isolated from the environment and also possess a wide range of internal states which can be used for their manipulation. Concerning the last point, molecules in fact substantially exceed atoms, having vibrational and rotational degrees of freedom which atoms lack. A second advantage compared to atoms is the existence, for polar molecules, of a strong permanent electric dipole moment. This results in strong long-range state-dependent interactions between individual molecules as well as strong interactions with microwave or DC electric fields. As a result of these properties, cold molecules offer a wide range of fascinating applications, ranging from controlled chemistry to precision measurements for fundamental physics. This is discussed in detail in the next section.

Compared to atoms, molecules have one key disadvantage, the lack of closed optical cycling transitions. Such transitions constitute the simplest means to achieve entropy dissipation for atoms at low temperature, and are the key ingredient for the principal technique to create cold atoms: laser cooling. With the workhorse method to produce cold atoms out of the question for all but a select few molecule species with nearly closed optical transitions [10], a wide variety of alternative techniques to produce cold molecules have been developed in the past 15 years. An overview of these methods is provided in section 1.2. In particular, the work performed for this thesis focused on the design and implementation of one such method, opto-electrical Sisyphus cooling.

1.1 Applications of cold and ultracold molecules

1.1.1 Cold and ultracold chemistry

Low temperatures provide fascinating opportunities to study chemistry [11, 12]. At warm temperatures, reactions typically take place via a large number of reaction channels, starting from a large number of internal and motional states. This causes features such as reaction resonances to be smeared out, hindering their observation. In contrast, at low temperature reaction resonances have been predicted to occur for a number of systems [13, 14, 15]. A further possibility at low temperature is to control chemical reactions using external fields [16]. This includes manipulating centrifugal barriers to vary reaction rates and shifting reaction resonances.

To date, a number of collision and reaction experiments have been performed with cold molecules. For example, collisions between Stark decelerated OH with all the noble gases as well as with D_2 and NO have been performed [17, 18]. These experiments are particularly interesting in that state sensitive detection of the reaction products allows the onset of various inelastic collision channels to be observed as a function of collision energy. Sawyer *et. al.* observed losses of trapped OH molecules from scattering with a beam of He atoms or D_2 molecules [19]. Parazzoli *et. al.* observed losses of trapped ND_3 molecules from collisions with trapped Rb atoms [20]. Strebel *et. al.* measured scattering cross sections of decelerated SF_6 with Li atoms in a MOT [21]. Henson *et. al.* measured resonances in Penning ionization reactions between beams of metastable He (^{3}S) and H_2 [22]. In this last experiment, extremely high millikelvin energy resolution was achieved by merging the beam of He atoms with the H_2 beam using a magnetic guide.

A variety of cold chemistry experiments have been performed with trapped ions. Due to the long trapping times which can be achieved for ions, extremely low reaction rates can be observed. In a first experiment, reactions between trapped Ca^+ ions and velocity selected CH_3F molecules were observed by Willitsch *et. al.* [23]. This was extended to collisions with CH_2F_2 and CH_3Cl in Gingell *et. al.* [24]. Hall and Willitsch studied reactions between N_2^+ ions and Rb atoms at millikelvin temperatures [25]. Okada *et. al.* studied reactions of Ca^+ ions with CH_3CN and ND_3 molecules as well as reactions of NH_2^+ ions with CH_3CN molecules [26].

A third platform to investigate cold chemistry involves the use of associated alkali dimers. Here particularly low temperatures have been reached. However, due to the reliance on laser cooled atoms, the variety of available chemical species is very limited. Ospelkaus *et. al.* observed a difference in the reaction rate of ultracold KRb molecules in a single quantum state and in two different quantum states due to the restriction, in the first case, to p-wave scattering, with s-wave scattering only allowed in the second case [27]. Ni *et. al.* observed a change in the reaction rate of KRb molecules when applying an electric field [28]. The reaction rate of KRb was suppressed by Miranda *et. al.* by confining the molecules to a 2D geometry [29].

1.1.2 Quantum information processing

While a wide variety of systems have been suggested for implementation of quantum information processing [9], polar molecules have a number of features which might make them particularly suitable. Their strong permanent electric dipole moment results in long range interactions between individual molecules allowing quantum information to be conveniently exchanged. Moreover, molecules' rotational degrees of freedom provide long lived states which can easily be manipulated using microwave radiation.

The beneficial features of polar molecules have resulted in a number of ideas for incorporating them in quantum information processing schemes. A particularly direct approach is to confine a set of molecules in a one-dimensional array, with dipole-dipole interactions between neighboring molecules allowing qubits stored in individual molecules to interact, as has been proposed by DeMille [30]. Here, a position dependent electric field allows the molecules to be individually addressed spectroscopically. One challenge with this approach is that it requires a regularly spaced array of molecules to be generated. This might be achieved by allowing the molecules to self-assemble in dipolar crystals, as has been suggested by Ortner *et. al.* [31].

Various systems for quantum information processing have different strengths and weaknesses. This suggests the approach of hybrid quantum computing, integrating various systems so as to combine the strengths and eliminate the weaknesses. Here the strong interaction of molecules with microwave fields strongly suggests their combination with microwave devices such as resonators or superconducting qubits, as has been proposed by André *et. al.* [32]. For the molecules, this results in benefits such as providing a means to cool them and a means for their non-destructive state-sensitive detection. In addition to individual molecules [32], ensembles of molecules might be coupled to microwave devices collectively, resulting in a dramatically increased coupling strength [33]. Alternatively, molecular ions might also be used [34].

For quantum information processing schemes based on atoms, each atom (or sometimes an entire ensemble of atoms) encodes one qubit, and coupling individual qubits requires coupling individual atoms. For molecules with their large number of internal degrees of freedom, this is not necessarily the case. In fact, Tesch and de Vivie-Riedle have suggested using a single molecule as an entire quantum computer [35]. Here, the qubits are composed of individual vibrational degrees of freedom. Qubit operations are implemented via shaped femtosecond laser pulses. A first step in this direction has been achieved experimentally by Hosaka *et. al.* by implementing a classical Fourier transform with a single molecule [36].

For many quantum information schemes, using symmetric top molecules rather than linear molecules can result in substantial benefits [37]. For example, symmetric top molecules possess large linear Stark shifts with dipole moments which are nearly field independent over a wide range in field strength. This is particularly relevant in the context of this thesis since the method to cool molecules which we describe herein is particularly suited to symmetric top molecules.

1.1.3 Precision measurements

The high level of control achieved with ultracold atoms has resulted in measurements of unsurpassed precision. Thus, atomic clocks with a stability of almost one part in 10^{18} have been demonstrated [38]. In addition to metrology, a key application of such precise measurements is to test fundamental physical theories. Here, one example is the search for an electric dipole moment of the electron (eEDM). Such a dipole moment is only possible via a violation of time reversal symmetry. While the standard model of particle physics predicts a value for the eEDM far below the sensitivity of current experiments, various extensions to the standard model predict substantially higher values [39]. The search for the eEDM thus allows TeV physics to be investigated at sub-meV energies.

Until recently, the most precise limits on the value of the eEDM were achieved with atoms [40]. However, for such tests, molecules have a number of intrinsic advantages [41]. In particular, an observable effect of the eEDM in an atom or molecule requires a preferably large admixture of s and p orbitals [41]. Such an admixture is automatically present in molecules due to the chemical bonds. A second advantage is that the energy level structure of molecules allows systematic effects to be more easily controlled [42].

A first measurement of the eEDM using molecules was performed in 2002 [43], and the best limit on the size of the eEDM is based on measurements using molecules as of 2011, resulting in a value of $|d_e| \lesssim 10^{-27}\,\mathrm{e\,cm}$ [44]. In the near future, improvements should allow this limit to be further reduced by several orders of magnitude [45, 46]. Measurements of the eEDM thus complement measurements in the Large Hadron Collider at CERN for ruling out parameter space for theories beyond the standard model.

1.2 Methods for producing cold and ultracold molecules

The fascinating applications of molecules at low temperatures have motivated the development of a variety of techniques to produce ensembles of cold molecules. These techniques can be divided into two categories, the so-called direct and indirect cooling methods. Direct cooling consists of taking the molecule species of interest and cooling it to the desired temperature. Indirect cooling consists of taking the constituent atoms of the molecule species of interest, cooling them to the desired temperature, and then assembling them into molecules.

1.2.1 Indirect cooling methods

Creating cold molecules from cold atoms is complicated by fundamental physical considerations. Specifically, for a two-particle process, conservation of energy and momentum forbids the creation of a stable bound state. Creating a bound state therefore typically involves a third particle to remove the binding energy in the form of kinetic energy. However, the kinetic energy of the third particle is accompanied by some momentum which is imparted equally but oppositely on the newly created bound particle. The temperature of the bound particle is thus increased, contrary to the desire to create cold molecules.

Eliminating binding energy while keeping heating to a minimum can be achieved by using photons. This is due to the huge ratio for photons between their kinetic energy and their momentum. This idea is realized in photoassociation. Here, atoms approaching each other sufficiently closely are transferred to a bound state on the potential energy surface of the electronically excited state using a laser. To form stable molecules, this must be followed by deexcitation to a bound state on the potential energy surface of the electronic ground state. This is possible either by spontaneous decay or via stimulated emission using a second laser. Photoassociation was first demonstrated to create cold Cs_2 molecules by Fioretti *et. al.* [47].

A second approach to create cold molecules is via Feshbach resonances. Here, molecules are in fact created using a two-body process. While this is unable to create stable bound states directly, the creation of short-lived unstable bound states is not excluded. Such short-lived states are populated when their energy precisely corresponds to the collision energy of the colliding particles, resulting in a so-called Feshbach resonance in the scattering length. An unstable bound state can be converted into a stable bound state if its energy can be shifted below the dissociation threshold. This is the case, for example, when the bound state and the unbound state have different magnetic moments, allowing a magnetic field to be used.

For both photoassociation and Feshbach association, molecules are created in highly excited states. For Feshbach association, this is clear from the molecules being created near the dissociation threshhold. For photoassociation, a sufficient overlap of the wavefunction for the atoms in the bound state with free atoms must exist. This is only the case for highly excited bound states. For applications, ensembles of molecules in their absolute vibrational ground state are often desired. This can be achieved using coherent state transfer, as was demonstrated by Ni *et. al.* to achieve a near quantum-degenerate gas of polar KRb molecules [48]. Ground-state molecules can also be obtained via internal state cooling. This has demonstrated for Cs_2 molecules for both vibrational [49] and rotational cooling [50].

1.2.2 Direct cooling methods

While indirect production of cold molecules benefits from several decades of experience in cooling atoms, this is less the case for the direct cooling methods which more directly make use of properties unique to molecules. For example, the strong interaction of polar molecules with DC electric fields plays a key role in velocity filtering, probably the simplest technique to create cold molecules. Here, the basic idea is that also at warm temperatures, the thermal Boltzmann distribution contains a certain fraction of molecules which are moving slowly. These slow molecules can be separated from the fast molecules with an electric guide to create an ensemble of cold molecules, as was first demonstrated by Rangwala *et. al.* [51].

In theory, velocity filtering can result in huge numbers of cold molecules. Thus, at standard temperature and pressure, the density of a molecular gas is approximately $3 \times 10^{19}\,\mathrm{cm}^{-3}$, a fraction of about one in 5000 of which is slow enough to be at a tempera-

ture below 1 K. This would theoretically allow a density of cold molecules of $6 \times 10^{15}\,\mathrm{cm}^{-3}$ to be achieved. In practice, the slow molecules must be separated from the fast molecules on a timescale comparable to the average time between collisions. This requires a substantially lower pressure and is achieved by injecting molecules into an electric guide using a nozzle operated in the effusive regime. The conditions to achieve optimal signal have been investigated in Motsch *et. al.* [52].

A major disadvantage of velocity filtering is that molecules are generated in a large number of internal rotational states. Thus, the internal state distribution reflects the temperature of the molecule source with the population of individual states additionally weighted depending on their Stark shift. This has been investigated in Motsch *et. al.* [53] using depletion spectroscopy and by Bertsche *et. al.* [54] using state-selective detection.

One possibility to obtain internally cold molecules is via buffergas cooling. This was in fact the first direct cooling technique for molecules to be demonstrated, by Weinstein *et. al.* [55]. The idea of buffergas cooling is to allow molecules to thermalize via collisions with a gas of Helium atoms in a cryogenic environment. A key requirement for this to work is to prevent collisions of molecules with the walls of the cryogenic environment since the molecules stick to the walls and are thereby lost. In the original buffergas cooling experiment, this was achieved by trapping the molecules magnetically. This works because for the CaH molecules used, elastic collisions with the helium are much more likely than inelastic collisions where the molecules end up in untrapped states. Even without a magnetic trap, however, the helium can substantially reduce collisions with the walls. This is because the motion of the molecules in the helium becomes diffusive, increasing the time to travel a given line-of-sight distance.

Creating an aperture in the buffer-gas cell allows molecules to exit, forming a beam of cold molecules. This allows the molecules to be separated from the helium and allows the molecules to be extracted from the cryogenic environment. Such a beam source for molecules was first realized by Maxwell *et. al.* [56]. Patterson *et. al.* combined it with a magnetic guide [57] and van Buuren *et. al.* combined it with an electric guide [58].

To obtain slow molecules from a buffergas source or via velocity filtering from a warm source, the source must be operated in a low-density effusive regime. The opposite, high density regime is also of great interest to produce cold molecules. Here, the large number of collisions during expansion of a beam from a nozzle into vacuum results in adiabatic cooling, substantially reducing the internal temperature of the beam. During such a supersonic expansion, the thermal energy of the gas is converted into forward velocity of the beam, with forward velocities of many hundreds of meters per second.

To obtain slow molecules using supersonic expansion, a means must be found to decelerate the beam. The extremely high densities of cold molecules which can be obtained with supersonic expansion have motivated the development of a wide variety of deceleration techniques. The first technique to be demonstrated was Stark deceleration, by Bethlem *et. al.* [59]. Here, the potential energy gradient created for molecules by spatially varying electric fields is used to decelerate the beam. Since the electric field strengths which can be created in the laboratory are insufficient to remove the entire kinetic energy at once, an array of electrodes is switched such that (for low-field seeking states) the

molecules move towards an increased electric field strength most of the time.

Replacing the electric fields in Stark deceleration with other fields results in a number of analogous deceleration techniques. For paramagnetic molecules, Zeeman deceleration using switched magnetic fields is possible [60, 61]. Fulton *et. al.* have demonstrated optical deceleration using the intense field in a focused pulsed laser [62]. First results have been obtained with microwave deceleration [63].

Molecular beams can also be decelerated mechanically. This was first realized via a counter rotating nozzle by Gupta and Herschbach [64]. Strebel *et. al.* have combined a counter rotating nozzle with a static quadrupole guide [65]. An alternate approach to decelerate molecule mechanically is to use the centrifugal force on a rotating disk. This is currently being demonstrated by our group [66].

1.2.3 Extending direct cooling to ultracold temperatures

The techniques for direct cooling of molecules presented so far all reach temperatures on the order of 1 K or slightly below. For many applications of cold molecules, substantially lower temperatures ($< 1\,\mathrm{mK}$) are required. Extending direct cooling to such temperatures is a very active field of research.

A key element of any dissipative cooling technique is some process to remove entropy. Entropy exchange is of course possible via collisions between particles. Here, sympathetic or evaporative cooling to achieve ultracold temperatures with molecules is very appealing since it could maintain the extreme generality of the techniques developed to reach sub-Kelvin temperatures. Applying sympathetic or evaporative cooling to molecules has proven surprisingly difficult. In many cases, inelastic collisions or even chemical reactions lead to large losses. Despite these challenges, evaporative cooling of OH has recently been demonstrated by Stuhl *et. al.* [67].

A particularly elegant technique for the removal of entropy is via the emission of photons. This is an irreversible process whenever the temperature of the environment is sufficiently low such that the mode of the electromagnetic field into which the photon is emitted is not occupied. While using photons to cool atoms has been extremely successful, applying them to cool molecules has been quite difficult. For example, Doppler cooling requires scattering of a large number of photons, and all molecules eventually spontaneously decay to rovibrational states which are not coupled to the laser. Direct application of Doppler cooling is thus completely hopeless for most molecule species. This however by no means eliminates the possibility of using photons to cool molecules.

Starting from Doppler cooling as a reference, two general strategies seem to exist for the adaptation of laser cooling to molecules. One approach is to alter, improve or otherwise manage the spontaneous decay process and the large number of states which are thereby potentially occupied. Here, one of the earliest suggestions is to simply accept the fact that the molecules populate a large number of different internal states. Thus, Bahns *et. al.* proposed only maintaining control of a molecules rotation while applying a large number of sidebands to a laser to address all relevant vibrational states during translational cooling [68]. Weitz and Hänsch suggested using extremely short pulses to address all in-

ternal states simultaneously while using an interferometry technique to achieve a velocity dependent force [69]. Vuletić and Chu suggested using an optical resonator to enhance far off-resonant scattering of light, allowing molecules to be treated as structureless polarizable particles with the internal state being ignored [70].

Optical resonators can also be used to maintain control of rather than to ignore the internal state by enhancing a particular spontaneous decay channel. The increase in the photon scattering rate above the spontaneous decay rate by a resonator might allow slowly decaying but intrinsically closed pure vibrational transitions to be used [71]. Control of the internal state might also be maintained by throwing out the spontaneous decay entirely and applying feedback cooling, a variant of which was proposed for molecules by Averbukh and Prior [72]. Here, photons remove entropy by providing information about the system. Finally, for certain molecule species, adding just a small number of repump lasers results in a transition scheme which is sufficiently closed that direct Doppler cooling is possible [10]. This has allowed Shuman *et. al.* to substantially reduce the transverse temperature of a molecular beam [73], and progress is being made on longitudinal cooling as well [74].

A second strategy to adapt laser cooling to molecules is to improve the efficiency of the energy reduction process (as opposed to the spontaneous emission which reduces entropy) such that fewer spontaneously emitted photons are required. The potential of this approach can be appreciated by noting that the weak nature of the photon recoil in Doppler cooling results in an energy reduction per spontaneously emitted photon which is several orders of magnitude below what is theoretically possible. One approach to use spontaneous decay more efficiently than in Doppler cooling has been known for a long time for atoms in the form of Sisyphus cooling [75]. Here, the idea is to use state dependent potentials combined with optical pumping such that a particle experiences a strong force when traveling from the center of a potential well towards the edge, and a weak force when traveling back to the center.

Surprisingly, the suitability of Sisyphus cooling for cooling of molecules remained unnoticed for a long time. Thus, the only mention of Sisyphus cooling in the context of cooling molecules in the literature before 2009 seems to be by Averbukh and Prior who compare the time dependent potentials in their feedback cooling to the state dependent potential in Sisyphus cooling [72]. This was followed by our proposal of optoelectrical cooling [76] and by a proposal by Robicheaux to apply Sisyphus cooling to OH using a microwave spontaneous decay [77].

The long disregard of Sisyphus cooling as a means to cool molecules, however, did not extend to the idea of using spontaneous decay as efficiently as possible. One variation which does not lead to cooling directly but does increase phase space density is the accumulation of molecules. Here, molecules enter a trap in a state which is not trapped and are optically pumped to a state which is trapped. Accumulation of NH was proposed by Meerakker *et. al.* [78] and realized by Riedel *et. al.* [79]. A variation of accumulation which can result in cooling as well is to accumulate molecules from a large trap into a small trap near the edge of the large trap where the kinetic energy of the molecules is small. This was proposed as single photon cooling by Narevicius *et. al.* [80].

Rather than to accumulate molecules in space, molecules might also be accumulated

in terms of their velocity. Thus, Ooi *et. al.* suggested transferring a subset of an ensemble of molecules with similar velocities to a separate internal state and shifting the average velocity of this set of molecules to zero via a sequence of STIRAP pulses [81]. The process ends with a single spontaneous decay back to the initial state. This idea, that a sequence of pulses followed by a single spontaneous decay allows a spontaneous decay to be used much more efficiently in fact provided the spark for the ideas presented in this thesis.

1.3 Outline of this thesis

Realizing a project as complex as optoelectrical Sisyphus cooling from the first idea to the experimental realization results in an almost endless supply of ideas about which to write a thesis. To nonetheless restrict the scope of this thesis to a manageable level, we focus on those topics which have not been presented elsewhere. Moreover, chapters 2 and 4 rely on existing texts. **Chapter 2** contains the original proposal for optoelectrical Sisyphus cooling, ref. [76]. This introduces the basic idea for cooling, identifies a set of molecular energy levels and transitions between them with which cooling can succeed, and provides a brief description of the microstructured electric trap in which cooling was realized.

The main part of this thesis is **chapter 3**, presenting the design of the microstructured trap in detail. A highly complex trap design allowed the combination of a number of features which were crucial for the success of optoelectrical cooling, as will be discussed. The chapter also contains an analysis of the possible loss processes in an electric trap as a well as the derivation of analytic expressions for the electric fields produced by a periodic microstructure, a key element of the trap.

In **chapter 4**, we present the original experimental results for cooling. These results were compiled into a paper and submitted for publication. However, while the paper was under review, substantially improved cooling results were obtained based on a different set of molecular states. In the end, only the improved results were published in ref. [82]. Since the original results would otherwise be likely to remain unpublished, we reproduce the original version of the paper. **Chapter 5** concludes with a discussion of ideas for the future.

Many of the topics left out of this thesis are excellently described elsewhere. Experimental results with the microstructured electric trap and additional information on the experimental setup are provided in ref. [83] and in the diploma thesis of Manuel Mielenz. Newer results for cooling are contained in ref. [82] and in the diploma theses of Alexander Prehn and Martin Ibrügger. Both the trap and the cooling results will be discussed at length in the doctoral thesis of Barbara Englert.

Chapter 2

Overview of optoelectrical cooling

In this chapter, the original proposal for optoelectrical Sisyphus cooling (ref. [76]) is presented as an introduction to the technique. The paper begins with a discussion of the basic concept of optoelectrical cooling: using state dependent potentials created by DC electric fields combined with optical pumping to reduce the energy of an ensemble of molecules. This is illustrated with a simplified version of the cooling scheme involving only three energy levels. It is argued that the cooling technique is particularly suited for molecules.

A key part of the paper is the proposal of a novel design for an electric trap in which optoelectrical cooling can take place. This design is motivated in particular by the ability to load it continuously with molecules from a quadrupole guide and the ability to apply tunable homogeneous offset fields in a large fraction of the trap volume. Achieving these features while simultaneously keeping trap losses under control requires a relatively complex trap design, the details of which will be discussed in chapter 3.

A large part of the paper is concerned with working out additional details for the experimental realization of optoelectrical cooling. For example, the relevant selection rules for molecular transitions are summarized and the energy level scheme for cooling is adapted to actual molecules. A number of molecules are suggested as possible candidates for cooling along with their most important properties. A rate equation model to describe the cooling process is developed allowing the time required for cooling to be estimated.

In the last part of the paper (excluding the appendix), various effects which might prevent the successful realization of optoelectrical cooling are considered. Thus, the cooling as proposed only reduces the velocity of the molecules in one dimension. Full three-dimensional cooling requires sufficient mixing of the velocity components. Trap loss mechanisms and transitions to unwanted states are also discussed.

The cooling scheme presented in this chapter differs from the scheme which has been experimentally demonstrated in one key respect. In the paper, we assume that transitions between a certain pair of neighboring rotational sublevels of a rotational state (e.g. between the states $|2, 2, -2\rangle$ and $|2, 2, -1\rangle$, using the notation $|J, K, M\rangle$ to label rotational states as discussed in the paper) can be driven without driving transitions between the rest of the rotational sublevels (e.g. between the states $|2, 2, -1\rangle$ and $|2, 2, 0\rangle$). In practice, this is almost impossible since all transitions between neighboring rotational sublevels of a

rotational state have almost identical differential Stark shifts for intermediate electric field strengths. One possibility to avoid this problem is to avoid transitions between rotational sublevels of a given rotational state and to replace them with transitions (for the energy levels in the paper) between $J = 2$ and $J = 3$. A second possibility, which ended up being realized in the experiment, is to drive the transitions between rotational sublevels at a slow rate compared to the rate of the spontaneous decay used for optical pumping (see chapter 4 for details). A major disadvantage of this approach is that it substantially increases the time required for cooling. However, since the homogeneity of the electric field in the high-field region is no longer important, the high-field region can be eliminated. This eliminates the slow down in cooling associated with molecules needing to travel between the two trap regions and results in three-dimensional rather than one-dimensional cooling since the high-field transitions can occur anywhere near the edge of the trap.

Publication: Optoelectrical cooling of polar molecules

M. Zeppenfeld, M. Motsch, P.W.H. Pinkse, and G. Rempe
published in Phys. Rev. A **80**, 041401(R) (2009)

We present an opto-electrical cooling scheme for polar molecules based on a Sisyphus-type cooling cycle in suitably tailored electric trapping fields. Dissipation is provided by spontaneous vibrational decay in a closed level scheme found in symmetric-top rotors comprising six low-field-seeking rovibrational states. A generic trap design is presented. Suitable molecules are identified with vibrational decay rates on the order of 100 Hz. A simulation of the cooling process shows that the molecular temperature can be reduced from 1 K to 1 mK in approximately 10 s. The molecules remain electrically trapped during this time, indicating that the ultracold regime can be reached in an experimentally feasible scheme.

The ability to prepare samples of ultracold molecules opens up exciting new possibilities in physics and chemistry, including ultrahigh-precision molecular spectroscopy and interferometry [84, 85], investigations of anisotropic collisions in quantum-degenerate gases [86], steering of chemical reactions [16], tests of fundamental physics such as the search for the electron dipole moment [43], and novel approaches to quantum computing and quantum simulations [35, 30, 87]. Reaching ultracold temperatures through laser cooling has the great advantage that it does not lead to particle loss and that it is a single-particle process which does not require suitable collision properties or high densities. However, laser cooling has so far only been demonstrated for atoms and ions with simple energy-level structures, whereas optical cooling of molecules has proven confoundingly difficult.

Optical cooling of molecules requires a change in paradigm: In contrast to ultracold atoms, for which efficient cooling was realized early on [88] but trapping proved to be a challenge due to the shallow optical and magnetic potentials available, electric trapping of polar molecules is relatively easy [89] and has, in fact, been demonstrated for molecules without any cooling [90]. Optical cooling of molecules could therefore start with trapped molecules and exploit the tremendous ($\sim$1 K) energy-level shifts producible by laboratory electric fields, circumventing the usual requirements of standard laser cooling such as highly closed transitions, fast decay rates, and significant photon momentum transfer.

Making use of the aforementioned paradigm shift we here present a cooling scheme for molecules which is conceivable with present technology. Specifically, we replace photon recoil by an electric-field interaction energy as the means to remove energy from a molecular ensemble in a configuration reminiscent of Sisyphus cooling and single-photon cooling [75, 91, 92]. Spontaneous emission of photons serves only to remove entropy. As a result, the number of scattered photons required to achieve substantial cooling is dramatically reduced. Slowly decaying vibrationally excited states, generally offering stricter selection rules than electronic transitions, can therefore be used for the spontaneous decay.

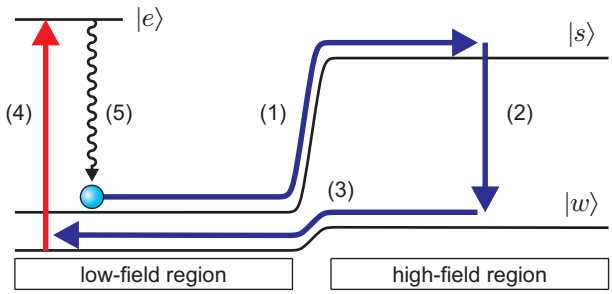

Figure 2.1: Energy-level and state-transition diagram for the cooling scheme. A molecule in the strong lfs state $|s\rangle$ diffuses from the low-field region to the high-field region (1) where it is driven to the weak lfs state $|w\rangle$ (2). After moving back to the low-field region (3), the molecule is driven to the excited state $|e\rangle$ (4) from which it decays spontaneously to $|s\rangle$ (5). The irreversible spontaneous decay makes this cycling process unidirectional.

Our cooling scheme is shown in Fig. 2.1. Two neighboring regions in space, each with a constant but different electric field, are realized by a suitable arrangement of electrodes. These electrodes also provide a high-electric-field enclosure around these regions to ensure trapping of molecules in low-field-seeking (lfs) states. Fig. 2.2 shows a possible design for the electrodes. Trapped molecules experience a potential step when moving from one region to the other. The magnitude of this potential step depends on the average orientation of the electric dipole moment of a molecule with respect to the electric field and may vary significantly for different molecular states. For one strong and one weak lfs molecular state we obtain a potential as a function of position as depicted by the curves $|s\rangle$ and $|w\rangle$ in Fig. 2.1.

Suppose a molecule possesses an excited state $|e\rangle$ which decays into the states $|w\rangle$ and $|s\rangle$. We induce transitions between $|w\rangle$ and $|e\rangle$ in the low-field region of the trap and transitions between $|s\rangle$ and $|w\rangle$ in the high-field region. Doing so creates a unidirectional cycling process. During the cycle, the molecule loses a kinetic energy corresponding to the difference between the potential steps of the strong and the weak lfs state, leading to overall cooling.

The main advantage of this cooling scheme is the large amount of kinetic energy which can be removed from a molecule for each spontaneously emitted photon. For a representative dipole moment $\mathbf{d}_{el}$ of 1 Debye [D], oriented in an electric field $\mathbf{E}$ of 100 kV/cm, one obtains an interaction energy of $\mathbf{d}_{el} \cdot \mathbf{E} = \frac{3}{2} k_B \times 1.61\,\mathrm{K}$. Starting with an ensemble of molecules with a translational temperature below 1 K, this in principle allows the removal of all of a molecule's kinetic energy in a single step. In practice, however, more than one spontaneous decay is necessary to cool a molecule: When the fields are kept constant, a molecule will generally end up in state $|s\rangle$ in the low-field region with insufficient energy to move back to the high-field region but with at least the amount of energy obtained when moving from the high- to the low-field region in the state $|w\rangle$. Further cooling to lower temperatures therefore requires the height of the electric-field step to be slowly ramped down, allowing the cooling cycle to repeat. Nonetheless, a few dozen spontaneous decays

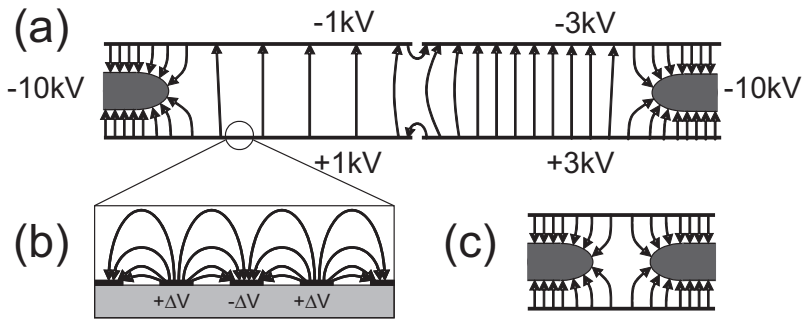

Figure 2.2: Design of an electric trap for the cooling scheme. Regions of tunable homogeneous fields are achieved using parallel capacitor plates (a). Collisions with the plate surface are eliminated by alternatingly-charged microstructured surface electrodes [93] (b). Transverse confinement is achieved by a high voltage electrode between the plates around the perimeter of the trap (a). By interrupting the perimeter electrode, an electric quadrupole guide can be connected to the trap for the injection and extraction of molecules [90] (c).

are more than enough to cool a molecule to below a mK.

Due to the small number of spontaneous photon emissions, the requirements imposed on the emission process are much less stringent than for standard laser cooling. Not only is the branching ratio for decay from the excited state to desired and undesired states much less critical, but the rate at which such transitions occur may also be much lower. As a result, the use of vibrational transitions for the spontaneous decay process is possible.

The advantage of vibrational compared to electronic excitations is that except in the case of strong resonances with other vibrational states, a molecule with one quantum of excitation in a single vibrational mode will decay primarily back to the vibrational ground state. Additionally, compared to the deep ultraviolet wavelengths required to excite electronic states of most simple chemically-stable molecules, many molecules have strong vibrational transitions in the wavelength range $3-10\,\mu$m. The coverage of this wavelength range by tunable narrow-band light sources has been significantly improved in recent years by the commercial availability of quantum-cascade lasers and optical parametric oscillators, in addition to, e.g., lead-salt lasers.

Beyond the closed vibrational transition, the rotational transitions must be considered. The excited vibrational state must not only decay to a manageable number of rotational states, but each of these states must be lfs so that the molecule remains trapped. Disregarding linear molecules due to their generally weaker quadratic Stark interactions, symmetric-top molecules have the most stringent selection rules for dipole transitions. Describing the rotational states of a symmetric-top molecule by the quantum numbers for the total angular momentum J, the angular momentum about the molecule's symmetry axis K and the angular momentum about a lab-fixed axis M, the selection rules for a parallel transition are $\Delta J = 0, \pm 1$, $\Delta K = 0$ and $\Delta M = 0, \pm 1$ [97]. Furthermore, the lowest-order Stark interaction is $E_{\text{Stark}} = -\mathbf{E}\cdot\mathbf{d}_{el} = -|\mathbf{E}||\mathbf{d}_{el}|\frac{KM}{J(J+1)}$. Observing that $J \geq 0$, $|K| \leq J$ and $|M| \leq J$ [97], we see that an excited state with $|K| = J \geq 2$ and $M = -K$ best satisfies

molecule	d_{el} [D]	f_{vib} [cm^{-1}]	γ [Hz]	molecule	d_{el} [D]	f_{vib} [cm^{-1}]	γ [Hz]
CFH_3	1.85	2964	*37*	CF_3Cl	0.50	1105	*73*
CF_3H	1.65	3036	*65*	CF_3Br	0.65	1089	*74*
CH_3CCH	0.78	3334	*87*	CF_3I	0.92	1080	*61*
CF_3CCH	2.36	3327	*79*	BH_3CO	1.80	*2217*	*274*
$N(CH_3)_3$	0.61	*2933*	*200*				

Table 2.1: An overview of symmetric-top molecules with strong parallel vibrational transitions with permanent dipole moment d_{el} [94], transition frequency f_{vib} [95], and spontaneous decay rate γ. The italicized values were obtained using the quantum-chemistry package `Gaussian` [96]. We have successfully produced a cold sample of each of the molecules on the left using our quadrupole guide [51]. Note that the large hyperfine splitting in CF_3Cl, CF_3Br, and CF_3I complicates the straightforward application of the present scheme to these molecules.

the conditions stated above. Such a state may decay into a total of only five rotational states, all of which are lfs. These can be repumped using additional lasers or microwave fields. Note that the condition of few decay channels to purely lfs states can also be satisfied for linear molecules, e.g., in a Σ electronic state using a vibrationally excited state with $M = 0$, $J \geq 3$ [97].

Use of vibrational excitations for opto-electrical cooling requires molecules with a sufficiently fast vibrational spontaneous decay rate. Table 2.1 lists promising symmetric-top molecules. Although a decay rate of $\sim 100\,\text{Hz}$ is glacial relative to decay rates used for laser cooling of atoms, it is adequate considering the small number of decays needed for the scheme presented here. Nonetheless, the spontaneous decay rate raises the question how fast opto-electrical cooling progresses. This is studied by numerically solving rate equations for cooling of CF_3H. The rate equations and their derivation are included in the appendix. The first excitation of the C-H stretch mode at $3036\,\text{cm}^{-1}$ in the rotational state $J = K = -M = 2$ is used as the excited state. The fact that this state spontaneously decays to five v= 0 states (v being the vibrational quantum number) necessitates a somewhat more complicated transition scheme than the one shown in Fig. 2.1. Specifically, we simulate cooling using the transition scheme shown in Fig. 2.3. The IR transition as well as each of the microwave transitions are driven with a rate of 10 kHz. Assuming a Stark-broadening of 10 MHz, this would require narrow-linewidth sources with an intensity on the order of $1\,\text{mW/cm}^2$ for all the transitions involved. Spontaneous decay from the excited state is modeled using a rate of 65.2 Hz, partitioned among the states with v= 0 based on rigid-rotor dipole-transition matrix elements [97]. The volumes of both trap regions are set to $100\,\text{mm}^3$, connected by an area of $10\,\text{mm}^2$.

At time $t = 0$, molecules are distributed among the states v= 0 in both trap regions with a $v^2\,dv$ velocity distribution up to a cut-off velocity of 11.7 m/s. This is the maximal trappable velocity of the involved states due to higher-order Stark shifts. The electric-field-strength difference between the two trap regions is a free parameter which is varied

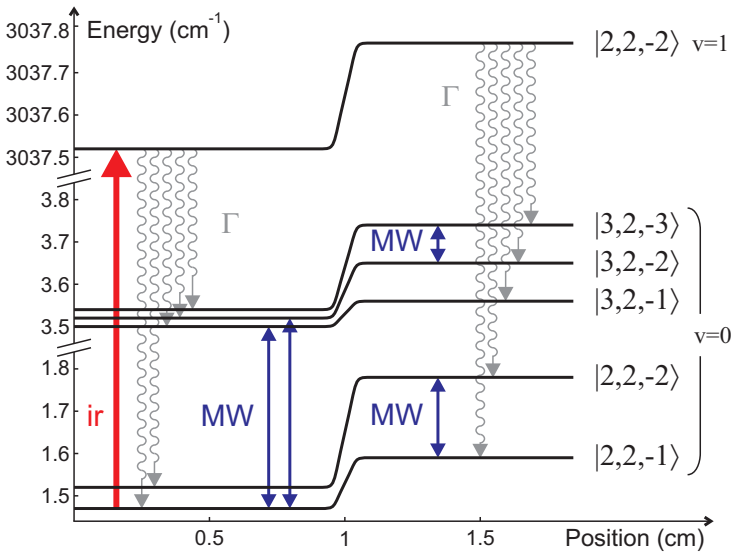

Figure 2.3: Transition scheme used to simulate cooling of CF_3H. Rotational states are labeled using the notation $|J, K, M\rangle$. MW and ir denotes the induced microwave and infrared transitions. Γ denotes spontaneous decay to the five states with vibrational excitation v= 0. The energy levels are obtained by diagonalizing the rigid-rotor Hamiltonian for CF_3H at field strengths of 5 kV/cm and 20 kV/cm for the low-field and high-field region, respectively.

as a function of time to be proportional to the 80th percentile of the kinetic energy of the molecules. The potential-energy step for each of the molecular states is modeled using the first-order Stark shift E_{Stark}.

The rate of the cooling process is influenced by three effects. Most significantly, the rate coefficients indicate the time in which $1 - 1/e$ of molecules perform some process, whereas the time in which 99% of molecules perform this process takes significantly longer. Ramping down the electric-field step too rapidly therefore causes the final energy of most molecules to substantially exceed the field-step energy so that efficient cooling is no longer possible. Secondly, the fraction of energy removed during each cooling cycle is below unity. Reducing the temperature by, e.g., a factor of ten requires several cooling cycles. Finally, spontaneous decay to the states $|2, 2, -1\rangle$, $|3, 2, -1\rangle$, and $|3, 2, -2\rangle$ in the low-field region of the trap has no net effect, reducing the effective decay rate.

The velocity distribution of the molecules in the low-field region of the trap for various times after cooling commences is shown in Fig. 2.4. As can be seen, significant cooling occurs in under a second. Note that the cooling rate decreases significantly as time progresses. For high temperatures, the cooling rate is limited by the decay rate of the vibrationally excited state, allowing the temperature to decrease exponentially with time. For low temperatures, the cooling rate is limited by the time it takes for the molecules to move between the two regions of the trap, with the cooling rate proportional to the velocity of the molecules. Therefore, at very low temperature the cooling process is no

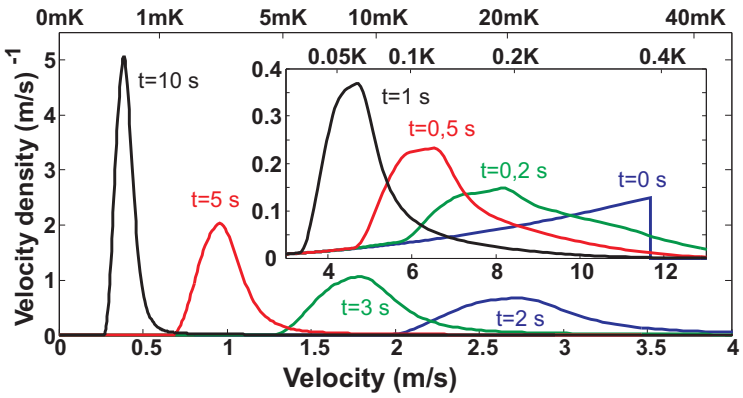

Figure 2.4: Velocity distribution in the weak-field region of the trap after cooling for a time t. Velocities are converted to temperatures according to $\frac{m}{2}v^2 = \frac{3}{2}k_BT$. Monitoring the population in the excited state during the cooling process shows that on average a molecule spontaneously decays 4.7× during the first second, 17.0× during the first 5 seconds, and 9.0× during the next 5 seconds.

longer efficient, and the molecules must either be moved to a smaller trap or a different cooling scheme must be applied.

The elementary description of opto-electrical cooling so far glosses over several issues which must be addressed to ensure the experimental viability of the method. In particular, achieving required trapping times, sufficient mixing of the individual velocity components, and validity of approximate selection rules are now discussed.

In addition to collisions with the background gas, Majorana flips and rovibrational heating by thermal blackbody radiation are the identified loss channels for polar molecules stored in electric traps [98, 99]. Although rotational heating is a problem for extremely light molecules [99] and vibrational heating for heavy molecules, neither is the case for the molecules considered in table 2.1. For example, the heating rates to the lowest vibrational modes never exceed a few mHz at 300 K for CF_3CCH, the heaviest molecule in table 2.1.

Majorana flips are expected to have been a problem in past trap designs with a near-zero electric field in the central trap region [98]. However, the trap in Fig. 2.2 is specifically designed to allow a homogeneous offset field throughout the vast majority of the trap volume. Furthermore, field zeros near the edges of the trap can be reduced to singular points through clever electrode design, which essentially eliminates Majorana flips.

Opto-electrical cooling only removes energy from a single component of the velocity vector, making sufficient mixing of the velocity components a necessity. Electric-field inhomogeneities near the microstructured plate surface allow such mixing on a sufficiently short timescale. This is demonstrated by trajectory simulations discussed in the appendix.

The zero-field rigid-rotor harmonic-oscillator selection rules used so far imply a closed six-level system for opto-electrical cooling. These selection rules are modified in several ways for real molecules. Transitions with $\Delta K \neq 0$ and decay to other excited vibrational states are generally possible for symmetric top molecules via resonances between near-

degenerate vibrationally excited states. Due to the few spontaneous emissions needed, such couplings will at most cause problems for individual molecule species.

For non-zero values of the electric field, J ceases to be a good rotational quantum number and spontaneous decay with $|\Delta J| \geq 2$ becomes possible. The resulting consequences were checked by diagonalizing the rigid-rotor Hamiltonian for non-zero electric fields using molecular constants of CF_3H and calculating dipole transition matrix elements between the new eigenstates. Although the partitioning of spontaneous decay from the state v= 1, $|2, 2, -2\rangle$ to the five states v=0, $J = 2$ and 3 is significantly changed already at electric fields of $\sim 50\,\mathrm{kV/cm}$, the spontaneous decay to states with $J \geq 4$ remains below 1% for fields up to $100\,\mathrm{kV/cm}$. This effect on opto-electrical cooling is therefore negligible.

Achieving a temperature below 1 mK through opto-electrical cooling would allow other cooling schemes, requiring longer interaction times or higher phase-space density, to be implemented. Specifically, opto-electrical cooling can easily be extended to an accumulation scheme, for example to load molecules into a tightly confining optical dipole trap. The low temperatures and high densities thus achieved create extremely favorable starting conditions for a number of further cooling schemes such as evaporative cooling, cavity cooling, or sympathetic cooling with ultracold atoms.

Appendix: Derivation of the Rate Equations

The rate equations used to simulate cooling of CF_3H can be derived as follows. The ensemble of molecules in the trap is represented by the number of molecules $p_a^{(i)}(v,t)dv$ with velocity between v and $v + dv$ in the molecular state a in part $i = 1, 2$ of the trap. Here, $i = 1$ denotes the low-field region and $i = 2$ denotes the high-field region of the trap.

In this description of the molecular ensemble, we ignore the position of the molecules within each trap region as well as the direction of the velocity vector $\mathbf{v}$ with $v = |\mathbf{v}|$, effectively assuming instantaneous spatial redistribution of the molecules within each trap region as well as instantaneous redistribution of the direction of $\mathbf{v}$. Whereas the assumed instantaneous spatial redistribution should at most slightly affect the validity of the results of the simulation since the molecule's thermal motion will rapidly redistribute the molecules through the trap, the assumed mixing of the components of $\mathbf{v}$ is less obvious. In fact, in the case of a potential energy in the trap which is completely separable in Cartesian coordinates, no mixing of the velocity components would occur at all.

To address this question, molecule trajectory simulations in a trap based on the design in Fig. 2.2 of the paper were performed and the temporal correlation of the magnitude of the individual components of $\mathbf{v}$ was calculated. The calculated correlation for a particle with a velocity of $10\,\mathrm{m/s}$ in the homogeneous-field region of the trap is shown in Fig. 2.5. Particularly for large τ, the correlation function for v_x and v_y can be accurately reproduced by assuming a $\sim 20\,\%$ probability for the velocities to completely mix for each collision with the microstructured plate surface. This demonstrates that significant mixing of the velocity components occurs due to the field inhomogeneities near the plate surfaces. Due to the translational symmetry of the microstructures along the z-direction, this mixing

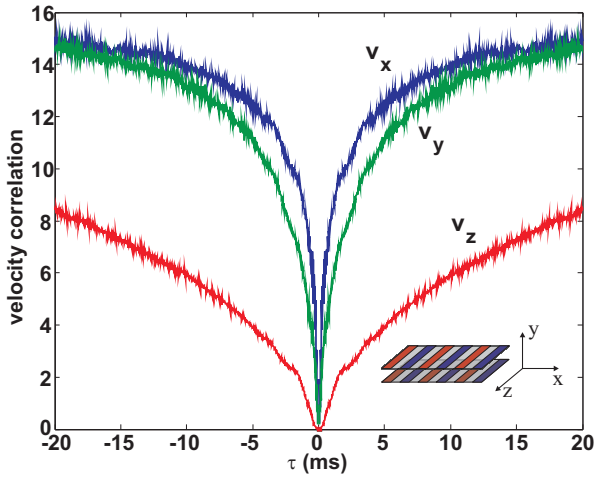

Figure 2.5: Temporal correlation $\langle(|v_i(t)| - |v_i(t+\tau)|)^2\rangle$ of the individual components of the velocity for a particle in a trap based on the design in Fig. 2.2 of the paper. The inset shows the orientation of the velocity components relative to the trap.

does not include the z-component of the velocity, leading to significantly slower mixing for this velocity component. However, by arranging the microstructure plates such that the structure on the top and bottom plate is rotated by 90 ° with respect to the other, all three velocity components mix on the shorter timescale. The resulting mixing is sufficiently strong that a major impact on the cooling rate does not occur.

To derive the rate equations for the molecule distributions $p_a^{(i)}(v,t)$, two processes must be taken into account. First, transitions between the various internal molecular states may occur in both regions of the trap. This is modeled by a fixed fraction of molecules in a given state switching to a different state per unit time interval,

$$\left.\frac{d}{dt}\right|_{\text{trans}} p_a^{(i)}(v,t) = \sum_{a'=1}^{6}(c_{a',a}^{(i)} p_{a'}^{(i)}(v,t) - c_{a,a'}^{(i)} p_a^{(i)}(v,t)), \tag{2.1}$$

with appropriate rate coefficients $c_{a,a'}^{(i)}$.

Second, molecules may diffuse between the two trap regions. For those molecules in region i with a velocity component v_x perpendicular to the interface between the trap regions, a fraction of $v_x A/V_i$ of the molecules attempt to enter the other trap region per unit time. Here, A is the surface area of the interface between the trap regions and V_i is the volume of trap region i. For those molecules in region 2 of the trap, all molecules attempting to enter region 1 succeed, whereas for molecules in region 1, only those molecules with $v_x^2 > 2\Delta E_a/m$ succeed, where ΔE_a is the potential energy difference between the two trap regions for molecules in state a and m is the molecular mass. Finally we need to average over the possible values of v_x. For an isotropic velocity distribution in three dimensions, a single velocity component is evenly distributed so that the fraction of molecules leaving

region 2 per unit time is

$$\frac{1}{2v}\int_0^v dv_x v_x \frac{A}{V_2} = \frac{v}{4}\frac{A}{V_2}, \tag{2.2}$$

and the fraction of molecules leaving region 1 per unit time is

$$\frac{1}{2v}\int_{\sqrt{\frac{2\Delta E_a}{m}}}^v dv_x v_x \frac{A}{V_1} = \frac{v_{a,2}^2}{4v}\frac{A}{V_1}. \tag{2.3}$$

Here, $v_{a,2} = \sqrt{v^2 - 2\Delta E_a/m}$ is equal to the velocity a molecule in region 1 will have once it has reached region 2. Note that the integrals are normalized by dividing by $2v$ since v_x can be both positive and negative but only molecules with (in this case) positive v_x can enter the opposite trap region.

Every molecule which leaves one trap region must enter the opposite region. Nonetheless, a complication arises since the velocity of the molecules changes when they move between the regions. Molecules which enter region 1 in state a with velocity in the range v to $v + dv$ must have had a velocity in the range $v_{a,2}$ to $v_{a,2} + v\,dv/v_{a,2}$ in region 2. As a result, the number of molecules in region 2 which could potentially increase the number of molecules $p_a^{(1)}(v,t)\,dv$ in region 1 with velocity in the range v to $v+dv$ by switching regions is equal to $p_a^{(2)}(v_{a,2},t)\,v\,dv/v_{a,2}$. Combining this with Eqs. (2.2) and (2.3) one obtains a diffusion rate

$$\left.\frac{d}{dt}\right|_{\text{diff}} p_a^{(1)}(v,t) = \begin{cases} \frac{v_{a,2}}{4}\frac{A}{V_2} \times \frac{v}{v_{a,2}} p_a^{(2)}(v_{a,2},t) - \frac{A}{V_1}\frac{v_{a,2}^2}{4v} p_a^{(1)}(v,t), & v \geq \sqrt{2\Delta E_a/m} \\ 0, & v < \sqrt{2\Delta E_a/m} \end{cases}. \tag{2.4}$$

Note that the v in Eq. (2.2) is the velocity in region 2 and is therefore replaced by $v_{a,2}$ in Eq. (2.4). For $v^2 < 2\Delta E_a/m$, the diffusion rate is zero due to the potential energy step.

For molecules entering region 2 we introduce $v_{a,1} = \sqrt{v^2 + 2\Delta E_a/m}$ and the derivation of the diffusion rate is entirely analogous. One obtains as the final result,

$$\begin{aligned} \frac{d}{dt}p_a^{(1)}(v,t) &= \begin{cases} \frac{A}{V_2}\frac{v}{4}p_a^{(2)}(v_{a,2},t) - \frac{A}{V_1}\frac{v_{a,2}^2}{4v}p_a^{(1)}(v,t) + \sum_{a'=1}^6 (c_{a',a}^{(1)} p_{a'}^{(1)}(v,t) - c_{a,a'}^{(1)} p_a^{(1)}(v,t)), & v \geq \sqrt{2\Delta E_a/m} \\ \sum_{a'=1}^6 (c_{a',a}^{(1)} p_{a'}^{(1)}(v,t) - c_{a,a'}^{(1)} p_a^{(1)}(v,t)), & v < \sqrt{2\Delta E_a/m}\,, \end{cases} \\ \frac{d}{dt}p_a^{(2)}(v,t) &= \frac{A}{V_1}\frac{v^3}{4v_{a,1}^2}p_a^{(1)}(v_{a,1},t) - \frac{A}{V_2}\frac{v}{4}p_a^{(2)}(v,t) + \sum_{a'=1}^6 (c_{a',a}^{(2)} p_{a'}^{(2)}(v,t) - c_{a,a'}^{(2)} p_a^{(2)}(v,t)). \end{aligned} \tag{2.5}$$

These rate equations are used for the cooling simulations in the main text.

Chapter 3

Design of the microstructured electric trap

3.1 Introduction

A basic outline for the design of an electric trap in which optoelectrical cooling might be realized was originally provided in Ref. [76], presented in the previous chapter. In this chapter, we present an in-depth discussion of the final realization of the trap with a strong emphasis on optimizing the trap electrodes and the electric fields they produce. Fundamentally, the trap design is based on four conditions: providing a deep confining potential for the molecules, realizing a maximal region of homogeneous electric field at the trap center, reducing trap losses to allow for long storage times, and providing an efficient connection to an electric guide for loading and unloading of molecules. Careful consideration allows these conditions to be satisfied quite well simultaneously, although for the current first version of the trap we have to some degree focused on efficient loading and unloading of molecules and on reducing trap losses at the expense of the field homogeneity.

The chapter is organized as follows. We begin by reviewing the various loss channels which are potentially relevant in an electric trap in section 3.2. We then present an overview of the trap design including a discussion of the trap dimensions and how they are chosen based on achieving the trap criteria in section 3.3. This is followed by a discussion of the two critical macroscopic components of the trap, the perimeter electrodes to achieve transverse confinement between the two capacitor plates in section 3.4, as well as the connection between the capacitor plates plus perimeter electrodes and an electric guide for loading and unloading of molecules in section 3.5.

The toughest challenges in realizing a successful trap all relate to the microstructure electrodes constituting the capacitor plate surfaces, considered in section 3.6. In particular, the most intuitive realization of the microstructures, a regular sequence of uniform strips of alternating polarity, would result in strong trap losses due to both Majorana transitions and holes in the trap. As we will show, these losses would limit the trap lifetime to well below one second. After introducing the problems, we first present the mathematical

techniques used to calculate the electric fields in the vicinity of the microstructures. We then show how the problems with the microstructures can be solved using a more complicated microstructure design and subsequently present an overview of the microstructure design in general. Section 3.6 concludes with a consideration of the electric fields from the combination of the microstructure and the trap perimeter electrode.

The final section of this chapter discusses possible improvements to the design of the electric trap to further reduce losses and to increase the field homogeneity inside the trap. Modulating the width of the microstructure electrodes should allow the field gradient in the remaining electric field zeros in the trap to be increased, thereby reducing losses due to Majorana transitions. Changes in the microstructure width might also be used to compensate the electric field induced by the perimeter electrode causing it to drop off at a faster rate towards the center of the trap. This would allow the homogeneity of the electric fields in the trap center to be improved without changing the dimensions of the trap.

3.2 Potential loss mechanisms in an electric trap

Minimizing losses for molecules stored in a trap requires understanding what loss channels are potentially relevant in the first place. For polar molecules in a DC electric trap, a rather comprehensive list of possible processes is collisions with background gas, holes in the strong electric fields constituting the walls of the trap, heating mechanisms which increase the temperature of trapped molecules until they are no longer confined, and transitions to untrapped states. Moreover, transitions to untrapped states can be subdivided into transitions due to blackbody radiation, Majorana transitions, and state changing collisions. We discuss each of these loss channels in turn.

3.2.1 Collisions with background gas

Probably the most well known loss process for particles in a shallow trap (here meaning a trap depth of less than the ambient temperature) is collisions with the background gas. Such losses can be particularly troublesome in experiments with a direct line-of-sight access to a high density source region. In contrast, the guiding techniques used for the molecule experiments in this thesis provide the ability to guide molecules around bends and through differential pumping sections away from the source [51, 100]. This allows the usual base pressures according to standard ultra high vacuum techniques to be reached, with correspondingly low collision rates with background gas. In fact, for atomic systems, lifetimes of many hundreds of seconds have been reached [101, 102], and even longer for experiments in a cryogenic environment [103], demonstrating the degree to which background gas collisions can be suppressed.

To estimate background gas collision rates we make use of a simple analytic theory by Bjorkholm [104] based on the long-range interaction potential between trapped particles and a background gas species. Here, the collision rate is obtained from the maximum impact parameter for a glancing collision which imparts enough energy on a trapped particle

to eject it from its trap. According to this theory, an ensemble of Na atoms in a trap with a 1 K depth colliding with a N_2 background gas at a pressure of 10^{-10} mbar should be lost from the trap with a time constant of 333 s [104]. One might expect the order of magnitude of this result to be transferable to collisions of polar molecules with a polarizable background gas since the dipole-induced-dipole interaction should be of similar order of magnitude as the induced-dipole-induced-dipole interaction between two polarizable particles. Note that this no longer holds for a background gas species which also has a permanent electric dipole moment, in which case the interaction potential strength and therefore the collision rate with the background gas at a given pressure should be considerably higher. According to these considerations, background collision induced losses should be negligible for the present trap experiment considering the background pressure of well below 10^{-10} mbar originating mainly from residual H_2. One remaining caveat is the rather confining trap geometry, so that the background pressure inside the trap might be substantially higher than in the surrounding vacuum chamber.

3.2.2 Holes in the trapping fields

A second possible source of losses for molecules from an electric trap is remaining holes, i.e. weak spots, in the confining high electric fields constituting the trap walls. In a simple quadrupole or Ioffe-Pritchard type configuration this may seem like a trivial effect with the potential in the weakest such hole simply taken to be the trap depth. The situation is substantially more complicated in an effectively extremely high-order multipole trap as we have implemented. For such a trap, deep holes in the confining potential by no means preclude long trapping times of particles with substantially more energy than required to traverse the hole since thousands of collisions with the trap boundary may be necessary before a molecule actually finds the exit channel. This necessitates description of such holes in terms of a loss rate rather than equating the lowest energy required to traverse the weakest hole with the trap depth. We note that the ability to implement such holes is one of the principle reasons to choose such a complicated trap design as our own since it allows direct connection of an input and output guide to continuously load/unload molecules to and from the trap.

While it may seem like holes in the trapping field will rarely if ever appear inadvertently, or that it should at least be easy to eliminate them by appropriate electrode design, the opposite is in fact the case for complicated electrode geometry due to geometric reasons. An electric trap consists of a set of electrodes surrounding some region of space. For a given set of voltages applied, each electrode either has a well defined polarity (plus or minus, based on the sign of the surface-normal electric field), or electric field zeros on the surface of some of the electrodes will exist (see Fig. 3.1a). While such zeros are generally surrounded by non-zero fields hindering molecules from colliding with the surface, these fields are generally lower than the remaining trapping fields and thus constitute weak spots in the trapping potential. Realizing a trap with maximal depth thus requires a definite polarity to be assigned to each electrode, providing a constraint on the trap geometry.

A more difficult problem appears whenever more than two electrodes meet on the sur-

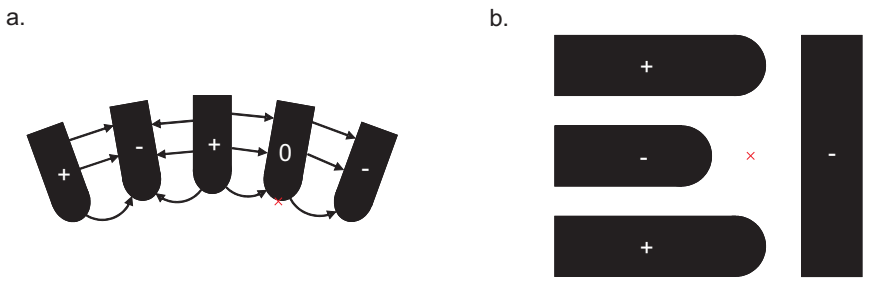

Figure 3.1: Demonstrating the existence of electric field zeros (indicated by the red crosses) in a region of space surrounded by more than 2 electrodes in 2 dimensions. **a**. The sign of the surface-normal electric field must alternate on neighboring electrodes, otherwise the electric field somewhere on the surface of some electrode must be zero. Note that this also holds in 3 dimensions and means that an electric field zero is guaranteed to exist on the surface of some electrode whenever an odd number of electrodes meet. **b**. For $2n > 2$ electrodes of alternating polarity arranged around some region of space, the nonexistence of local extrema of the electric potential in free space dictates the existence of saddle points in the potential, i.e. electric field zeros.

face of the trap, as illustrated in Fig. 3.1b. In two dimensions, such a geometry always leads to an electric field zero somewhere in free space. In three dimensions this corresponds to a channel of zero field leading out of the trap. The only way to plug such holes is to create large electric fields along the third dimension, the direction leading out of the trap. However, making such fields strong enough is again exceedingly challenging, especially when using microstructure electrodes constrained to two dimensions. We thus either have to accept such holes, or come up with a trap geometry which avoids more than two electrodes meeting anywhere on the trap surface. The second possibility can in fact be accomplished using a ring type trap architecture as was implemented in the first design for a continuously loadable electric trap in our group [90]. However, transferring this approach to a microstructured trap would require the microstructure to consist of a series of concentric circles, which poses a problem in terms of contacting.

Considering that holes in the trapping potential appear relatively easily, we calculate the rate at which losses of molecules through such holes will occur. The result is of course also useful to determine the rate at which molecules enter the input and output guide of the trap, which after all are simply (hopefully) the biggest holes in the trap. For an exit channel with a slow variation of the electrodes along the direction of the channel, the electric field can be approximated by assuming a two dimensional electrode geometry. In this case the electric field in the vicinity of the hole is given by a quadrupole or higher order multipole. We restrict our attention to the idealized quadrupole case, a hole with a transverse potential profile $V(r) = V_0 r/r_0$, where V_0 is the trapping potential at some radius r_0 from the center of the hole. Moreover, we assume the trap with volume $\mathcal{V}$ to be filled with molecules of mass m and energy E. It is possible to obtain identical results using either of the following two approaches. First, one can calculate the fraction of molecules

which enter the hole in the time dt, being near enough to the entrance of the hole and with a velocity component along the direction of the hole which is large enough to overcome the potential $V_0 r/r_0$ of the hole. Second, one can compare the phase space volume of the trap with the phase space volume emptied through the output hole in time dt. We proceed with the second approach.

With phase space volume element $d^3x\, d^3v$, the phase space volume of the trap is equal to

$$\int d^3v \int_{\mathcal{V}} d^3x\, \delta\left(\frac{m}{2}v^2 - E\right) = \mathcal{V}\, 4\pi \frac{\sqrt{2E}}{m^{3/2}}. \tag{3.1}$$

To calculate the phase space volume passing through the output in time dt, we can use the same integral, except that the potential energy in the hole needs to be taken into account. Moreover, the spatial volume element depends on the longitudinal velocity v_z and is given by $d^3x = v_z\, dt\, d^2x_t$, where $\mathbf{x}_t$ is the transverse position. We obtain

$$\int_{v_z>0} d^3v \int v_z\, dt\, d^2x_t\, \delta\left(V_0 \frac{|\mathbf{x}_t|}{r_0} + \frac{m}{2}v^2 - E\right) = \left(\frac{\pi r_0}{V_0 m}\right)^2 \frac{2}{3}\, E^3\, dt. \tag{3.2}$$

The loss rate Γ_{hole} of molecules through the hole is now obtained from the ratio of the two previous equations. Denoting the maximum radius from the center of the hole at which molecules can exist based on their energy by $r_{\max} = E\, r_0/V_0$, we obtain

$$\Gamma_{\text{hole}} = \sqrt{\frac{2E}{m}}\, \frac{\pi r_{\max}^2}{12\mathcal{V}} \tag{3.3}$$

We emphasize the strong dependence of the losses on the energy of the molecules, with the losses being proportional to $E^{5/2}$.

3.2.3 Heating mechanisms

For shallow atomic traps, a particularly prevalent loss process is the existence of various heating mechanisms which increase the kinetic energy of atoms until they are no longer confined. This is especially the case for dipole traps where, in addition to off-resonant scattering from the dipole laser, parametric heating due to power or beam-pointing fluctuations are possible. Certainly, heating by scattering of photons is a non-issue in our present experiment, and beam-pointing fluctuations, which might translate to mechanical motion of the trap electrodes, is also extremely unlikely to be relevant. However, we identify several other mechanisms which might cause heating, and discuss them in the following.

While one might generally think of collisions with a background gas as relatively violent events which directly expel molecules from a trap, extremely glancing collisions which provide only a small momentum kick also exist. Such collisions can impart insufficient kinetic energy on a molecule to expel it from the trap and will then instead result in heating. Such collision induced heating was already observed many years ago for Cs atoms [105], and has also been investigated theoretically [106, 107]. Collision induced heating can be a problem particularly in traps with a substantially larger trap depth than the temperature of

the trapped particles. In this case, glancing collisions create individual trapped particles with a substantially higher energy than the rest of the ensemble. Subsequent collisions between these particles and the rest of the ensemble then transfer this energy to the entire ensemble. Considering that we have yet to observe collisions between trapped particles in the present trap, this last mechanism for us is certainly not an issue.

While parametric heating by mechanical oscillations of the trap electrodes hardly needs to be considered, and the DC nature of the trapping fields in principle results in purely conservative forces acting on the molecules, heating due to fluctuations of the voltages applied to the trap electrodes might still be relevant. We estimate the effect of such fluctuations based on the following simple model. Suppose the fractional rms voltage fluctuations in the bandwidth equal to the trap frequency f is equal to $\delta \ll 1$. In this case, molecules moving from the center of the trap to the peak of their trajectory will experience a force which on average varies by a fractional amount δ from the force they experience when moving back to the trap center. During the process, the molecules therefore gain or lose an amount of energy approximately equal to δE, where E is their total energy. Modeling this process as a random walk, a total of approximately δ^{-2} trap oscillations are necessary for the energy of the molecules to increase by a factor of two. We therefore obtain an energy doubling time of approximately $(\delta^2 f)^{-1}$. We note that except for a constant prefactor, this is identical to the result obtained using a quantum calculation by Savard *et. al.* [108]. Considering that fractional voltage fluctuations of far below 10^{-3} can easily be obtained, we see that parametric heating should not be an issue in our experiment.

A final mechanism which potentially might cause heating in our trap is long-range interactions of the molecules with the trap electrodes and other surfaces. This has in fact been investigated in some detail by Henkel and Wilkens for atoms and ions [109]. For ions, surface induced heating can be quite substantial, with a heating rate on the order of 1 Hz for distances from a surface on the order of $10\,\mu$m [109]. Based on the trap design discussed in later parts of this chapter, molecules in our trap will generally have insufficient kinetic energy to approach the trap surface within $10\,\mu$m. Combined with the fact that the interaction of an electric dipole with a surface will be substantially smaller than the interaction of an ion with a surface, we expect surface induced heating not to play a role for us.

3.2.4 Losses via untrapped states

Since the trapping potential in an electric trap strongly depends on the internal rotational state of a molecule, any mechanism causing a change in the molecular state will generally result in trap losses. Such state changes can occur due to the following mechanisms.

3.2.4.1 Blackbody radiation

Considering the very high frequencies of electronic transitions, far above the Boltzmann cutoff at room temperature, and the extremely weak nature of magnetic transitions between hyperfine states, transitions between internal states induced by blackbody radiation

can be completely ignored for atoms. This situation changes entirely for molecules with their strong electric dipole transitions between rotational states and the existence of low-lying vibrational excitations in the tail of the Boltzmann distribution. Blackbody induced transitions have in fact already been observed for OH molecules in an electric trap [99], resulting in state lifetimes of only several seconds at room temperature. It turns out, however, that OH belongs to the relatively special class of molecules with chemical formula XH_n. Here, very light hydrogen nuclei rotate around a single heavier nucleus, leading to very high rotational constants. The resulting very high frequencies between neighboring rotational states dramatically increase the rate at which blackbody induced transitions can occur.

We substantiate the previous by deriving the rate Γ_{bb} at which an arbitrary electric dipole allowed transition between two molecular states is driven by blackbody radiation. It turns out that the only required molecular parameter is the spontaneous decay rate A from the more energetic to the less energetic of the two states. For a transition dipole moment $\mathbf{d}$ between the two states and a transition frequency ω, this is given by

$$A = \frac{\omega^3 |\mathbf{d}|^2}{3\pi\varepsilon_0 \hbar\, c^3}. \tag{3.4}$$

According to the principle of detailed balance, the blackbody induced transition rate is now given by the product $A\,\langle n\rangle$, where $\langle n\rangle$ is the average thermal photon occupation number in a single mode of the electromagnetic field. According to Bose-Einstein statistics, this is given by

$$\langle n\rangle = \frac{1}{e^{\hbar\omega/k_B T} - 1} = \begin{cases} \frac{k_B T}{\hbar\omega} & \hbar\omega \ll k_B T \\ e^{-\hbar\omega/k_B T} & \hbar\omega \gg k_B T \end{cases}. \tag{3.5}$$

For transitions between low-lying rotational states at room temperature, the low frequency limit $\hbar\omega \ll k_B T$ always holds, in which case Γ_{bb} scales as $\Gamma_{\mathrm{bb}} \propto \omega^2 |\mathbf{d}|^2 T$. For a representative transition with a transition dipole moment of $|\mathbf{d}| = 1\,\mathrm{D}$ and a transition frequency of $\omega = 2\pi \times 100\,\mathrm{GHz}$ at a temperature of $T = 293\,\mathrm{K}$, we find $A = (86000\,\mathrm{s})^{-1}$, $\langle n\rangle = 61$, and therefore $\Gamma_{\mathrm{bb}} = (1400\,\mathrm{s})^{-1}$. Taking into account the exact transition frequencies and transition dipole moments, we find that blackbody induced transitions between rotational states should not play a role for any of the experiments performed for this thesis.

For transitions between vibrational states in light and moderately heavy molecules, the high frequency limit $\hbar\omega \gg k_B T$ generally applies. In this case, transitions with an appreciable spontaneous decay rate generally have such high transition frequencies that the low value of $\langle n\rangle$ prevents blackbody induced transitions from happening, whereas for lower-lying vibrational transitions, the dependence of A on ω^3 again sufficiently suppresses Γ_{bb}. However, unlike rotational transitions, whose transition dipole moment is given by the permanent electric dipole moment of the molecule times the relevant Hönl London factor, the transition strengths for the vibrational modes of a given molecule can vary independently over a large range, and must therefore be considered individually. In fact, for CH_3F, the lowest lying vibrational C-F stretch mode has a large spontaneous decay rate of about 13 Hz from the first vibrational excitation to the ground state [110]. Together

with a value of $\langle n \rangle = 0.0058$ at a transition frequency of $1049\,\mathrm{cm}^{-1}$ at $293\,\mathrm{K}$, this results in $\Gamma_{\mathrm{bb}} = 0.075\,\mathrm{Hz} = (13\,\mathrm{s})^{-1}$, which is certainly relevant on the timescales of our experiments.

The previous rates for radiative induced transitions between states can be enhanced by the following two effects. First, electromagnetic noise in the lab can mimic blackbody radiation but with increased power. Here, the effect can be obtained by comparing the spectral power density of the electromagnetic noise with that of the blackbody radiation. For RF noise, the noise spectrum should drop off rapidly above the bandwidth of any amplifiers used in the lab, and should therefore leave transitions between vibrational states and transitions between well separated rotational states unaffected. On the other hand, DC electric fields create Stark splittings between rotational M-sublevels on the order of $1\,\mathrm{GHz}$ and transitions between these states can easily be driven by RF fields. However, the scaling of the rate of blackbody induced transitions with ω^2 implies that RF noise needs to be many orders of magnitude stronger than the blackbody radiation to have an effect. Avoiding RF induced transitions thus requires ensuring that this is not the case.

A second enhancement for the rate of radiative induced transitions results for molecules in close proximity to material surfaces [111]. Here, thermal fluctuations of the charges in the material can cause near fields which are many orders of magnitude larger than the far-field blackbody radiation. To understand this process, we consider an oscillating dipole $\mathbf{d}$ in free space separated by a distance z_0 from a dielectric with dielectric constant ε. In addition to the usual radiation of light, the oscillating dipole can dissipate energy electromagnetically via losses in the dielectric. For a molecule in an excited state, this results in an increase in the spontaneous decay rate to a lower lying state. Here, the fractional increase is equal to the ratio of the energy dissipated in the dielectric by a dipole oscillating at the molecular transition frequency and the energy dissipated via radiation by the same dipole. For thermal excitations in the dielectric and the rest of the environment at the molecular transition frequency, all processes can also happen in reverse. Detailed balance then dictates that blackbody induced transitions occur at the modified spontaneous decay rate times the average occupancy in a single mode of the electromagnetic field.

To estimate the magnitude of the previous effects, we approximate the electric field induced by the dipole $\mathbf{p}$, placed at the origin, to be equal to that of a dipole in free space,

$$\mathbf{E}(\mathbf{x}) = \frac{1}{4\pi\varepsilon_0}\left[k^2(\hat{\mathbf{n}}\times\mathbf{p})\times\hat{\mathbf{n}}\frac{e^{ikr}}{r} + (3\hat{\mathbf{n}}(\hat{\mathbf{n}}\cdot\mathbf{p}) - \mathbf{p})\left(\frac{1}{r^3} - \frac{ik}{r^2}\right)e^{ikr}\right], \tag{3.6}$$

where $r = |\mathbf{x}|$, $\hat{\mathbf{n}} = \mathbf{x}/r$, and k is the wavenumber [112]. The power P_{rad} radiated into space by the dipole is given by twice (due to an equal contribution by the magnetic field) the energy density $\frac{\varepsilon_0}{4}|\mathbf{E}|^2$ of the electric field integrated over a sphere of radius R centered at the dipole with $kR \gg 1$, multiplied by the speed of light,

$$P_{\mathrm{rad}} = 2\,c\int\frac{\varepsilon_0}{4}|\mathbf{E}|^2\,R^2\,d\Omega = c\int\frac{k^4}{32\,\pi^2\,\varepsilon_0}|\hat{\mathbf{n}}\times\mathbf{p}|^2\,d\Omega = \frac{c\,k^4\,|\mathbf{p}|^2}{12\,\pi\,\varepsilon_0}. \tag{3.7}$$

Note that except for a constant factor, $P_{\mathrm{rad}}/\hbar\,\omega$ is the spontaneous decay rate for a transition with transition dipole moment $\mathbf{p}$, as might be expected.

To calculate the power dissipated in the dielectric, the dielectric can be described by a complex dielectric constant $\varepsilon = \varepsilon_r + i\,\varepsilon_i$, where ε_r and ε_i are the real and imaginary parts of ε, respectively. In this case, the power dissipation per unit volume is equal to $\frac{\omega\,\varepsilon_i}{2}|\mathbf{E}|^2$ [112]. For an order of magnitude estimate, we approximate the electric field as

$$\mathbf{E}(\mathbf{x}) \sim \frac{1}{4\,\pi\,\varepsilon_0}\frac{\mathbf{p}}{r^3}, \tag{3.8}$$

thereby only considering the near field and disregarding the anisotropy of the dipole field. The power dissipated in the dielectric is then given by integrating over the volume $z > z_0$ containing the dielectric,

$$P_{\rm dis} \sim \int_{z>z_0} d^3x \frac{\omega\,\varepsilon_i}{2}\left(\frac{|\mathbf{p}|}{4\,\pi\,\varepsilon_0\,r^3}\right)^2 = \frac{\omega\,\varepsilon_i|\mathbf{p}|^2}{32\,\pi^2\,\varepsilon_0^2}\,\frac{\pi}{6\,z_0^3} \sim \frac{\omega\,\varepsilon_i|\mathbf{p}|^2}{\varepsilon_0^2\,z_0^3}. \tag{3.9}$$

The ratio of power absorbed by the dielectric and the radiated power is therefore given by

$$P_{\rm dis}/P_{\rm rad} \sim \frac{\varepsilon_i}{\varepsilon_0}\frac{1}{(k\,z_0)^3}, \tag{3.10}$$

this being the fractional amount by which blackbody radiation induced transitions are enhanced. The modification of the transition rate thus increases with the inverse cube of the molecule-surface separation z_0, and, for a somewhat typical value of $\varepsilon_i/\varepsilon_0$ of 10^{-3}, is of similar order of magnitude as the free-space transition rate when z_0 is approximately two orders of magnitude less than the wavelength of light at the transition frequency.

A more comprehensive analysis of the effect of a surface on blackbody radiation induced transitions has been performed by Buhmann *et. al.* [111]. In particular, Buhmann *et. al.* include the modification of the electromagnetic field by the material surface. In addition to slightly changing the power absorbed in the dielectric, this can modify the radiated power via the Purcell effect. In the limit of small z_0, Buhmann *et. al.* find a fractional increase in the blackbody radiation induced transition rate given by

$$\frac{\varepsilon_i\varepsilon_0}{2|\varepsilon+\varepsilon_0|^2}\frac{1}{(k\,z_0)^3}. \tag{3.11}$$

Note that except for a slightly changed dependence on ε, this is identical to the result derived here.

3.2.4.2 Majorana transitions

Solving the molecule Hamiltonian in an electric field results in molecular eigenstates corresponding to specific rotational M-sublevels only for a quantization axis chosen parallel to the direction of the electric field. However, as a molecule moves, the direction of the electric field may vary. As a result, a molecular eigenstate for the electric field at one point in time projected onto the molecular eigenstates for a rotated electric field at a later point in time results in a contribution from the complete set of rotational M-sublevels. This

redistribution among states is suppressed for a sufficiently slow rotation of the direction of the electric field, allowing the molecular states to follow adiabatically. Conversely, for a fast rotation, molecules in low-field-seeking states can undergo transitions to untrapped states, resulting in trap losses. Such a fast rotation occurs in particular in the vicinity of field zeros, where the direction of the field can flip practically instantaneously, causing these so-called nonadiabatic, spin-flip, or Majorana losses to be a particularly prevalent loss mechanism in electric or magnetic quadrupole traps for neutral particles. Any other electric or magnetic trap design with field zeros will of course also suffer from these losses.

Majorana losses have been investigated experimentally for polar molecules in an electric trap in quite some detail by Kirste *et. al.* [98]. Specifically, trap losses for various isotopes of ammonia were determined for both an electric quadrupole as well as for an electric Ioffe-Pritchard type trap. As might be expected for Majorana losses, the loss rates in the quadrupole trap were generally larger and strongly isotope dependent. Moreover, double exponential decays were observed for the quadrupole trap, consistent with a Majorana loss rate depending on the hyperfine state of the molecule.

We estimate the dependence of the Majorana loss rate on trap and molecule parameters. Field zeros locally almost always take the shape of a quadrupole potential, with the electric field increasing linearly away from the zero. Except in the case where hyperfine structure dominates, in which case Majorana flips may potentially be avoided altogether [98], the separation ΔV between neighboring rotational M-sublevels generally depends either linearly or quadratically on the electric field for electric field strengths at which Majorana transitions may happen. Thus,

$$\Delta V = (c_E\, x)^n, \tag{3.12}$$

where x is the distance of a molecule from the field zero, c_E is a coefficient which, among other things, quantifies the slope of the electric field strength versus position near the zero, and $n = 1$ for a linear Stark shift or $n = 2$ for a quadratic Stark shift. A Majorana transition is likely to happen if a molecule passes by a field zero such that the minimal value of ΔV along its trajectory, occuring at a distance b from the zero, is comparable to or less than the rate of approximately v/b at which the direction of the electric field changes. Here, v is the velocity of the molecule. As a result, the critical minimal distance for a molecule to pass by a zero such that a Majorana transition becomes likely to happen is

$$b \approx \sqrt[n+1]{\frac{v}{c_E^n}}. \tag{3.13}$$

The effective "cross section" for Majorana losses for a total of N identical zeros in a trap of volume $\mathcal{V}$ is then approximately $N\, b^2$, so that the loss rate is given as

$$\Gamma \approx \frac{N\, b^2\, v}{\mathcal{V}} \approx \begin{cases} \frac{N\, v^2}{\mathcal{V}\, c_E} & n = 1, \\ \frac{N\, v^{5/3}}{\mathcal{V}\, c_E^{4/3}} & n = 2. \end{cases} \tag{3.14}$$

For $n = 1$ and fixed trap volume $\mathcal{V}$, the Majorana loss rate depends linearly on the energy of the molecules and is inversely proportional to the electric field strength in the vicinity of

the zeros. Note that Majorana losses will typically be much stronger for molecular states with quadratic Stark shifts ($n = 2$), since the energy splitting between neighboring states then approaches zero much more quickly for low fields.

3.2.4.3 Inelastic collisions

A final process for the internal state of a molecule to change would be via inelastic collisions between the molecules themselves. Here, not only the change to an untrapped state can cause trap losses, but also the fact that the conversion of internal energy to kinetic energy might expel both collision partners from a trap. However, despite the propensity for inelastic collisions to cause unwanted trap losses, at present we would consider the observation of such collisions between cold molecules to be a definite achievement. The investigation of such collisions is of great interest to improve the understanding of molecular dynamics, being one of the often cited reasons to study cold molecules.

3.3 Overview of the trap design

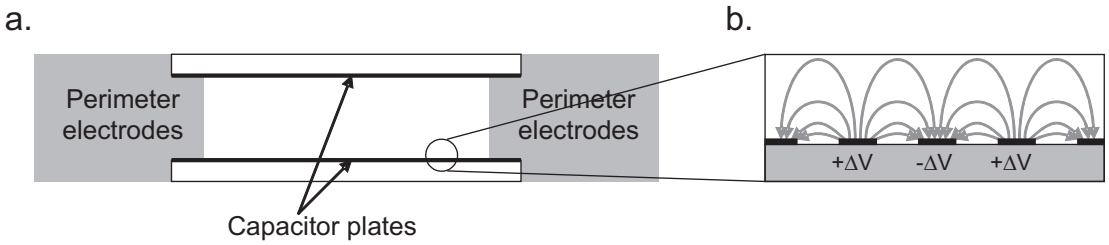

Figure 3.2: Fundamental design for a microstructured trap. **a.** Molecules are confined between two capacitor plates with perimeter electrodes in the shaded grey region around the circumference of the trap providing transverse confinement. **b.** Collisions with the capacitor plate surface are avoided by microstructuring it (see text).

The fundamental design for a microstructured capacitor-plate type trap is shown in Fig. 3.2. The primary goal of the trap design, providing a large region of tunable homogeneous fields in the trap center, is achieved by trapping the molecules between a pair of capacitor plates. Confinement of the molecules, i.e. creating much higher fields everywhere at the trap periphery, can be simultaneously achieved by microstructuring the plate surface with an array of electrode strips of alternating DC polarity and by surrounding the circumference of the trap with some arrangement of perimeter electrodes.

The dimensions of the flat rectangular box which approximately describes the trap volume have a substantial impact on the properties of the trap. Here, establishing the trap dimensions is closely related to establishing the periodicity of the capacitor plate microstructure, which we therefore consider concurrently. The choice of trap dimensions separates quite well into the two individual questions of choosing the ratio between the various dimensions and choosing their absolute value. In particular, the ratio affects the

field homogeneity which can be achieved in the trap, the loading and unloading of molecules to and from the trap, and the ability to suppress Majorana losses. The overall dimensions again affect the loading and unloading of molecules as well as the size of the molecule ensemble which can be stored in the trap, and are directly related to technical constraints.

3.3.1 Establishing the ratio of the trap dimensions

Determining the effect of the trap dimensions on the achievable field homogeneity requires understanding how the high confining electric fields at the trap periphery drop off towards the inside of the trap. We first consider the fields resulting from the perimeter electrodes. This is in fact a classic problem in electrodynamics [112]: determining the electric field in a volume defined by $x > 0$, $0 < y < a$, and translation symmetry in the z direction, with a constant potential Φ_0 and Φ_1 on the surfaces $y = 0$ and $y = a$, respectively, and an arbitrary potential on the surface $x = 0$. Here, the y-direction is the direction between the capacitor plates with a being the separation between the plates, x is the direction into the trap, and z is the direction along the perimeter electrodes. The general solution to this problem is given by [112]

$$\Phi(x, y, z) = \Phi_0 + (\Phi_1 - \Phi_0)\, y + \sum_{n=1}^{\infty} a_n \exp\left(\frac{-n\,\pi\,x}{a}\right) \sin\left(\frac{n\,\pi\,y}{a}\right), \tag{3.15}$$

where the $\{a_n\}$ are expansion coefficients. As can be seen, the electric fields caused by the perimeter electrodes always decay exponentially towards the center of the trap. The slowest decaying component is from the term with the a_1 coefficient, which decays by a factor of 10 over a distance of $\frac{\ln 10}{\pi}\, a$. Thus, for each order of magnitude by which the perimeter electrode fields are to be suppressed, the distance from the center of the trap to the perimeter electrodes must be increased by 0.733 times the capacitor plate separation.

The electric fields originating from the capacitor plate microstructure strips are surprisingly similar to those from the perimeter electrodes. Let d be the periodicity of the microstructure, i.e. the distance between consecutive electrodes of equal polarity. Consider the volume defined by $x_0 < x < x_0 + d/2$, $y > 0$, and translational symmetry along the microstructure, taken to be oriented along the z direction. Here, x_0 is the midpoint above one of the electrodes, in which case, assuming equal spacing between all the microstructure electrodes, $x_0 + d/2$ is the midpoint above the neighboring electrode of opposite polarity. The planes $x = x_0$ and $x = x_0 + d/2$ are reflection planes. The x component of the electric field therefore vanishes in these planes, i.e. Neumann boundary conditions hold. Except for the change in the type of boundary condition, we thus have the same problem as before, with the general solution given by

$$\Phi(x, y, z) = \Phi_0 + E_0\, y + \sum_{n=1}^{\infty} a_n \exp\left(\frac{-n\,2\pi\,y}{d}\right) \cos\left(\frac{n\,2\pi\,(x - x_0)}{d}\right). \tag{3.16}$$

Here, E_0 is the homogeneous offset field between the two capacitor plates. Note that we are approximating the opposite capacitor plate at $y = a$ to be an infinite distance away.

The term with the a_1 coefficient again decays slowest, with a decrease by a factor of 10 over a distance of $\frac{\ln 10}{2\pi}\, d$. The inhomogeneous microstructure field is thus suppressed by a factor of 10 for each increase in the distance from the microstructure by 0.366 times the microstructure periodicity.

We next consider the effect of the trap dimensions on loading and unloading of molecules to and from the trap. According to Eq. 3.3, the rate with which molecules escape through a hole in the trap scales as $\Gamma_{\text{hole}} \sim \frac{v\mathcal{A}}{\mathcal{V}}$, where v is the velocity of the molecules, $\mathcal{A}$ is the effective area of the hole, and $\mathcal{V}$ is the trap volume. For an appropriate value of $\mathcal{A}$ (according to the size of the openings to the input and output guides of the trap), Γ_{hole} describes the rate with which molecules find the trap exit as well as the rate with which the density of molecules in the trap approaches the density of molecules in the input guide during loading. In the case where losses through the trap input and output are the dominant trap loss mechanism, Γ_{hole} determines the timescale for loading and unloading of molecules to and from the trap. In this case a large value of Γ_{hole} is useful since experiments with the trap can be performed at a higher rate. However, the maximal density which can be obtained in the trap will simply reflect the density in the input guide, and the number of detected molecules obtained from loading and unloading the trap once will simply reflect the trap density times the trap volume, independent of Γ_{hole}. Obtaining a large value of Γ_{hole} is much more important when other trap losses, occurring at a rate Γ_{loss}, dominate. In this case the maximum obtainable trap density as well as the fraction of trapped molecules which can be unloaded both scale as $\Gamma_{\text{hole}}/\Gamma_{\text{loss}}$, and the total signal for loading and unloading the trap once scales as $(\Gamma_{\text{hole}}/\Gamma_{\text{loss}})^2$. A large value of Γ_{hole} is then clearly very important.

Determining the scaling of Γ_{hole} with the trap dimensions of course depends on how the input and output guides are attached to the trap, as discussed in detail in section 3.5. Here, the only viable approach seems to be to interrupt the trap perimeter electrodes at some point and attach the guide. Considering that all electric guides for molecules which have been realized to date have had a more or less cylindrical potential for the molecules, both transverse dimensions of a well matched guide attached to the trap would be proportional to the separation of the microstructure plates a so that the area of the guide is proportional to a^2. For transverse trap dimensions b and c, resulting in a trap volume $\mathcal{V} = a \cdot b \cdot c$, we obtain

$$\Gamma_{\text{hole}} \propto \frac{v\, a}{b\, c}. \tag{3.17}$$

We see that a large value of Γ_{hole} requires a large microstructure plate separation and small transverse trap dimensions, exactly the opposite of what is needed for homogeneous fields. Reducing all three trap dimensions by an equal amount also increases Γ_{hole}. Finally, we note that Γ_{hole} decreases for colder molecules, which is of particular importance once the molecules are cooled.

The final effect of the ratio of the trap dimensions relates to the specific approach which was chosen to suppress Majorana losses in the trap. As discussed in section 3.6.4, the width of the microstructure strips is tapered to provide on offset field which eliminates electric field zeros. Here, a minimum degree of tapering is necessary, restricting the ratio

of the microstructure length to width. We note that increasing the overall trap dimensions reduces the degree of tapering which is necessary.

In the previous, we have seen that a large ratio between the transverse trap dimensions and the microstructure plate separation as well as between the plate separation and the microstructure periodicity is necessary to achieve highly homogeneous fields inside the trap. On the other hand, a large ratio reduces Γ_{hole} and can prevent Majorana losses from being effectively suppressed. Considering that the homogeneity of the electric fields doesn't directly affect the ability to trap molecules but "only" affects the ability to further experiment with the molecules once trapping has been achieved, a ratio between the trap dimensions was chosen for the initial trap design which only results in moderately homogeneous fields. Specifically, a suppression of the high trap periphery fields at the central point in the trap by at least four orders of magnitude is obtained by choosing a ratio between the microstructure plate separation and the microstructure periodicity of at least 2.9 and by choosing a ratio between the transverse trap dimensions and the plate separation of at least 5.9. Note that the field homogeneity in, say, the 50 % of the trap volume with the smallest variation in the electric field strength, will be substantially worse than the homogeneity near the central point in the trap.

3.3.2 Establishing the overall scale of the trap dimensions

In addition to affecting the rate Γ_{hole} for molecules to enter and exit the trap, scaling all the trap dimensions in particular affects the number of molecules which can be trapped inside. Here, we consider two scenarios regarding the molecule source for the trap. First, the trap might be combined with a high-density source where the density in the trap is limited by the need to avoid losses via inelastic collisions on the timescale needed for the desired manipulation of the molecules inside the trap. The maximum trap density is then independent of any trap properties and increasing the trap volume proportionally increases the number of molecules which can be usefully loaded into the trap.

The second and current scenario is for molecules being loaded into the trap from a velocity selected source. In the case where losses via the entrance and exit hole dominate, the density in the trap during loading eventually approaches the density of molecules in the input guide, and increasing the trap dimensions can again dramatically increase the number of molecules which can be obtained from the trap. However, increasing the trap dimensions is no longer beneficial when other trap losses dominate. In this case, doubling the trap dimensions reduces Γ_{hole} by a factor of 2, which, assuming the other trap losses remain constant, reduces the number of molecules which can be unloaded from the trap by a factor of 4. Moreover, increasing the dimensions of the input guide and effusive source by a factor of 2 reduces all molecule densities by an additional factor of 2. This is because the high pressure in the region directly behind the effusive nozzle which limits the maximum guide density due to boosting [52] extends over twice the distance. Increasing the trap dimensions beyond the point where Γ_{hole} is approximately equal to other trap losses thus no longer increases the number of molecules which can be unloaded from the trap, and this point might thus be taken to define an optimal size for the trap.

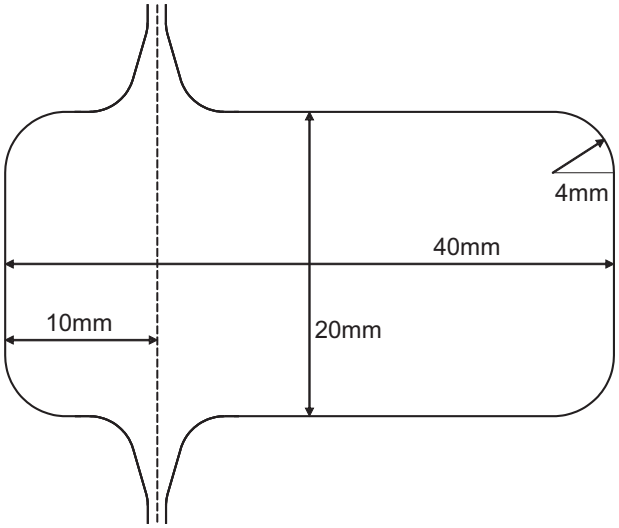

Figure 3.3: Dimensions chosen for the microstructured trap. The solid outer line shows the inner edge of the perimeter electrodes. The transverse dimensions are 2 cm by 4 cm with a 3 mm separation between the microstructure plates and a 0.8 mm microstructure periodicity. The connection to an input and output guide is centered relative to one of the two independently tunable trap regions.

Before fixing the trap dimensions, two technical points also need to be considered. First, a large trap size is desirable since it simplifies the manufacturing of the trap components. Thus, scaling the present design of the trap down to a microstructure plate separation of less than 1 mm would be quite challenging. Second, increasing the trap dimensions requires all voltages applied to trap electrodes to be increased proportionally if the electric field strengths in the trap are to remain constant. Thus, obtaining electric fields on the order of 100 kV/cm for electrodes separated by more than 1 mm requires voltages which are more and more difficult to handle.

A final criterion for trap dimensions is the desire to provide two independently tunable regions of homogeneous field inside the trap. In addition to being a requirement for the original proposal of opto-electrical cooling, this allows for additional manipulation of the molecules such as confining the molecules to a single half of the trap. Satisfying this criterion is accomplished by choosing the length of the trap to be twice the width, with the microstructure on the capacitor plates being configured to allow independent voltages to be applied to the two halves.

Given the lack of sufficiently accurate a priori knowledge concerning the loss processes in the trap, choosing the trap size so that Γ_{hole} is similar to the rate of other trap losses was not possible. As an alternative, the trap size in the end was chosen by trying to optimally match the trap to a quadrupole guide with the standard size for a quadrupole guide in our group. Specifically, to match a quadrupole guide made of cylindrical electrodes of radius 1 mm with a 1 mm separation between neighboring electrodes, a separation between the microstructure plates of 3 mm was chosen, as described in section 3.5. The criteria for the

ratio of the trap dimensions from the previous section were then satisfied by choosing a microstructure periodicity of 0.8 mm and choosing transverse trap dimension of 2 cm by 4 cm. This results in a top view of the trap as shown in Fig. 3.3.

3.4 Transverse confinement via a perimeter electrode

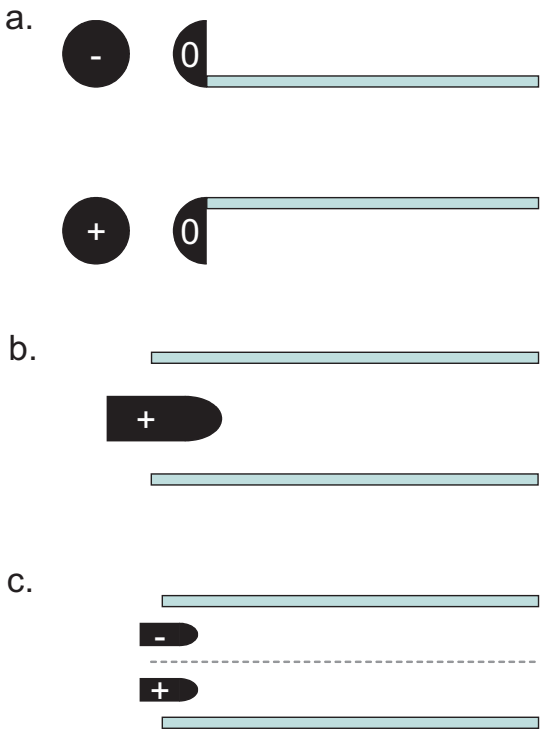

Figure 3.4: Variations for the design of the perimeter electrode.

With the two microstructure capacitor plates confining the molecules in one dimension, full three dimensional trapping is achieved by providing additional transverse confinement around the perimeter of the trap. The perimeter electrode geometry for the transverse confinement is basically dictated by the following three considerations. Most importantly, the perimeter electrodes must ensure a strong uniform trap depth. Second, it must be possible to interrupt the perimeter electrode to allow efficient loading and unloading molecules to and from the trap. In our case we aim to connect the trap to a quadrupole guide. Finally, good optical access from the side of the trap is desirable.

Three possible designs which were considered for the perimeter electrode are shown in Fig. 3.4. The first design which was considered is shown in Fig. 3.4a. This design has the advantage of providing optimal optical access. However, both the other criteria are difficult to satisfy. In particular, the lack of an opposing electrode with the opposite voltage at the transition between the semicircular electrode and the microstructure plates leads to weaker confining fields. Moreover, the need to extend the microstructure directly to the

edge of the microstructure plate posed an uncertain technical challenge. The requirement to connect the perimeter electrodes to a quadrupole also remains an unsolved challenge for this geometry since the dipolar symmetry of the edge of the trap is inconsistent with the quadrupole symmetry of the guide.

By placing the perimeter electrode between the microstructure plates as shown in Fig. 3.4b, the problems with the first design are completely solved. With sufficient overlap between the perimeter electrode and the microstructure plates, the electric field between the two approaches a homogeneous value. By additionally appropriately shaping the curvature at the inner side of the perimeter electrode, we can aim at achieving completely uniform confining fields on the entire surface of the perimeter electrode. This is discussed in detail in section 3.4.1. A straightforward connection to a quadrupole guide is also possible in this configuration. Interrupting the perimeter electrode, we extend the two microstructure plates to the negative electrodes of the quadrupole and extend the two sides of the gap in the perimeter electrode to the positive electrodes. This transition is discussed in detail in section 3.5. Despite the diminished optical access, this design was therefore chosen for the trap.

The third design which we consider is shown in Fig. 3.4c. Here, the single perimeter electrode between the two plates is replaced by two identical perimeter electrodes. With opposite voltages applied to the two microstructure plates, the plane between the two plates (indicated by a dashed line in Fig. 3.4c) is a reflection plane. We can therefore imagine an electrode at zero potential located in this plane and we obtain two versions of the second perimeter design stacked on top of each other. With this design, we retain direct optical access to the center of the trap. Additionally, due to the reflection symmetry, the edge fields due to the perimeter electrodes fade out more rapidly towards the center of the trap than in the second design. A disadvantage of this approach is the smaller perimeter electrode dimensions for a given plate separation which presents more challenging construction requirements. Additionally, with an electrode topology identical to the first design, connection to a quadrupole guide is difficult. However, by interrupting the perimeter electrodes as in the second design, an efficient connection to a hexapole guide could probably be realized.

3.4.1 Shape of the perimeter electrode

While the perimeter electrode design in Fig. 3.4b in principle allows a strong uniform transverse trapping field to be achieved, actually achieving this goal requires the edges of the electrode to be suitably shaped. There plausibly exists a shape for the perimeter electrode for which the electric field strength is constant on the entire surface of the electrode. Such a shape could be considered optimal since the confining field strength due to the perimeter electrode could be ramped infinitesimally close to its breakdown electric field strength. However, it is completely unclear how to find an exact solution to this problem: we require a surface shape that satisfies Dirichlet and Neumann boundary conditions simultaneously. However, the electric field strength at each position on the electrode surface depends on the position of the surface at all other points of the electrode.

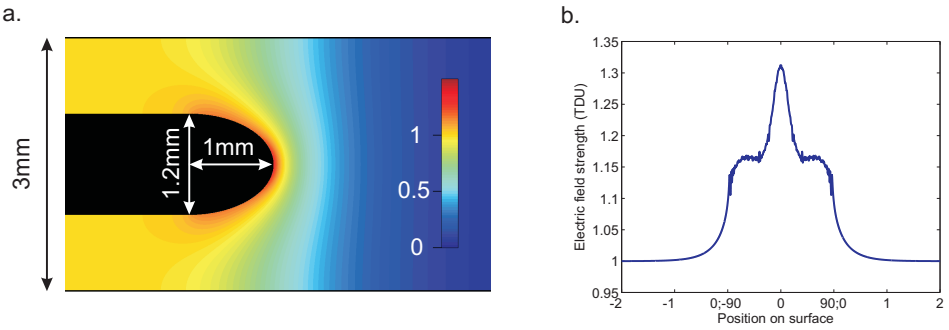

Figure 3.5: Perimeter electrode realization and resulting electric field strength distribution in units of trap depth (TDU, see text). **a.** The electrode consists of a plate with a width of 40 % of the separation between the microstructure plates. The edge of the plate is an ellipse with a semi-major axis of one third of the microstructure-plate separation. **b.** Electric field strength on the surface of the perimeter electrode. On the flat part of the surface, position is given in mm. On the elliptical part, position is given in terms of the angle from the ellipses center.

Perhaps more importantly, other considerations are also relevant for the perimeter electrode design. In particular, an acceptable optical access from the side of the trap requires a sufficient separation between the microstructure plates and the perimeter electrode. Moreover, keeping the electrode shape simple is advantageous for drafting and implementation. Last but not least, experience from operating the trap has shown that the perimeter electrode is far from being the limiting factor in determining the maximum possible trapping field strength, this instead being the microstructure plates. A weaker condition for the perimeter electrode shape would therefore be requiring the electric field strength on the perimeter electrode surface to be everywhere larger than the maximum electric field strength due to the perimeter electrode on the microstructure plate surface.

The perimeter electrode shape and dimensions chosen for the present trap to satisfy the previous criteria is shown in Fig. 3.5a. Additionally, Fig. 3.5a shows the electric field strength distribution resulting from this configuration, with the electric field strength on the perimeter electrode surface shown in Fig. 3.5b. As can be seen, the field on the perimeter electrode surface remains constant to an acceptable degree, with the maximum field strength being approximately 30 % higher than the trapping field between the perimeter electrode and the microstructure plates. We note that the maximum field could be reduced using a slightly flatter front edge of the perimeter electrode. However, this would increase the field away from the front edge. To reduce the field everywhere relative to the trapping field would require the distance between the perimeter electrode and the microstructure plates to be reduced. Finally, we note that the increased field at the edge of the perimeter electrode is in fact an advantage in two regions of the trap where this field is reduced due to additional electrode geometry. These are the bends of the perimeter electrode in the corners of the trap, discussed in section 3.4.2, and the entrance and exit channels of the trap discussed in section 3.5.

3.4.1.1 Definition of trap depth units (TDU) to account for scaling of the trap voltages

Throughout this chapter, we repeatedly show electric field strength distributions resulting from various trap electrode geometries, as in Fig. 3.5. Here, the absolute scale of the electric field strength of course not only depends on the electrode geometry, but also on the voltages applied to the electrodes. Since this scaling is relatively arbitrary, it is useful to define a consistent scaling for the electric field strength. As a result, we define the nominal trap depth to be the electric field strength equal to the voltage difference between the perimeter electrode and the average voltage on the capacitor plate electrodes divided by the 0.9 mm distance between the perimeter electrode and the capacitor plates. From Fig. 3.5, we see that the nominal trap depth is equal to the confining electric field strength due to the trap perimeter electrode. We define trap depth units (TDU) to measure an electric field strength in units of the nominal trap depth. In section 3.6.2, we define a standard ratio between the voltage applied to the trap perimeter electrode and the voltages applied to the trap microstructure. The trap depth units can then also be used for the electric fields produced by the trap microstructure.

3.4.2 Perimeter electrode at the corners of the trap

The previous description of the electric fields produced by the perimeter electrode assumes translation symmetry along the perimeter electrode. This of course no longer holds in the vicinity of the corners of the trap, resulting in modified fields. Here, the bend of the perimeter electrode to a slight degree shields the front edge of the perimeter electrode from the capacitor plates, resulting in reduced electric fields. Additionally, the inhomogeneous perimeter fields are expected to extend further into the trap.

To investigate this situation, we consider the fields produced by a completely circular perimeter electrode. We then have azimuthal symmetry about a symmetry axis perpendicular to the capacitor plates, allowing the fields produced by an arbitrary arrangement of (cylindrically symmetric) perimeter electrodes to be expressed using an analytic expression comparable to Eq. 3.15. Specifically, with translation symmetry along the z axis replaced by rotation symmetry along an azimuthal ϕ coordinate and with the x coordinate replaced by the radius r from the symmetry axis, we obtain

$$\Phi(r, y, \phi) = \Phi_0 + (\Phi_1 - \Phi_0)\, y + \sum_{n=1}^{\infty} a_n J_0\left(\frac{i\, n\, \pi\, r}{a}\right) \sin\left(\frac{n\, \pi\, y}{a}\right), \tag{3.18}$$

where $J_0(z)$ is the zeroth order Bessel function of the first kind. Along the imaginary axis,

$$J_0(i\, r) \approx \frac{e^r}{\sqrt{2\, \pi\, r}} \qquad \text{for} \qquad r \gg 1. \tag{3.19}$$

We thus see that for large r, Eq. 3.19 is identical to Eq. 3.15 except for an additional factor $1/\sqrt{r}$, causing a slightly slower decay of the perimeter field towards the trap center.

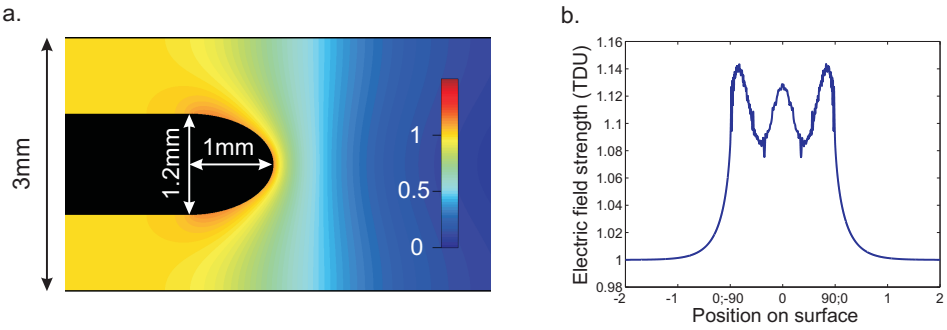

Figure 3.6: Electric field strength at the corners of the trap, if the perimeter electrode profile were swept over a full circle to provide azimuthal symmetry. The depiction is the same as in Fig. 3.5.

To investigate the fields in the vicinity of the perimeter electrode, we require the specific perimeter electrode geometry. This is defined by sweeping the transverse profile in the straight sections of the perimeter electrode as described in the previous section over a quarter circle about an axis located 4 mm from the front edge of the perimeter electrode, as shown in Fig. 3.3. If the curvature of the perimeter electrode is continued over a full circle, the resulting cylindrical symmetry allows the electric fields to be calculated with substantially higher accuracy. This gives rise to fields as shown in Fig. 3.6. Note that the actual fields near the corners of the trap will lie somewhere between those shown in Fig. 3.6 and those shown in Fig. 3.5. As we can see, the field at the front edge of the perimeter electrode is reduced by approximately 14 %, but remains higher than the maximum field at the surface of the microstructure plate. The increased fields at the front edge of the perimeter electrode are thus important at the trap corners and would even allow a slightly smaller corner bend radius without reducing the trap depth.

3.5 Connecting the trap to a quadrupole guide

The basic principle for attaching a quadrupole guide to our trap for loading and unloading of molecules is relatively simple. Creating a gap in the trap perimeter electrode at some point, two opposing electrodes of the quadrupole are attached to the perimeter electrode on the two sides of the gap, and the other two electrodes are attached to the microstructure plates. However, achieving an efficient connection requires several details to be worked out, mainly related to maintaining a sufficient transverse trapping depth and providing a uniform and preferably large channel of low electric field along the entire trap-guide transition. These are addressed in the following.

3.5.1 Optimized depth for a connecting guide

A first question one might consider when attaching a guide to the trap is determining the optimal transverse potential depth of the guide. Naively, one might expect the optimal

depth to be equal to the potential depth of the trap, but this is not the case: Suppose the two are equal. In this case a molecule in the guide with a transverse energy equal to the guide depth must have a longitudinal velocity of zero if it is to be confined in the trap. Slightly reducing the guide depth will then result in a loss of the transversely hottest molecules of which only a vanishing fraction might have been trapped, whereas the area of the guide which can be occupied by all other molecules simultaneously increases. The net flux of molecules entering the trap will thus increase.

An optimal value for the depth of the quadrupole guide can be derived as follows. Let V_T be the potential depth of the trap. We assume a guide with a perfect quadrupole potential profile whose transverse depth V_G can be varied independent of the trap depth. In this case, the effective area of the guide for a molecule with a linear Stark shift and with transverse energy E_t is proportional to $(E_t/V_G)^2$. To obtain the total molecule flux, we multiply by the molecule velocity distribution and integrate over the velocity. Assuming a uniform distribution of molecules in phase space, the velocity distribution for the flux of molecules along the guide is proportional to $dE_t\, v_l\, dv_l$, where v_l is the longitudinal velocity. For $V_G \leq V_T$, the total flux of guided molecules which can be trapped is then proportional to

$$\Phi = \int_0^{V_G} dE_t \int_0^{V_T - E_t} dv_l^2 \left(\frac{E_t}{V_G}\right)^2 = \frac{V_G V_T}{3} - \frac{V_G^2}{4}. \tag{3.20}$$

Maximizing Φ by varying V_G results in a value of $V_G = \frac{2}{3} V_T$. The potential depth of a guide for loading molecules into the trap can thus be considerably below the trap depth without reducing the flux of molecules entering the trap.

The previous derivation is based on several disputable assumptions. First, we have assumed the dimensions of the guide to be fixed, whereas increasing the guide dimensions can of course also considerably increase the flux of molecules entering the trap. However, taking into account the guide dimensions will only increase the optimal value of V_G relative to V_T if an increase in the guide dimensions simultaneously results in an increase in the guide potential depth, and, if anything, the opposite will be the case. A second assumption is the uniform initial distribution of the molecules in phase space which, for a real-world source, of course won't be the case. In particular, for an effusive nozzle, collisions during beam formation increase the share of molecules with a high forward velocity [52], but this in fact even further reduces the optimal value of V_G. Third, we consider the trap and the guide as separate entities, whereas assuming both to be part of the same trapping environment would mean that a lower transverse depth in the guide is equivalent to a lower trap depth. However, as long as the lower electric fields don't extend too far into the guide to trap transition, most molecules only have two opportunities to probe the weaker confinement in the guide: once on their way in and once on their way out of the trap, this being the framework on which the present derivation is based. In contrast, a molecule might have many opportunities to probe the weakest confining field inside the trap, greatly increasing the probability that a molecule with slightly more energy than the confining field depth will eventually approach the trap boundary with a sufficiently steep angle to escape the trap. Finally, we note the reliance of the previous derivation on the assumption of

a perfect quadrupole potential as well as on the assumption that maximizing the flux of molecules into the trap is the relevant figure of merit.

So far this discussion has been restricted to loading of molecules into the trap and we now switch to briefly consider the unloading of molecules as well. In the case where the trap unloading rate is unimportant, i.e. when molecules exiting the trap through the output guide is the dominant trap loss process and when achieving a high unloading efficiency surpasses any other reasons to limit the unloading duration, an optimal potential depth for the unloading guide is given by the maximum energy of the molecules inside the trap. Conversely, when a high unloading rate is important, maximizing the flux of molecules in the guide is again achieved with a potential depth in the unloading guide below the energy of the hottest molecules in the trap.

3.5.2 Realizing a capacitor-plate-based quadrupole guide

In the transition from the guide to the trap, two of the guide electrodes flatten into the two capacitor plates whereas the other two electrodes deform into the perimeter electrodes and bend outward to start their encirclement of the trap volume. Once the perimeter guide electrodes start to bend outward, the electric field they produce at the surface of the capacitor plate guide electrodes starts to weaken and eventually approaches zero. To avoid losses, it is therefore sensible to begin the microstructuring of the plate surface before the outward bend of the perimeter guide electrodes begins. Considering that the capacitor plate guide electrodes must be flat before the microstructure can begin, the guide-trap transition necessarily includes an intermediate two dimensional quadrupole geometry where two of the electrodes consist of two parallel planes.

The capacitor-plate-based guide is in fact the bottleneck in loading and unloading molecules to and from the trap. With the capacitor plate separation determined by the trap dimensions, the shape and separation of the two perimeter guide electrodes are the only parameters which can be varied. Together with the condition of providing a sufficient transverse depth, one obtains a tight upper bound for the surface area on which molecules can be guided.

The dimensions of the capacitor-plate-based guide for our experiment as well as the resulting electric fields are shown in Fig. 3.7. The front edges of the two perimeter guide electrodes are 1.2 mm apart and have the same shape as the perimeter electrode in the trap. This results in an electric field strength at the midpoint of the surface of each of the four electrodes which is about 30 % less than the trap depth. It is in fact impossible to maintain an electric field strength on the surface of the electrodes which everywhere is at least equal to the trap depth since increasing the separation between the plate and the perimeter electrodes necessarily reduced the electric field on the plate surface. However, as pointed out in the previous section, realizing a transverse guide depth equal to the trap depth is by no means desirable, and the transverse depth we achieve is in fact quite close to the value of two thirds the trap depth which was calculated to be ideal.

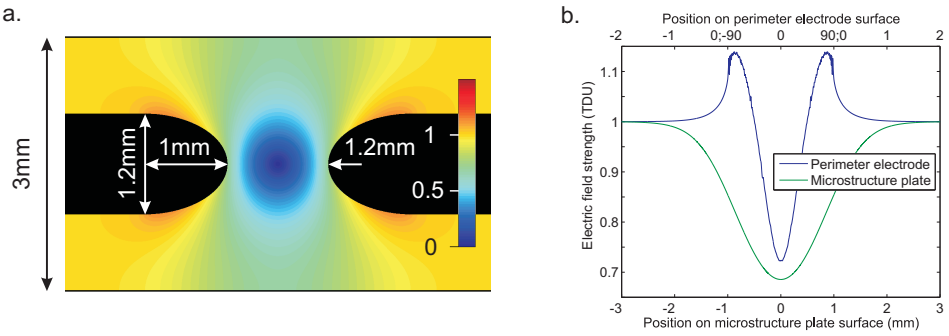

Figure 3.7: Capacitor-plate-based guide for the input and output channel of the trap. **a.** Electrode dimensions and simulated electric field strength distribution in trap depth units. The extensions of the trap perimeter electrodes are on the left and on the right and the trap capacitor plates are on top and on bottom. The 1.2 mm label on the right denotes the separation between the front edges of the perimeter electrodes. **b.** Electric field strength at the surface of the electrodes. The position on the perimeter guide electrode is parameterized as in Fig. 3.5.

3.5.3 Transition from the trap to the capacitor-plate-based guide

Starting from the capacitor-plate-based guide, the transition to the trap is completed by bending the two perimeter electrodes outwards. In terms of providing a sufficient potential depth, the design of this region is relatively uncritical. Keeping the transverse shape of the perimeter electrode constant, the electric field on the perimeter electrode surface is everywhere at least as large as for the capacitor-plate-based guide. Moreover, the outward bend of the perimeter electrodes helps to rapidly increase this field beyond the trap depth. Concerning the capacitor plates, the microstructure assumes the role of ensuring a high electric field at the surface.

The other criterion for the trap-guide transition, maintaining a wide channel of low electric field, might also seem uncritical considering the increasing separation between the perimeter electrodes. However, a rapid transition between the trap and the guide will result in strong electric potential gradients along the guide axis, potentially eliminating the channel of low electric field altogether. In fact, the electric potential in the center of the trap is equal to the voltage applied to the capacitor plates whereas the electric potential on the axis of our capacitor-plate-based guide is calculated to be 0.7893 times the voltage applied to the perimeter electrode relative to the capacitor plate voltage. Since the path integral of the electric field along any path from the trap to the guide is equal to the potential difference at the endpoints, maintaining an electric field zero on the axis of the guide is impossible.

To achieve a low electric field in the input and output channel of the trap, the trap-guide transition needs to extend over a sufficient distance. Moreover, for a fixed trap-guide separation, minimizing the maximum electric field on the guide axis requires a uniform electric potential gradient along the guide axis to be realized. These are the two key

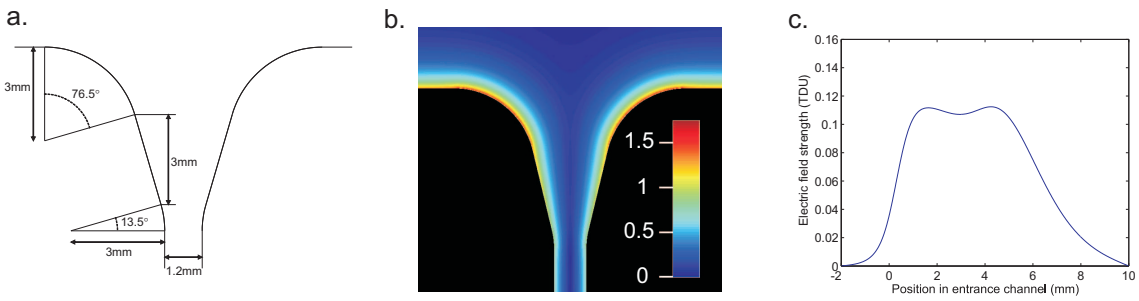

Figure 3.8: Connection of the capacitor-plate-based guide to the trap. For the position relative to the rest of the trap see Fig. 3.3. **a.** Specification of the line defining the front edge of the perimeter electrodes. This geometry was chosen to minimize the maximal electric field strength on the axis of the guide. **b.** Simulated electric field strength distribution in trap depth units in the plane midway between the two capacitor plates. **c.** Simulated electric field strength on the axis of the guide.

criteria which determine the design of the capacitor-plate-based guide to trap transition shown in Fig. 3.8a. The design results in an electric field strength distribution in the plane midway between the capacitor plates and an electric field strength on the axis of the guide as shown in Figs. 3.8b and c, respectively. We achieve a decent result in terms of uniformly spreading the change in the electric potential over a large distance, with the electric field maintained near 11 % of the trap depth over a distance of about 4 mm, corresponding to about 60 % of the required change in the electric potential. Further decreasing the electric field on the guide axis would require the length of the trap-guide transition to be further increased, but this also has disadvantages such as further increasing the required width of the glass substrate for the microstructure. Note that the maximal electric field strength on the guide axis of 11.2 % of the trap depth completely prevents molecules with an energy less than this value from entering or exiting the trap.

3.5.4 Matching a capacitor-plate-based guide to a standard quadrupole

The final element in the trap to guide transition is the transition from the capacitor-plate-based guide to a normal quadrupole. For equal voltages applied to the electrodes at both ends of the transition, a necessity if a gap in the electrodes is to be avoided, the change in the electric potential on the guide axis for this transition is only 0.2893 times the perimeter electrode to plate electrode voltage difference. Achieving a small electric field along the guide axis is therefore less difficult than for the transition from the capacitor-plate-based guide to the trap. However, for equal voltages, simultaneously matching the potential depth as well as the width of the low-field channel for both quadrupoles is impossible. This is because for fixed voltages, the product of the potential depth of the guide and the width of the low field channel which can be occupied by a molecule with a given transverse energy is more favorable, i.e. larger, for a normal quadrupole than for a capacitor-plate-based guide.

The difficulty in matching the two quadrupole guides can be seen from Fig. 3.9, showing

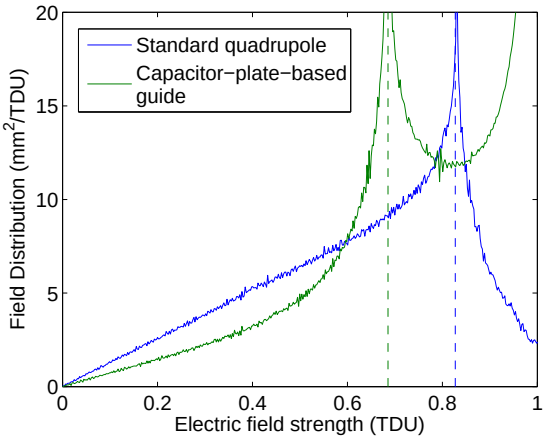

Figure 3.9: Simulated electric field strength distribution for both the capacitor-plate-based guide as well as for a standard quadrupole guide (the latter consisting of electrodes of radius 1 mm with a 1 mm spacing between neighboring electrodes). The vertical dashed lines denote the transverse potential depth of the two guides. We assume that the same voltages are applied to the quadrupole electrodes as are applied to the perimeter and plate electrodes in the trap.

the two electric field strength distributions for the guides with the dimensions used in the experiment. Due to the calculated 1.329 times faster increase of the electric fields with distance from the guide symmetry axis for the capacitor-plate-based guide, the guide area for low energy molecules is almost 1.8 times smaller than for the standard quadrupole, despite the fact that the standard quadrupole has a 1.207 times higher potential depth. Trying to match the width of the low-field channel for the two guides by increasing the trap dimensions relative to the standard quadrupole dimensions would further increase the potential depth mismatch and trying to match the potential depths would further increase the mismatch in the width of the low-field channel. A compromise between the two was chosen for the experiment, with this match ultimately determining the overall scaling of the trap dimensions as discussed in section 3.3. Assuming the resulting high fields in the quadrupole wouldn't limit the trap voltages, a better choice in retrospect would have been to focus entirely on matching the width of the low-field channel. While this would further reduce the fraction of the area of the standard quadrupole containing molecules which can be loaded into the trap, the molecules confined to this area could be loaded into the trap with 100% efficiency. Moreover, the design of a molecule source to load the quadrupole could be optimized taking into account the reduced effective width of the quadrupole.

Concerning the actual connection between the capacitor-plate-based guide and the standard quadrupole, any interpolation between the two shapes spread out over a sufficient distance along the guide should serve as an efficient connection. As a result, the exact shape of the transition was determined by the computer aided design software used to design the trap.

3.5.5 An alternative approach to the trap-guide transition

Two problems have been identified with the approach to the trap-guide transition presented so far. First, the width of the low-field channel for the capacitor-plate-based guide is quite small compared to the capacitor plate separation. Second, matching both the depth and the width of the capacitor-plate-based guide to a standard quadrupole is not possible. The second problem could in principle be solved by interrupting the quadrupole electrodes and applying a different set of voltages to the standard quadrupole than to the capacitor-plate-based guide. Here, we briefly sketch an idea based on this theme which might solve the first problem as well.

The idea would be to abruptly change the transverse shape of the guide at the end of the capacitor-plate-based guide. If the microstructures could maintain high fields sufficiently close to the edge of the capacitor plates, then the separation between the two perimeter guide electrodes in the capacitor-plate-based guide could be substantially increased, thereby increasing the width of the channel of low electric field. Once the microstructure ends, the abrupt change in the shape of the guide electrodes at the end of the capacitor plates would need to provide sufficiently high fields on the plate guide electrodes to compensate the lack of the microstructure fields. A brief decrease in the field strength at the plate guide electrode surface would potentially be acceptable, as long as most molecules fly by without being lost. An abrupt change in the quadrupole shape would of course require the electric potential on the axis of both guides to be practically identical. Whether all these challenges with such a design can be solved remains to be seen.

3.6 Design of the trap microstructure

The most important trap element to achieve confinement of molecules is the microstructuring of the surface of the capacitor plates. Here, the goal of an optimal design is again to provide strong confinement for the molecules but also to ensure that the relatively complicated microstructure fields don't facilitate any trap loss processes. As we shall see, the microstructure design for our trap also plays a substantial role in ensuring the homogeneity of the electric fields near the center of the trap.

An optimal design for a microstructure which is completely isolated in space is quite simple. Along the lines of Babinet's principle for optics [112], the electric field strength distribution above the microstructure remains unchanged if the electrodes and the gaps between the electrodes are interchanged, assuming reflection symmetry about the plane of the microstructure, translation symmetry along the microstructure, and electric fields which approach zero far away from the microstructure. As a result, the most uniform fields near the microstructure surface are achieved if the width of the microstructure electrodes of both polarity is equal to the width of the separation between adjacent electrodes. A microstructure design might then be realized as shown in Fig. 3.10.

The microstructure in the trap is by no means isolated from the rest of the trap, with the perimeter electrode field in particular strongly altering the electric fields produced by

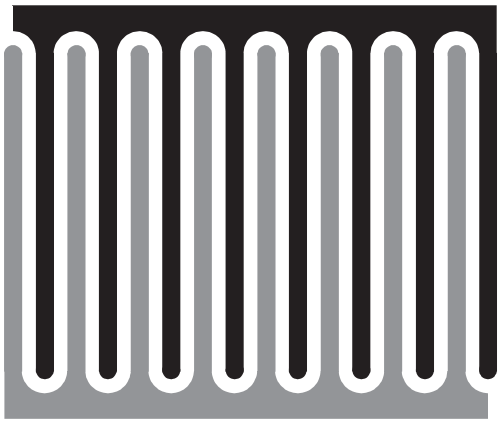

Figure 3.10: Elementary design for the trap microstructure. The black and the grey surface represent the electrodes of opposite polarity.

the microstructure and the offset field between the capacitor plates interfering with the microstructure fields as well. These field modifications result in severe problems in several respects. On the one hand, the perimeter electrode field points in the opposite direction and is therefore simply subtracted from the microstructure field at the surface of those microstructure electrodes with the same polarity as the perimeter electrode. This reduces the field strength on these microstructures electrodes by an amount equal to the trap depth. On the other hand, for an offset field perpendicular to the microstructure which is weaker than the electric field on the microstructure surface, the decay of the microstructure field away from the surface assures the existence of a line above every second microstructure electrode where the microstructure field and the offset field precisely cancel. These electric field zeros result in Majorana losses inside the trap and their persistence underneath the perimeter electrode creates holes in the trapping fields.

For the most part, the previous problems can be solved by varying the width of the individual microstructure electrodes. For this purpose, a detailed knowledge of the electric fields produced by the trap microstructure is required. We therefore consider how analytic solutions for the electric fields above the microstructure can be obtained in the next section and then use the solution in the subsequent sections to help address the challenges in designing the trap microstructure.

3.6.1 Analytic description of the electric fields above a periodic microstructure

An analytic solution for the electric potential near a periodic microstructure is in principle given by Eq. 3.16. However, this is true only as long as the potential coefficients Φ_0, E_0, and $\{a_n\}$ can be determined based on the boundary conditions at the microstructure surface. Determining these coefficients analytically is quite challenging but is in fact possible.

We begin by taking a closer look at the boundary conditions for the problem in sec-

tion 3.6.1.1. In particular, we show how the boundary conditions consisting of an electric potential being specified at the microstructure electrodes and a continuous electric field being required everywhere away from the electrodes is identical to mixed boundary conditions where the electric potential is specified at the electrodes and the surface normal electric field is specified in the plane of the microstructure away from the electrodes. These boundary conditions are applied to Eq. 3.16 in section 3.6.1.2, resulting in series equations for the potential coefficients.

In section 3.6.1.3, we show how the series equations for the potential coefficients can in principle be solved by applying what is essentially an inverse Fourier transform. However, due to the mixed boundary conditions, this gives rise to an infinite sequence of coupled linear equations for the potential coefficients. All attempts to solve these equations analytically were unsuccessful. While a solution is possible by truncating the sequence of linear equations and inverting them numerically, this procedure converges extremely slowly compared to the required computing resources and leaves open questions regarding convergence and the validity of the truncation, making this a rather unsatisfactory approach.

A completely analytic solution for the microstructure field is obtained in section 3.6.1.4 by adapting the techniques in Ref. [113] for solving mixed boundary value problems. Specifically, the series equations for the potential coefficients can be converted into integral equations for the electric potential and surface-normal electric field at the microstructure surface, which we then solve. This solution is general in that it is applicable for the case of an arbitrary position-dependent potential on the electrode surfaces and an arbitrary position-dependent surface-normal electric field between the electrodes. Moreover, we outline how the solution can be extended for an arbitrary periodic sequence of electrode strips.

For the special case of a constant potential on each microstructure electrode and a globally constant surface-normal electric field between the electrodes (the case we are interested in), a substantially simpler solution for the microstructure fields has been known in the context of surface acoustic wave interdigital transducers (see, e.g., Refs. [114] and [115] and references therein). Specifically, complex analytic functions can be used to write the electric field due to the microstructure directly in closed form. For completeness, this solution is presented in section 3.6.1.5.

3.6.1.1 Microstructure boundary conditions

The microstructure electrode geometry for which we wish to calculate the electric field is shown in Fig. 3.11. A periodic array of electrodes with periodicity d is located in the plane $y = 0$. A potential V_1 is applied to every second electrode of width w_1 and a potential V_2 is applied to every other electrode of width w_2. The electrodes are equally spaced resulting in reflection symmetry about each plane centered at and perpendicular to each microstructure electrode, indicated by the dashed lines. The origin is located at the center of one of the electrodes of width w_1, and the boundary condition for $y \to \pm\infty$ is a homogeneous electric field of magnitude $E_\pm$ pointing away from the surface. For the moment we assume the space on both sides of the microstructure to be filled by an unpolarizable medium. The required modification for a dielectric medium with an isotropic dielectric constant filling

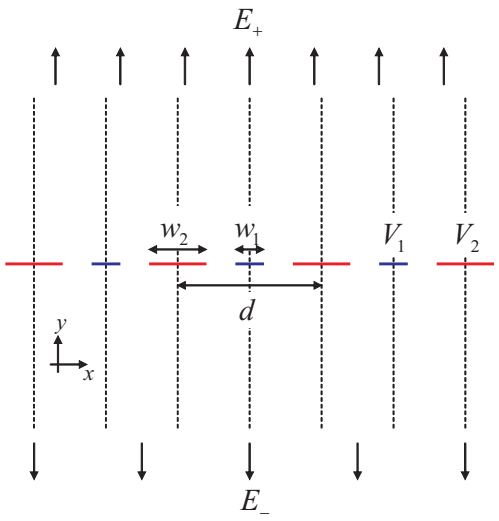

Figure 3.11: Boundary conditions for calculating the electric field near the trap microstructure.

the half-space $y < 0$ and/or $y > 0$ is considered below.

Let S_1 and S_2 be subsets of the real line such that the points $y = 0$, $x \in S_1$ correspond to the electrodes with potential V_1 and the points $y = 0$, $x \in S_2$ correspond to the electrodes with potential V_2. In this case, the boundary conditions for the electric potential $\Phi(x, y)$ are

$$\begin{aligned} \Phi(x,y)|_{x\in S_1, y=0} &= V_1 \\ \Phi(x,y)|_{x\in S_2, y=0} &= V_2 \\ \lim_{y\to\pm\infty} \frac{\partial\Phi(x,y)}{\partial y} &\pm E_\pm = 0. \end{aligned} \tag{3.21}$$

Moreover, $\Phi(x, y)$ satisfies the Laplace equation everywhere except at the electrodes. These conditions uniquely determine $\Phi(x, y)$ [112].

Determining the potential $\Phi(x, y)$ would be relatively easy if the potential were specified everywhere for $y = 0$. As a result we try to formulate a boundary condition for the non-electrode part of $y = 0$. We consider the modified potential $\Phi(x, y) + \frac{E_+ - E_-}{2} y$ consisting of a constant electric field $\frac{E_- - E_+}{2}\hat{\mathbf{y}}$ being superimposed on the desired electric field. The modified potential satisfies the same boundary conditions on $y = 0$ as $\Phi(x, y)$ but for $|y| \to \infty$ the boundary conditions are changed for both $y > 0$ and $y < 0$ into a constant electric field of magnitude $\frac{E_+ + E_-}{2}$ pointing away from the surface. The modified potential is therefore symmetric under reflection about the plane $y = 0$. The y-component of the modified electric field, being continuous everywhere except at the electrodes, must therefore vanish for $y = 0$, $x \notin S_1 \cup S_2$,

$$\left.\frac{\partial\Phi(x,y)}{\partial y} + \frac{E_+ - E_-}{2}\right|_{x\notin S_1\cup S_2, y=0} = 0. \tag{3.22}$$

We thus find the boundary condition at $y = 0$ to be a combination of Dirichlet boundary conditions, with the value of Φ specified at the electrodes, and Neumann boundary conditions, with the value of $\frac{\partial \Phi}{\partial y}$ specified away from the electrodes, such mixed boundary condition problems being notoriously difficult to solve [112].

We briefly consider the effect of dielectric media with dielectric constant ϵ^+ and ϵ^- filling the half-spaces $y > 0$ and $y < 0$, respectively. In this case, the electric potential $\Phi(x, y)$ still satisfies the Laplace equation and the boundary conditions in Eq. 3.21, with the only change being an additional condition at the interface between two dielectric media given by [112]

$$\begin{aligned} &\hat{\mathbf{n}} \cdot (\epsilon^+ \mathbf{E}^+ - \epsilon^- \mathbf{E}^-) = 0, \\ &\hat{\mathbf{n}} \times (\mathbf{E}^+ - \mathbf{E}^-) = 0. \end{aligned} \tag{3.23}$$

Here, $\mathbf{E}^\pm$ is the electric field in the limit $y \to 0^\pm$ and $\hat{\mathbf{n}} = \hat{\mathbf{y}}$ is the surface normal. Eq. 3.23 is surprisingly simple to satisfy once the solution for $\epsilon^+ = \epsilon^-$ is known. According to Eq. 3.22, the electric potential for $\epsilon^+ = \epsilon^-$ satisfies $\hat{\mathbf{n}} \cdot \mathbf{E}^+ = \hat{\mathbf{n}} \cdot \mathbf{E}^- = \frac{E_+ - E_-}{2}$. As a result, the solution for $\epsilon^+ = \epsilon^-$ with $E_+ = E_-$ satisfies Eq. 3.23 for arbitrary ϵ^+ and ϵ^- and is therefore identical to the solution for $\epsilon^+ \neq \epsilon^-$. To find the general solution for $E_+ \neq E_-$, we require a single specific solution with $E_+ \neq E_-$ in which case the general solution is given by a linear combination of the specific solution and a general solution with $E_+ = E_-$. Such a solution is given by

$$\Phi_s(x, y) = \begin{cases} \epsilon^- y & y > 0 \\ \epsilon^+ y & y < 0 \end{cases}. \tag{3.24}$$

Multiplying Φ_s by $\frac{E_+ - E_-}{\epsilon^+ + \epsilon^-}$ and adding this to the desired potential results in a modified potential for which $E'_+ = E'_- = \frac{\epsilon^+ E_+ + \epsilon^- E_-}{\epsilon^+ + \epsilon^-}$. The overall effect of a dielectric filling the half-space $y < 0$ and/or $y > 0$ is therefore nothing more than to modify Eq. 3.22, the modified version being

$$\left. \frac{\partial \Phi(x, y)}{\partial y} \right|_{x \notin S_1 \cup S_2, y = 0^\pm} = -\epsilon^\mp \frac{E_+ - E_-}{\epsilon^+ + \epsilon^-}. \tag{3.25}$$

3.6.1.2 Series equations for the potential coefficients

In its most general form, a potential with periodic boundary conditions on the surface $y = 0$ approaching a constant electric field $E_\pm$ for $y \to \pm\infty$ can be written as

$$\Phi(x, y) = \Phi_0 - E_\pm |y| + \sum_{n=1}^{\infty} \left(a_n \cos\left(\frac{2\pi n}{d} x\right) + b_n \sin\left(\frac{2\pi n}{d} x\right) \right) \exp\left(-\frac{2\pi n}{d} |y|\right), \tag{3.26}$$

where E_+ is used for $y > 0$ and E_- is used for $y < 0$. This expression automatically satisfies the Laplace equation $\nabla^2 \Phi(x, y) = 0$ for $y \neq 0$ as well as the boundary conditions for $|y| \to \pm\infty$. The terms $\sin(\frac{2\pi n}{d} x)$ are important later when we consider arbitrary periodic

sequences of electrode, but for now, the reflection symmetry about $x = 0$ results in $b_n = 0$ for all n, leading us back to Eq. 3.16.

We match the coefficients Φ_0 and $\{a_n\}$ to the boundary conditions at the surface $y = 0$. Due to the periodicity and the reflection symmetry we can restrict our attention to the range $0 \leq x \leq d/2$. With a bit of algebra, we find that Eqs. 3.21 and 3.25 are identical to

$$\begin{cases} \sum_{n=0}^{\infty} a_n \cos(n\,x) = V_1 & 0 \leq x \leq c_1 \\ \sum_{n=0}^{\infty} n\,a_n \cos(n\,x) = -\frac{d}{2\pi}\frac{\epsilon^+ E_+ + \epsilon^- E_-}{\epsilon^+ + \epsilon^-} & c_1 < x < c_2 \\ \sum_{n=0}^{\infty} a_n \cos(n\,x) = V_2 & c_2 \leq x \leq \pi \end{cases}, \tag{3.27}$$

with $a_0 = \Phi_0$, $c_1 = \frac{w_1}{d}\pi$, and $c_2 = \frac{d-w_2}{d}\pi$. This set of series equations is the compact mathematical formulation of the problem which we wish to solve.

3.6.1.3 An unsatisfactory numerical approach

If the factor n on the left hand side of the equation on the second line of Eq. 3.27 were absent, the left hand side of Eqs. 3.27 would simply be the Fourier expansion of the right hand side of Eqs. 3.27. The coefficients a_m could then be obtained by simply taking the inverse Fourier transform: multiplying by $\cos(m\,x)$ and integrating from 0 to π. A simple approach to try solving Eq. 3.27 would be to attempt the same procedure. Multiplying the equation on each line of Eq. 3.27 by $\cos(m\,x)$, integrating over the region where the respective equation holds and adding the three results, we obtain

$$\sum_{n=0}^{\infty} a_n (L_{n,m} + M_{n,m}) = A_m + B_m, \tag{3.28}$$

an infinite sequence of linear equations. Here,

$$L_{n,m} = \left(\int_0^{c_1} + \int_{c_2}^{\pi} \right) \cos(n\,x)\cos(m\,x) dx \tag{3.29}$$

and

$$A_m = \left(V_1 \int_0^{c_1} + V_2 \int_{c_2}^{\pi} \right) \cos(m\,x) dx, \tag{3.30}$$

are the contributions from the electrode part of the microstructure surface and

$$M_{n,m} = n \int_{c_1}^{c_2} \cos(n\,x)\cos(m\,x) dx, \tag{3.31}$$

and

$$B_m = -\frac{d}{2\pi}\frac{\epsilon^+ E_+ + \epsilon^- E_-}{\epsilon^+ + \epsilon^-} \int_{c_1}^{c_2} \cos(m\,x) dx. \tag{3.32}$$

are the contributions from the non-electrode parts of the microstructure surface.

Eqs. 3.28 can in principle be solved by inverting the matrix $\{L_{n,m} + M_{n,m}\}$ and multiplying by the vector $\{A_m + B_m\}$. Here we are thoroughly confronted with the challenge of

mixed boundary conditions compared to pure Dirichlet or Neumann boundary conditions. Whereas for both $c_1 = c_2$ (Dirichlet boundary conditions) and for $c_1 = 0$, $c_2 = \pi$ (Neumann boundary conditions) the matrix $\{L_{n,m} + M_{n,m}\}$ is diagonal, allowing its inverse to be found trivially, general values of c_1 and c_2 result in matrix elements $L_{n,m} + M_{n,m}$ which are messy nonzero linear combinations of trigonometric functions.

All attempts to invert the matrix $\{L_{n,m} + M_{n,m}\}$ analytically were unsuccessful. However, an approximate solution is possible by truncating the matrix and inverting it numerically. This is in fact the approach which was used to design the microstructure for the present trap. However, this approach is unsatisfactory in several respects. For one thing, inverting an $N \times N$ matrix numerically takes $\mathcal{O}(N^3)$ operations, and with the coefficients a_n approaching 0 relatively slowly for large n, obtaining a high accuracy result with this method seems impossible. Moreover, the approach leaves open a number of fundamental questions. For example, do the coefficients a_n even approach a constant value as the number of included coefficients becomes large, and if so, how? How is the expectation that to lead order $a_n = \mathcal{O}(n^{-3/2})$ for $n \to \infty$ due to the singularity at the edge of the electrodes and thus $a_n \to 0$ for $n \to \infty$ a consequence of Eqs. 3.28-3.32? Why should the Fourier coefficients for a function which is zero for $c_1 < x < c_2$ automatically be in the null space of the matrix $\{M_{n,m}\}$? Supporting these assertions numerically is relatively easy, but their analytic justification based on Eqs. 3.28-3.32 remains completely unclear.

3.6.1.4 General solution via integral equations

We now present a successful analytic approach to solving Eq. 3.27 based on the methods in Ref. [113]. For convenience, we define the subsets I_1 and I_2 of the interval $0 \leq x \leq \pi$ according to

$$\begin{aligned} I_1 &= \{x \,|\, 0 \leq x \leq c_1 \text{ or } c_2 \leq x \leq \pi\}, \\ I_2 &= \{x \,|\, c_1 < x < c_2\}, \end{aligned} \tag{3.33}$$

these being the electrode and the non-electrode part of the microstructure surface on this interval, respectively. Eq. 3.27 can then be generalized as

$$\sum_{n=0}^{\infty} a_n \cos(nx) = \begin{cases} H(x) & x \in I_1 \\ h(x) & x \in I_2 \end{cases}, \tag{3.34}$$

and

$$\sum_{n=0}^{\infty} n\, a_n \cos(nx) = \begin{cases} g(x) & x \in I_1 \\ G(x) & x \in I_2 \end{cases}. \tag{3.35}$$

Here $H(x)$ and $G(x)$ are known functions defined exclusively on I_1 and I_2, respectively, and $h(x)$ and $g(x)$ are unknown functions defined on the intervals I_2 and I_1. $H(x)$ is an arbitrary electric potential specified on the microstructure electrode surface, $G(x)$ is proportional to an arbitrary surface-normal electric field specified on the non-electrode part of the microstructure surface, $h(x)$ is the resulting electric potential on the non-electrode

part of the microstructure surface, and $g(x)$ is proportional to the resulting surface-normal electric field on the microstructure electrode surface.

Determining either $h(x)$ or $g(x)$ in terms of $H(x)$ and $G(x)$ would solve our problem since the coefficients $\{a_n\}$ could then be obtained via an inverse Fourier transform. In fact,

$$a_n = \frac{2-\delta_{0,n}}{\pi}\left(\int_{I_1} H(t)\cos(nt)dt + \int_{I_2} h(t)\cos(nt)dt\right), \tag{3.36}$$

with our focus from here on being determining the function $h(x)$. Inserting this expression into Eq. 3.35, we obtain

$$G(x) = \left(\int_{I_1} H(t) + \int_{I_2} h(t)\right) dt \sum_{n=0}^{\infty} \frac{2-\delta_{0,n}}{\pi} n\,\cos(nx)\cos(nt) \tag{3.37}$$

where $x \in I_2$. This equation can be simplified considerably by noting that

$$\sum_{n=0}^{\infty} 2\sin(nx)\cos(nt) = \frac{\sin(x)}{\cos(t)-\cos(x)}. \tag{3.38}$$

This equation is true in the sense that we multiply the left hand side by $e^{-\varepsilon n}$ and take the limit $\varepsilon \to 0$. Making use of Eq. 3.38 in Eq. 3.37, we find

$$G(x) = \frac{1}{\pi}\frac{d}{dx}\left[\int_{I_1} \frac{\sin(x)H(t)dt}{\cos(t)-\cos(x)} + \int_{I_2} \frac{\sin(x)h(t)dt}{\cos(t)-\cos(x)}\right]. \tag{3.39}$$

Moving the known part of the right hand side of this equation to the left hand side, and defining this as a new known function $\tilde{G}(x)$, we obtain

$$\tilde{G}(x) = G(x) - \frac{1}{\pi}\frac{d}{dx}\int_{I_1} \frac{\sin(x)H(t)dt}{\cos(t)-\cos(x)} = \frac{1}{\pi}\frac{d}{dx}\int_{I_2} \frac{\sin(x)h(t)dt}{\cos(t)-\cos(x)}, \tag{3.40}$$

where again $x \in I_2$. We thus obtain an integral equation for the unknown function $h(x)$ in terms of the known function $\tilde{G}(x)$ exclusively involving the interval I_2. This is a big improvement since we must no longer simultaneously satisfy a second condition involving the interval I_1. To solve Eq. 3.40, we note that

$$\begin{aligned}\int_{c_1}^{c_2} \frac{\sin(x)dx}{(\cos(t_1)-\cos(x))(\cos(t_2)-\cos(x))}\sqrt{\frac{\cos(c_1)-\cos(x)}{\cos(x)-\cos(c_2)}} = \\ \pi^2\sqrt{\frac{\cos(c_1)-\cos(t_1)}{\cos(t_1)-\cos(c_2)}}\,\delta(\cos(t_1)-\cos(t_2))\end{aligned} \tag{3.41}$$

which holds for arbitrary $t_1, t_2 \in I_2$. To obtain this result, we set $u = \cos(x)$, $du = -\sin(x)dx$, $a_1 = \cos(c_1)$, $a_2 = \cos(c_2)$, $b_1 = \cos(t_1)$, and $b_2 = \cos(t_2)$, in which case the

integral in Eq. 3.41 can be performed step by step according to

$$\begin{aligned}
&\int_{a_2}^{a_1} \frac{du}{(u-b_1)(u-b_2)} \sqrt{\frac{a_1-u}{u-a_2}} = \\
&\mathrm{Re}\, \frac{d}{db_2} \int_{-\infty}^{\infty} du\, \frac{\log|b_2-u|}{b_1-u} \sqrt{\frac{a_1-u}{u-a_2}} = \\
&\mathrm{Re}\, \frac{d}{db_2} \int_{-\infty+i\varepsilon}^{\infty+i\varepsilon} du\, \frac{\log(u-b_2) - i\pi\theta(b_2-u)}{b_1-u} \sqrt{\frac{a_1-u}{u-a_2}} = \\
&\mathrm{Im}\, \pi \frac{d}{db_2} \int_{-\infty+i\varepsilon}^{b_2+i\varepsilon} \frac{du}{b_1-u} \sqrt{\frac{a_1-u}{u-a_2}} = \\
&\pi^2 \sqrt{\frac{a_1-b_1}{b_1-a_2}}\, \delta(b_1-b_2).
\end{aligned} \tag{3.42}$$

Here, we make use of the fact that the integrand on the first line is pure imaginary everywhere outside the range of integration as well as the fact that a contour integral of a complex analytic function on a closed path in the complex plain is zero. The $i\varepsilon$ in the limits of integration on the third and fourth line denotes the integral being performed for an infinitesimally positive imaginary value of u.

Obtaining the solution to Eq. 3.40 with use of Eq. 3.41 is straightforward, and results in

$$h(t) = \frac{\sin(t)}{\pi} \int_{c_1}^{c_2} \frac{dx}{\cos(t)-\cos(x)} \sqrt{\frac{\cos(c_1)-\cos(t)}{\cos(c_1)-\cos(x)} \frac{\cos(x)-\cos(c_2)}{\cos(t)-\cos(c_2)}} \int_x \tilde{G}(x')dx'. \tag{3.43}$$

This can be easily checked by inserting Eq. 3.40 for $\tilde{G}(x)$ into this equation and applying Eq. 3.41. The one remaining issue which needs to be addressed is the constant of integration for the indefinite integral over $\tilde{G}(x)$. It would be convenient if the constant of integration could be chosen arbitrarily, which would be the case if changing the constant of integration left $h(t)$ unchanged, but this is wrong. The constant of integration must thus have been defined implicitly somewhere along the way. In fact, Eq. 3.43 only follows from Eq. 3.40 if

$$\int_x \tilde{G}(x')dx' = \frac{1}{\pi} \int_{I_2} \frac{\sin(x)h(t)dt}{\cos(t)-\cos(x)}, \tag{3.44}$$

leaving no room for an arbitrary constant of integration.

To determine the constant of integration non-circularly, i.e. without knowing $h(t)$ in advance, we note that for arbitrary $t \in I_2$,

$$\int_{I_2} \frac{dx}{\sqrt{(\cos(c_1)-\cos(x))(\cos(x)-\cos(c_2))}} \frac{\sin(x)}{\cos(t)-\cos(x)} = 0. \tag{3.45}$$

Multiplying by $h(t)$ and integrating t over I_2, we find that

$$\int_{I_2} \frac{dx}{\sqrt{(\cos(c_1)-\cos(x))(\cos(x)-\cos(c_2))}} \int_x \tilde{G}(x')dx' = 0. \tag{3.46}$$

However, this only holds if the constant of integration assumes the correct value, and can therefore be used to determine its value.

So far, the derivation of the electric field above the microstructure has focused exclusively on the electrode geometry shown in Fig. 3.11. However, the approach can easily be extended to an arbitrary periodic microstructure, and we briefly outline the key changes this introduces into the derivation.

Let $a_1, ..., a_N$ and $b_1, ..., b_N$ be a set of $2N$ numbers which satisfy $0 < a_1 < b_1 < a_2 < b_2 < ... < a_N < b_N < 2\pi$. These numbers correspond to a periodic sequence of electrodes with N electrodes per period in the plane $y = 0$ where the intervals $a_i < x < b_i$ correspond to the gaps between the electrodes. For a reason given below, N must be an even integer. If the base microstructure period contains an odd number of electrodes, we can simply double the period length. We again define subsets I_1 and I_2 of the interval $0 \leq x \leq 2\pi$ corresponding to the electrode and non-electrode part of the microstructure period, so that

$$I_2 = \bigcup_{i=1}^{N} \{x | a_i < x < b_i\} \tag{3.47}$$

and I_1 is equal to the complement to I_2 in $0 \leq x \leq 2\pi$.

Unlike the specific geometry in Fig. 3.11, a general electrode geometry usually won't be symmetric under reflection about a plane perpendicular to the microstructure. As a result, the expansion of the electric potential above the microstructure surface is given by the full expression in Eq. 3.26 with both the sine and the cosine terms contributing. The boundary condition at the microstructure surface is then given by

$$\sum_{n=0}^{\infty} a_n \cos(nx) + b_n \sin(nx) = \begin{cases} H(x) & x \in I_1 \\ h(x) & x \in I_2 \end{cases} \tag{3.48}$$

and

$$\sum_{n=0}^{\infty} n(a_n \cos(nx) + b_n \sin(nx)) = \begin{cases} g(x) & x \in I_1 \\ G(x) & x \in I_2 \end{cases}, \tag{3.49}$$

in analogy to Eqs. 3.34 and 3.35.

Following the same steps as before, we again obtain an integral equation for $h(t)$ in terms of a known function $\tilde{G}(x)$,

$$\tilde{G}(x) = G(x) - \frac{1}{2\pi}\frac{d}{dx}\int_{I_1} H(t) \cot\left(\frac{x-t}{2}\right) dt = \frac{1}{2\pi}\frac{d}{dx}\int_{I_2} h(t) \cot\left(\frac{x-t}{2}\right) dt. \tag{3.50}$$

The integral equation can again be solved, by noting that

$$\begin{aligned} \int_{I_2} dx \cot\left(\frac{x-t_1}{2}\right) \cot\left(\frac{x-t_2}{2}\right) \left[-\prod_{i=1}^{N} \frac{1}{\sin\left(\frac{x-a_i}{2}\right)\sin\left(\frac{x-b_i}{2}\right)}\right]^{1/2} = \\ 4\pi^2 \left[-\prod_{i=1}^{N} \frac{1}{\sin\left(\frac{t_1-a_i}{2}\right)\sin\left(\frac{t_1-b_i}{2}\right)}\right]^{1/2} \delta(t_1 - t_2). \end{aligned} \tag{3.51}$$

with $t_1, t_2 \in I_2$. In order for this equation to hold, we must make sure to evaluate the square root with the correct sign. In particular, the square root as a function of x or t_1 must be extendable to a complex analytic function in the entire upper half of the complex plane. This is only possible if the square root is alternatingly evaluated as positive and negative on adjacent intervals in I_2. Eq. 3.51 also requires the square root to be evaluated with opposite sign on the leftmost and rightmost interval in I_2. This is inconsistent with the previous condition unless N is an even integer, as required above.

Using Eq. 3.51, we obtain

$$h(t) = \frac{1}{2\pi} \int_{I_2} dx \cot\left(\frac{x-t}{2}\right) \left[\prod_{i=1}^{N} \frac{\sin\left(\frac{t-a_i}{2}\right)\sin\left(\frac{t-b_i}{2}\right)}{\sin\left(\frac{x-a_i}{2}\right)\sin\left(\frac{x-b_i}{2}\right)}\right]^{1/2} \int_x \tilde{G}(x')dx'. \tag{3.52}$$

The same comments regarding the square root hold as above, with the sign chosen positive when t and x are in the same interval of I_2. Moreover, a total of N constants of integration must be determined for the indefinite integral over $\tilde{G}(x)$, for which equations similar to the one in Eq. 3.46 can be used.

Eq. 3.52 provides a general solution for the electric potential away from the plane $y = 0$ for arbitrary periodic mixed boundary conditions specified along the x-direction in the plane $y = 0$. Our result could most likely be further generalized to non-periodic boundary conditions as well. As such, it would be very interesting if our approach could be used to gain deeper insight into the mathematics of mixed boundary value problems, but this topic is clearly beyond the scope of this thesis.

3.6.1.5 Specific solution via complex analytic functions

Eq. 3.43 or Eq. 3.52 directly provide the electric potential for all of $y = 0$ and allow a number of quantities such as individual Fourier coefficients to be calculated relatively easily. However, determining the electric potential away from the microstructure surface requires a sufficiently large number of Fourier coefficients to be calculated and inserted into Eq. 3.26, a somewhat cumbersome process. It turns out that for a fixed (i.e. x-independent) potential applied to each microstructure electrode, equivalent to $\frac{dH}{dx} = 0$, and a uniform value of the surface-normal electric field on the entire non-electrode part of the microstructure surface, equivalent to $G(x) = \text{const.}$, a substantially simpler solution for the electric field in the entire $x - y$ plane exists, and has been known in the context of surface acoustic wave interdigital transducers [114, 115]. A quite well-written derivation of this solution has been presented in Ref. [114], but only for a finite (and therefore non-periodic) set of microstructure electrodes. We show how a similar derivation can be applied to the periodic case.

We consider the electrode geometry where the non-electrode part of a microstructure period, corresponding to the interval $0 \leq x \leq 2\pi$, is given by I_2 defined by Eq. 3.47, with the electrode part being its complement, I_1. An electric potential V_j is applied to the electrode at $b_j \leq x \leq a_{j+1}$ for $j = 0, ..., N$, where $V_0 = V_N$ and where we define $b_0 = 0$ and $a_{N+1} = 2\pi$. Adding a constant electric field perpendicular to the microstructure surface

leaves the electric potential on the microstructure surface unchanged. We can therefore assume that the surface-normal electric field on the non-electrode part of the microstructure surface is zero and that the electric field approaches a constant value of $E_0\hat{\mathbf{y}}$ far away from the surface.

Let $\mathbf{E}(x,y) = E_x(x,y)\hat{\mathbf{x}} + E_y(x,y)\hat{\mathbf{y}}$ for $y > 0$ be the electric field corresponding to the microstructure geometry and boundary conditions just described. It is well known that any solution to the Laplace equation in two dimensions can be written as the real part of a complex analytic function defined on the complex plane. As a result, for $z = x + iy$, the function $E(z) = E_x(\operatorname{Re} z, \operatorname{Im} z) - iE_y(\operatorname{Re} z, \operatorname{Im} z)$ is a complex analytic function for $\operatorname{Im} z > 0$. It turns out that the function $E(z)$ has a surprisingly simple form.

We convert the boundary conditions for the electric potential into conditions imposed on the function $E(z)$. The boundary condition on the electrode part of the microstructure surface results in $\operatorname{Re} E(x)|_{x\in I_1} = 0$ and the boundary condition on the non-electrode part of the microstructure surface is identical to $\operatorname{Im} E(x)|_{x\in I_2} = 0$. The boundary condition for $y \to \infty$ is identical to $E(z) = -iE_0$ for $\operatorname{Im} z \to \infty$. We are thus looking for a function which is complex analytic in the entire upper half of the complex plane and which is pure imaginary on parts of the real line and pure imaginary on the rest of the real line. A simple example for such a function, albeit with the regions where it is real or imaginary being incorrect, is $\sqrt{z}$. The same is of course true for the function $\sqrt{z-a}$ for arbitrary real values of a as well as for the product of any number of such functions with different values of a. The final ingredient we need to venture a first guess as to the form of $E(z)$ is the well known fact that the electric field at the end of an infinitely thin electrode in two dimensions can be described by $1/\sqrt{z}$. We thus consider the expression

$$\sqrt{-\prod_{j=1}^{N}\prod_{n=-\infty}^{\infty}\frac{1}{(1-\frac{z}{a_i-2\pi n})(1-\frac{z}{b_i-2\pi n})}}\,, \tag{3.53}$$

which automatically satisfies the conditions for $E(z)$ on the real line. This expression is proportional to

$$\tilde{E}(z) = \sqrt{-\prod_{j=1}^{N}\frac{1}{\sin\left(\frac{z-a_i}{2}\right)\sin\left(\frac{z-b_i}{2}\right)}}\,, \tag{3.54}$$

as can easily be shown using the identity

$$\sin\left(\frac{z-a}{2}\right) = -\sin(a/2)\prod_{n=-\infty}^{\infty}\left(1-\frac{z}{a-2\pi n}\right). \tag{3.55}$$

$\tilde{E}(z)$ in fact represents the correct solution for the electric field when $E_0 = 0$ and when a specific set of voltages are applied to the electrodes: the real part of the integral of $\tilde{E}(z)$ then satisfies the boundary conditions for the electric potential and is therefore equal to the electric potential by the uniqueness theorem for potential problems with mixed boundary conditions [112].

We consider if $\tilde{E}(z)$ can be modified to allow for both $E_0 \neq 0$ as well as for a general set of microstructure voltages. We begin by noting that $\tilde{E}(z) = 0$ is satisfied nowhere in the complex plane. $\tilde{E}(z)$ thus corresponds to a set of voltages applied to the microstructure electrodes such that no electric field zeros exist. In contrast, general voltages applied to the microstructures electrodes most certainly can result in electric field zeros. Electric field zeros can easily be incorporated. Thus, the product $(z-a)\tilde{E}(z)$ and the product $((z-a)^2+b^2)\tilde{E}(z)$ for real a and b have zeros at $z = a$ and at $z = a \pm ib$, respectively while still satisfying the condition for $E(z)$ on the real line. These products, however, are no longer periodic functions, but this can easily fixed by adding a whole sequence of zeros spaced by 2π. Using Eq. 3.55 plus some trigonometry in the second case, this is easily shown to be identical to multiplying by $\sin(\frac{z-a}{2})$ for zeros on the real line or by $\frac{1}{2}(\cosh(b) - \cos(z-a))$ for zeros in the complex plane. We thus obtain a solution for $E(z)$ for general microstructure voltages given by

$$E(z) = A\frac{\prod_{j=1}^{N_r} \sin\left(\frac{z-r_j}{2}\right) \prod_{j=1}^{N_c} \frac{1}{2}(\cosh(s_j) - \cos(z-t_j))}{\sqrt{-\prod_{j=1}^{N} \sin\left(\frac{z-a_i}{2}\right) \sin\left(\frac{z-b_i}{2}\right)}}. \tag{3.56}$$

Here, $r_1, ..., r_{N_r} \bmod 2\pi$ are the real zeros of $E(z)$ and $s_j \pm i\, t_j \bmod 2\pi$ for $j = 1, ..., N_c$ are the complex zeros of $E(z)$. A is a real constant. The boundary condition for $\operatorname{Im} z \to \infty$ provides a constraint for the value of N_r and N_c. We have

$$\lim_{z \to i\infty} E(z) = \lim_{z \to i\infty} \frac{A}{i} \exp\left[i \left(\sum_{j=1}^{N_r} \frac{r_j}{2} + \sum_{j=1}^{N_c} t_j - \sum_{j=1}^{N} \frac{a_i + b_i}{4} \right) \right] \exp\left[\frac{(N_r + 2N_c - N)z}{2i} \right]. \tag{3.57}$$

As a result, for $E_0 = 0$, we require $N_r + 2N_c < N$, and for $E_0 \neq 0$, we require $N_r + 2N_c = N$. Moreover, for $E_0 \neq 0$, we require $\sum_{j=1}^{N_r} \frac{r_j}{2} + \sum_{j=1}^{N_c} t_j - \sum_{j=1}^{N} \frac{a_i+b_i}{4}$ to either be an even multiple of π, in which case $A = E_0$, or an odd multiple of π, in which case $A = -E_0$. Note that this choice of sign pins down the sign which the square root in Eq. 3.56 must take, due to the fact that $E(z)$ is complex analytic and therefore continuous in the entire upper half of the complex plain. Finally, we see that for $E(z)$ to be a periodic function with period 2π, $N - N_r$ must be an even integer.

The constraints on the free parameters in Eq. 3.56 result in exactly the number of degrees of freedom necessary to match N voltages on the microstructure electrodes plus the value of E_0. Thus, for $E_0 \neq 0$, we have up to N distinct values of r_j, s_j, and t_j which must fulfill one constraint, providing $N - 1$ degrees of freedom. The value of A accounts for the value of E_0, and the integration constant when integrating the electric field to obtain the potential accounts for final required degree of freedom. For $E_0 = 0$ the maximal number of distinct values of r_j, s_j, and t_j is reduced by two since $N - N_r$ must be even. With the value of A no longer bound to the value of E_0, we again obtain the required number of degrees of freedom.

A rigorous proof that the set of solutions defined by Eq. 3.56 accounts for all possible values of the microstructure electrode voltages plus the value of E_0 could now proceed

as follows. One first needs to show that the set of functions defined by Eq. 3.56 is an N-dimensional linear space. Together with the integration constant when calculating the electric potential from the electric field, this space maps linearly to the set of electrode voltages plus E_0. Since this mapping is one-to-one due to the uniqueness theorem for potential problems with mixed boundary conditions, the equal dimensionality of both spaces requires the mapping to automatically be onto.

We conclude this section by applying Eq. 3.56 to the original microstructure geometry shown in Fig. 3.11. Here, $N = 2$, and we have $a_1 = c_1$, $b_1 = c_2$, $a_2 = 2\pi - c_2$, and $b_2 = 2\pi - c_1$. Due to the reflection symmetry about $y = 0$, Eq. 3.56 can be simplified considerably and we obtain

$$E(z) = \frac{A + E_0 \cos(z)}{\sqrt{(\cos(c_1) - \cos(z))(\cos(z) - \cos(c_2))}}, \tag{3.58}$$

with the constant A determined by

$$\int_{c_1}^{c_2} E(z)dz = V_1 - V_2. \tag{3.59}$$

Eq. 3.58 substantially simplifies the calculation of the microstructure fields used in the following sections.

3.6.2 General microstructure design considerations

Before considering the main specific problems which need to be addressed with the microstructure design, we briefly discuss several general issues regarding the microstructure realization. As mentioned in section 3.3, the periodicity chosen for the trap microstructure is 0.8 mm. For a regular microstructure, with all electrodes of equal width along the lines of Fig. 3.10, this would result in a width for both the electrodes as well as for the gaps in between of 0.2 mm. We consider the voltages which would need to be applied to such a microstructure in the absence of any offset fields to obtain an electric field strength on the microstructure surface which is everywhere at least equal to the nominal trap depth. According to the results from the previous section, a voltage of $\pm V_\mu$ applied to the microstructure electrodes results in a minimal field strength on the microstructure surface of $5.99\, V_\mu\, \mathrm{mm}^{-1}$. This is equal to the nominal trap depth if a voltage difference of $5.39\, V_\mu$ is applied across the 0.9 mm between the trap perimeter electrode and the capacitor plate surface. For the actual trap, the optimal voltage applied to the perimeter electrode is, however, quite a bit lower. This is due to the modifications to the microstructure discussed in section 3.6.4 which, while essential for reducing trap losses, have the unfortunate side effect of reducing the minimal field strength on the microstructure surface. Maintaining the nominal trap depth on the microstructure surface therefore requires the ratio of the perimeter electrode voltage to the microstructure voltage to be reduced, and the trap is designed for optimal performance when, for a microstructure voltage of $\pm V_\mu$, a voltage of $3\, V_\mu$ is applied to the perimeter electrode.

In addition to ensuring that the electric field strength on the microstructure surface is everywhere at least equal to the nominal trap depth, it is desirable to limit the maximal electric fields on the microstructure surface in order to maximize the voltages which can be applied without breakdown. Purely theoretically, the maximal electric field strength on the microstructure surface is always infinite, due to the $1/\sqrt{z}$ divergence of the electric field near the edges of the electrodes. In practice, the maximal electric fields will therefore to a large part depend on the radii of curvature of the edges of the microstructure electrodes, and we expect the microstructure breakdown voltage to a large part to depend on the quality of these edges. Nonetheless, the proportionality factor for the $1/\sqrt{z}$ divergence at the microstructure edge also plays a big role in determining the maximal electric fields and minimizing this factor for a given set of microstructure voltages is therefore a key goal for an optimal microstructure design. Determining the proportionality factor for the $1/\sqrt{z}$ divergence using the theory from the previous section is quite straightforward. However, while designing the microstructure for the present trap, only the approach for calculating the microstructure fields from section 3.6.1.3 was available. This approach performs particularly poorly near the edges of the microstructure electrodes since truncating a Fourier series acts as a low pass filter. As a result, the microstructure was instead designed so as to limit the maximal value of the electric field minima at the center of the electrodes and near center of the gaps between the electrodes on the microstructure surface (see Fig. 3.12 for an example), in the hope that this results in lower electric fields near the edges of the microstructure electrodes as well.

3.6.3 Maintaining a strong microstructure confinement under the perimeter electrode

A first problem with a regular microstructure design as shown in Fig. 3.10 is the interaction of the strong electric field due to the traps' perimeter electrode with the microstructure field underneath the perimeter electrode. The perimeter electrode field has the opposite sign as the microstructure field on the surface of those microstructure electrodes with the same polarity as the perimeter electrode, reducing the electric field strength and thereby the trap confinement in the vicinity of these electrodes. At the same time, the electric field strength near the microstructure electrodes with the opposite polarity as the perimeter electrode is substantially increased. This can be seen by the dashed curve in Fig. 3.12, showing the electric field strength on the surface of a regular microstructure with a voltage of $\pm V_\mu$ applied to the microstructure electrodes and a voltage of $3\,V_\mu$ applied to an electrode (i.e. the perimeter electrode) 0.9 mm above the microstructure surface. As we can see, the trap depth would be reduced by just over 25 % despite an electric field strength at the center of the electrodes with opposite polarity as the perimeter electrodes which is almost three times the trap depth. For a higher perimeter electrode voltage relative to the microstructure voltage as discussed in the previous section, the problem would be even worse. Both here and below, we assume a relative dielectric constant $\epsilon^- = 6.2$ for the microstructures dielectric substrate, this being the dielectric constant of the AF45 glass

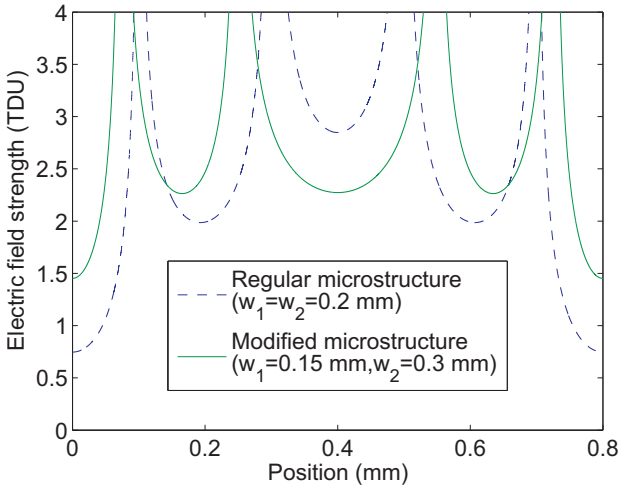

Figure 3.12: Expected electric field at the surface of the microstructure plate underneath the perimeter electrode for both a regular microstructure with $w_1 = w_2 = d/4$ as well as for the actual microstructure. d is the microstructure periodicity. The microstructure electrodes with the same polarity as the perimeter electrode are located at even multiples of 0.4 mm, those with opposite polarity at odd multiples of 0.4 mm. Modifying the electrode widths results in an increased trap confinement and a more uniform field strength at the plate surface.

used for the substrate.

The electric field strength at the surface of a microstructure electrode can be increased by decreasing the width of that electrode and vice versa. A simple solution to the present problem is thus to decrease the width of the microstructure electrodes with the same polarity as the perimeter electrode and to increase the width of the other electrodes. Here, the key goal is of course to ensure an electric field strength on the microstructure surface which is everywhere at least equal to the trap depth. This is easy to achieve for a wide range of values for the widths w_1 and w_2 of the microstructure electrodes. The remaining variability in w_1 and w_2 can be used to minimize the divergences in the electric fields near the edges of the electrodes, as discussed in the previous section. These conditions can be used to define optimal values $w_1(E)$ and $w_2(E)$ for the microstructure electrode widths as a function of a homogeneous offset field E far away from the microstructure surface. An optimized microstructure geometry could then be obtained by first calculating the electric field $E(\mathbf{x})$ on the capacitor plate surfaces in the trap if the microstructure is replaced by a solid electrode. The widths of the microstructure electrodes as a function of position on the capacitor plate surface $\mathbf{x}$ is then given by $w_1(E(\mathbf{x}))$ and $w_2(E(\mathbf{x}))$.

For the present trap microstructure, the width of the electrodes underneath the perimeter electrode with the same polarity as the perimeter electrodes is reduced to 0.15 mm and the width of the electrodes with the opposite polarity is increased to 0.3 mm. This results in an electric field strength on the microstructure surface shown by the solid curve in

Fig. 3.12. As can be seen, the electric field strength on the surface is now everywhere at least 45 % above the nominal trap depth. Simultaneously, the electric field strength on the electrode of opposite polarity to the perimeter electrode has been reduced. Changing the width of the microstructure electrodes thus allows the traps confining electric field strength to be maintained under the perimeter electrode without resorting to increased voltages on the microstructure electrodes.

3.6.4 Minimizing electric field zeros inside the trap

Considering the complex microstructure fields and their interaction with the perimeter electrode field, it can be expected that avoiding electric field zeros inside the trap will be somewhere between extremely difficult and impossible. As such, the prevalence of trap losses due to Majorana transitions is a key issue which needs to be addressed. For identical voltages applied to the microstructure on both capacitor plates of the trap, the electric field in the entire central region of the trap for a regular microstructure is vanishingly small, and molecules will be lost due to Majorana transitions almost instantly. An offset is then essential for successful trapping of molecules, but this by no means eliminates all electric field zeros. In fact, with the dominant contributions to the electric potential far away from the microstructure plate surface according to Eq. 3.16 given by

$$\Phi(x, y, z) = \Phi_0 + E_0\, y + a_1 \exp\left(\frac{-2\pi\, y}{d}\right) \cos\left(\frac{2\pi\,(x - x_0)}{d}\right), \tag{3.60}$$

we see that an electric field zero exists above every second microstructure electrode at $y \approx \frac{d}{2\pi} \log(\frac{2\pi\, a_1}{d\, E_0})$ where the microstructure field and the offset field precisely cancel.

We estimate the rate at which Majorana transitions will occur due to an electric field zero above every second microstructure electrode based on the approach in section 3.2.4.2. Linearizing Eq. 3.60 near the zero, we find that the electric field strength at a distance x_z from the zero is $|\mathbf{E}| = \frac{2\pi}{d} E_0 x_z$. Interestingly, this is independent of a_1, or equivalently, of the voltage difference between neighboring microstructure electrodes. For a more or less typical Stark splitting between neighboring rotational sublevels of 200 MHz/(kV/cm) and a typical value of E_0 in the experiment of 600 V/cm, we find that the constant c_E in Eqs. 3.12 and 3.13 is equal to $c_E = 940\,\mathrm{MHz/mm}$. As a result, for molecules with a velocity of 10 m/s, Majorana transitions are likely to occur when they pass by an electric field zero within a distance of approximately $b = 3.3\,\mu\mathrm{m}$. To apply Eq. 3.14 to obtain the loss rate, we must note a key difference in the situation here from the assumptions leading to Eq. 3.14. Eq. 3.14 assumes a point-like zero with the electric field increasing in all directions away from the zero. In contrast, the electric field zeros above every second microstructure electrode extend the entire length of the trap. As a result, one factor of b in Eq. 3.14 must be replaced by the width of the trap, i.e. 2 cm. For a total of 100 microstructure electrodes of one polarity on the two capacitor plates along the 4 cm length of the trap, we obtain a loss rate of

$$\Gamma = \frac{100 \times 2\,\mathrm{cm} \times 3.3\,\mu\mathrm{m} \times 10\mathrm{m/s}}{2.4\,\mathrm{cm}^3} = 27\,\mathrm{Hz}. \tag{3.61}$$

Thus, even with an offset field between the capacitor plates, Majorana transitions lead to catastrophic trap losses.

To achieve long trapping times, the electric field zeros above every second microstructure must be eliminated. From the standpoint of finding a suitable solution to the Laplace equation for the electric potential, this is relatively easy. Due to the translation symmetry along the microstructure, the electric fields they produce are confined to the plane perpendicular to the translation direction. The electric field zeros are therefore eliminated in the solution to the Laplace equation where a constant electric field pointing along the translation direction is added to the microstructure field. Such a field could be rather weak, with a strength which needs to be only slightly more than the microstructure field at a distance from the field zeros where Majorana transitions start to become likely. In the numerical example above, this is 15 V/cm. However, creating such a field configuration with a realistic set of electrodes is quite difficult. Unlike a magnetic trap, where an offset field can easily be added with an external set of coils, the trap electrodes act as a Faraday cage, shielding the trap volume from any external fields. Thus, even using the trap perimeter electrode to apply a voltage difference to opposite sides of the trap would create only a vanishingly small field along the trap microstructure in the center of the trap.

To achieve a component of the electric field along the microstructure electrodes requires a voltage gradient along the electrodes. One possibility would be to fabricate the microstructure electrodes out of a material with a high electrical resistivity and apply an electric current along the electrodes. This option was seriously considered while designing the trap and would be very interesting if a suitable material for the microstructure electrodes could be found. However, in the end a substantially simpler solution from a microstructure fabrication standpoint was found. As in the previous section, the idea is to play with the widths of the microstructure electrodes. Viewed from a distance, a microstructure with wider positive than negative electrodes will appear to have an overall positive voltage applied and vice versa for wider negative electrodes. This is reflected in the dependence of the constant Φ_0 in, e.g., Eq. 3.60 on the widths of the electrodes even for constant electrode voltages. As a result, an electric field along the trap microstructure can be obtained by tapering the widths of the electrodes, with the positive electrodes being wider on one side of the trap and the negative electrodes being wider on the other side.

Before considering the design of the microstructure taper, we discuss the key issue of calculating the electric fields which the tapered microstructure produces. Here, the theory from section 3.6.1 may at first seem inapplicable since the taper eliminates the translation symmetry along the microstructure. However, one can easily obtain an approximate electric potential $\tilde{\Phi}(x, y, z)$ (with z the direction along the microstructure) by solving the Laplace equation in two dimensions with z fixed for each value of z. Due to the slow variation in the electrode dimensions along the microstructure, this is an excellent approximation: Let $\theta_{\mu t}$ be the maximal angle between the z-axis and the tangent to the edge of the microstructure. By scaling the distance over which the microstructure taper occurs, it is relatively easy to show that the error in $\tilde{\Phi}(x, y, z)$ is on the order of $\theta_{\mu t}^2$. For the microstructure taper in the present trap, $\theta_{\mu t} = 0.0077$, and we thus expect the inaccuracy in assuming the electrode widths to be invariant under translation to calculate the potential at a given position z to

be on the order of $\theta_{\mu t}^2 = 6 \times 10^{-5}$.

3.6.4.1 Design of the tapered microstructure

In addition to the primary goal of achieving a sufficiently strong electric field along the microstructure, the choice of electrode widths for the microstructure taper is again guided by the need to maintain the trap depth and by the desire to limit the maximal electric field strength on the microstructure surface. Here, a large taper directly conflicts with a large trap depth since the former requires the electrode widths to deviate from the values which are optimal for the latter. As a result, the microstructure taper should be as small as possible to sufficiently suppress Majorana losses. Determining the minimal necessary microstructure taper requires knowledge of a wide range of parameters concerning the operation of the trap, including the choice of molecule species and the identity of the rotational molecular states to be trapped, and additionally requires a much more accurate model for Majorana losses than the one presented in section 3.2.4.2. These conditions were hardly fulfilled while designing the trap, and since suppressing Majorana losses is much more important than maximizing the trap depth, the microstructure taper was chosen to be substantially larger than it should need to be.

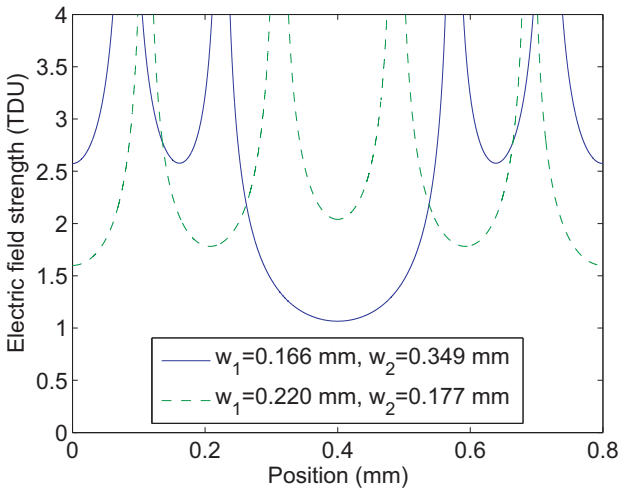

Figure 3.13: Electric field at the surface of a microstructure without any offset field for electrode widths as indicated. These widths represent the extreme values for the taper of the microstructure electrodes across the trap. The choice of these values is discussed in the text.

The values for the electrode widths w_1 and w_2 at one end of the microstructure taper were chosen to satisfy the following two conditions. First, for a voltage of $\pm V_\mu$ applied to the microstructure, the mean electric potential of the microstructure surface should be $-V_\mu/4$. Together with the mean potential at the other end of the microstructure taper, this determines the strength of the electric field along the trap microstructure, which needs

to be sufficiently large. Second, the minimal electric field on the surface of the narrower electrode should be equal to the minimal electric field on the microstructure surface between the electrodes. This results in electrode widths of $w_1 = 0.166\,\mathrm{mm}$ and $w_2 = 0.349\,\mathrm{mm}$ and an electric field strength at the surface of the microstructure as shown by the solid line in Fig. 3.13. The electric field strength $E_{\mu,\mathrm{min}}$ at the center of the wider electrode is just slightly more than the trap depth. This is in fact the weakest electric field strength on the surface of the entire microstructure. The fact that it is just slightly more than the trap depth is a matter of definition because the value of $3\,V_\mu$ for the voltage applied to the perimeter electrode is based on this electric field strength. In principle, a slightly higher voltage could be applied to the perimeter electrode such that the trap depth is equal to $E_{\mu,\mathrm{min}}$. The value of $3\,V_\mu$ was chosen both for simplicity and to allow for slight variations in the actual microstructure fields compared to the theoretical fields shown in Fig. 3.13.

In the absence of any offset fields perpendicular to the microstructure plates, the electrode widths at the other end of the microstructure taper would best be the same as the widths at the first end, but with the values for the positive and negative electrode being interchanged. However, offset fields affect the electric field strength on the opposite polarity electrodes differently, and an asymmetric taper design can be used to allow for large offset fields without reducing the trap depth. This is particularly relevant since the original proposal for optoelectrical cooling requires a large offset field to be applied between the capacitor plates in one half of the trap. As a result, the electrode widths at the second end of the taper were chosen such that an offset field of approximately $E_{\mu,\mathrm{min}}/2$ can be applied without reducing the electric field strength at the surface of the microstructure below $E_{\mu,\mathrm{min}}$. This is translated to the conditions that the minimum electric field strength on the electrode of width w_1 is 50% more than $E_{\mu,\mathrm{min}}$ and that the minimum electric field strength on the electrode of width w_2 is 50% of $E_{\mu,\mathrm{min}}$ less than the minimal electric field strength on the surface of the electrode of width w_1 at the first end of the taper. These conditions result in electrode widths of $w_1 = 0.220\,\mathrm{mm}$ and $w_2 = 0.177\,\mathrm{mm}$ and an electric field strength at the surface of the microstructure shown by the dashed line in Fig. 3.13. The mean electric potential on the microstructure surface resulting from these widths is $0.0653V_\mu$, and the electric field strength along the microstructure will thus be $0.3153V_\mu$ divided by the distance over which the taper occurs.

In order to use the asymmetric microstructure taper to allow for large offset fields without reducing the trap depth, the polarity of the offset field needs to be such that it increases the electric field strength on the electrode of width w_2 and reduced the field strength on the electrode of width w_1. As a result, to allow for a large offset field between the capacitor plates, the polarity of the electrodes of width w_1 and w_2 would need to be exchanged between the two capacitor plates of the trap. Choosing an opposite preferred sign for the offset field for the two capacitor plates in this way is problematic because the perimeter electrode also produces large offset fields perpendicular to the capacitor plate surface with an equal sign for both plates. In particular, the microstructure taper needs to extend quite close to the sides of the trap, resulting in offset fields due to the perimeter electrodes which are as large as 25% of the trap depth (see section 3.6.7 for details). Since the offset field due to the perimeter electrode needs to be on permanently whereas

a large offset field between the capacitor plates is optional for basic operation of the trap, it was decided to have the electrode of width w_1 be of the same polarity as the perimeter electrode for both capacitor plates of the trap. Note that since the perimeter electrode only creates an offset field of 25% of the trap depth in the region where the microstructure taper exists, the asymmetry in the microstructure taper is larger than it needs to be, and would optimally be reduced.

3.6.4.2 Maintaining homogeneous fields with a tapered microstructure

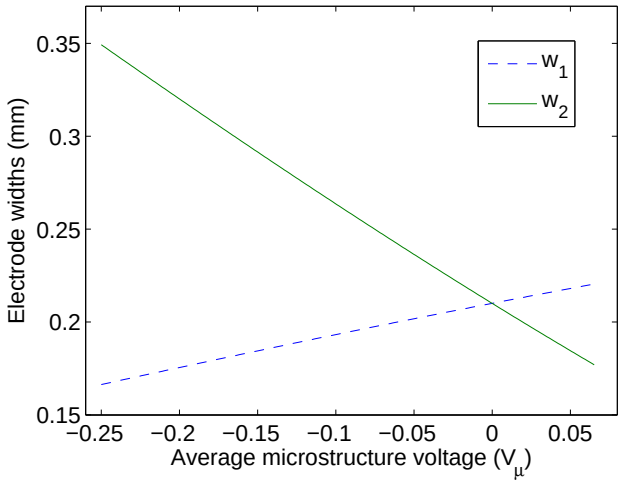

Figure 3.14: Electrode widths for the microstructure versus average voltage (in units of the voltage $\pm V_\mu$ applied to the microstructure electrodes) on the microstructure surface which the indicated electrode widths produce. Replacing the voltage on the horizontal axis by position along the microstructure results in the required progression of the electrode widths along the microstructure taper to achieve a homogeneous field along the microstructure.

So far we have only considered the electrode widths at either end of the microstructure but not the progression of the widths in between. This is because in terms of the criteria we have discussed so far: achieving a sufficient electric field along the microstructure, maintaining the trap depth, and limiting the maximal fields, the progression is quite uncritical, and a linear interpolation between the values at the end of the taper is completely sufficient. The progression of the electrode widths nonetheless plays a key role for the trap in that the field along the electrodes, unlike all other electric fields in the trap except for the offset field between the capacitor plates, extends with undiminished strength to the center of the trap. Unlike the offset field between the capacitor plates, however, the field along the microstructure electrodes is by no means automatically homogeneous, and failure to ensure that it is homogeneous would wipe out a large part of the effort to build a trap with homogeneous fields in the center!

Determining the required electrode width progression to achieve homogeneous fields is (with the help of the theory from section 3.6.1) quite easy. All we need to do is ensure that the average voltage on the microstructure surface (which is the effective voltage of the microstructure plate as viewed from a distance) progresses linearly with distance along the microstructure taper. This is achieved in detail as follows. We linearly interpolate the electrode widths between the values $w_{1,i}$ and $w_{2,i}$ at one end and $w_{1,ii}$ and $w_{2,ii}$ at the other end of the taper as defined above as a function of a parameter t according to

$$\begin{aligned} w_1(t) &= w_{1,i} + (w_{1,ii} - w_{1,i})t \\ w_2(t) &= w_{2,i} + (w_{2,ii} - w_{2,i})t \end{aligned} \qquad 0 \leq t \leq 1. \tag{3.62}$$

The theory in section 3.6.1 provides the average voltage on the microstructure surface $V(w_1, w_2)$ as a function of the electrode widths. Inserting Eq. 3.62 into this function, we obtain a function $V(t)$. This function is inverted and inserted into Eq. 3.62 to obtain functions $w_1(V)$ and $w_2(V)$ which are plotted in Fig. 3.14. Replacing V by a linear function of the position along the microstructure taper, we obtain the desired progression of the electrode widths.

3.6.5 Eliminating holes between the perimeter electrode and the microstructure

The lines of near zero electric field above every second microstructure electrode discussed above by no means end near the perimeter electrode. All that happens is that they move closer to the surface as the offset field E_0 perpendicular to the microstructure increases. For microstructure electrodes contacted sufficiently close to the edge of the perimeter electrode, the perimeter electrode will produce sufficiently strong electric fields along these channels of near zero field to prevent Majorana losses in this region. However, the channels nonetheless cause a problem in that they lead directly out of the trap volume and thus constitute holes through which molecules can escape from the trap.

In principle the channels of near zero electric field under the perimeter electrode can be plugged by applying an electric potential gradient along the channel with a strength equal to the trap depth. For microstructure electrodes contacted as shown in Fig. 3.10, corresponding to Fig. 3.15a, this is basically automatically the case on the side of the microstructure where the microstructure electrodes with the opposite polarity as the perimeter electrode (i.e. those above which a low field channel does not exist) are contacted. Here, a high electric field strength exists everywhere on the microstructure surface, either due to the offset field from the perimeter electrode, or due to the electric potential difference between the microstructure electrodes of opposite polarity.

On the side of the microstructure where the microstructure electrodes with the same polarity as the perimeter electrode are contacted, avoiding holes in the trap is much more difficult. The surface normal electric field on these electrodes invariably changes sign between what is the top and the bottom of Fig. 3.15a. This results in a region of zero electric field on the electrode surface, indicated by the red line in the figure, and the

Figure 3.15: Variations for contacting the microstructure electrodes underneath the perimeter electrode. **a**. This simplest variation works fine on the side of the microstructure where the black electrode has the opposite polarity as the perimeter electrode. However, when the black electrode has the same polarity as the perimeter electrode, a zero-field region indicated by the red line exists on the surface of the electrode, resulting in holes in the electric trap. **b**. The region of zero electric field on the microstructure surface can be eliminated by adding an additional electrode with the opposite polarity as the perimeter electrode above the electrode with the same polarity as the perimeter electrode. However, the electric field strength is still substantially weakened in the vicinity of the red crosses, and the holes in the trap thus effectively remain. **c**. The holes in the trap can be almost completely eliminated by bending the microstructure electrodes with the same polarity as the perimeter electrode around and contacting them in a single location at the side of the trap.

low-field channels thus end in an entire line of zero field on the microstructure electrode surface. While the zero field can be eliminated by adding an additional electrode as shown in Fig. 3.15b, the low field channels will still terminate in a point of weak field on the microstructure surface in the vicinity of the red crosses in the figure.

We estimate the loss rate for molecules through the low-field channels under the perimeter electrode. Whereas the absolute loss rate depends on a variety of parameters according to the description in section 3.2.2, almost all these parameters cancel when comparing with the loss rate through the entrance and exit quadrupole guide connected to the trap, and we thus calculate the ratio of these loss rates. In fact, modeling both holes as a two-dimensional electric quadrupoles, the only relevant parameter is the rate of increase of the electric field strength with distance from the center of the quadrupole hole. For the capacitor-plate-based guide shown in Fig. 3.7, this is 0.93 TDU/mm. For the holes under the perimeter electrode, and approximating the electric field with Eq. 3.60, this is approximately $2\pi E_0/d = 7.9\,\mathrm{TDU/mm}$, where $E_0 = 1\,\mathrm{TDU}$ and d is the periodicity of the microstructure. Due to the approximate nature of Eq. 3.60, this second value is approximately 10% too small.

Since the loss rate through a quadrupole hole in the trap is inversely proportional to the square of the increase of the electric field strength with distance from the center of the hole, the loss rate through a single hole under the perimeter electrode is approximately 72 times less than the loss rate through either the input or the output guide of the trap. However, for microstructure electrodes contacted as shown in Fig. 3.15a or b, one hole

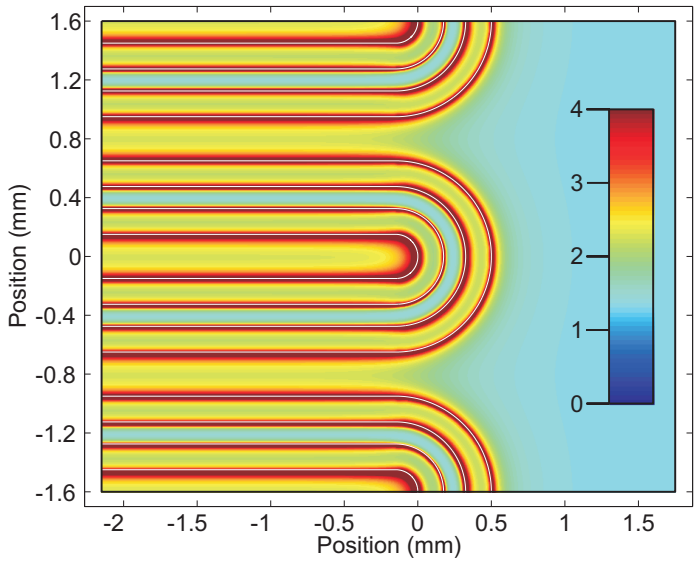

Figure 3.16: Electric field strength at the surface of the microstructure for microstructure electrodes contacted as shown in Fig. 3.15c. The edges of the electrodes are indicated by the white lines. The ends of the electrodes are defined by a sequence of concentric circles. The electric field strength on the right side of the figure is 1/3 larger than the nominal trap depth because, for a voltage of $\pm V_\mu$ applied to the microstructure and a voltage of $3V_\mu$ applied to the perimeter electrode, the voltage difference to the perimeter electrode in this region is 1/3 larger than the voltage difference between the perimeter electrode and the average microstructure voltage. This is not the case for the actual microstructure because the microstructure electrode with opposite polarity as the perimeter electrode is followed by an electrode which typically has a voltage applied which is equal to the average microstructure voltage, in a geometry analogous to that in Fig. 3.15b.

exists for each of the 100 microstructure electrodes with the same polarity as the perimeter electrode on the two capacitor plates of the trap. Moreover, the holes consisting of the input and output quadrupole can be plugged by applying appropriate voltages between two consecutive segments of the input and output guide, which is hardly possible with the holes under the perimeter electrode. For an optimized trap where the dominant loss process would otherwise be molecules escaping through input and output guide, the holes under the perimeter electrode thus substantially reduce the number of molecules which can be loaded into and unloaded from the trap.

By tweaking the design in Fig. 3.15b, for example by reducing the width of the black electrode across the top of the figure, the electric field strength at the surface of the black electrode could probably be increased to the point where only the hottest molecules in the trap can still reach the electrode surface. However, this invariably increases the maximum electric fields near the edges of the microstructure electrodes as well. A much more satisfactory approach exists by contacting the microstructure electrodes as shown in Fig. 3.15c. Here, the microstructure electrode with the same polarity as the perimeter

electrode meanders back and forth across the surface of the capacitor plates and is only contacted in a single location at the side of the trap. For the present trap design with two independent trap regions on both capacitor plates, this reduced the number of holes under the perimeter electrode to one for each of the four independently contacted microstructure electrodes with the same polarity as the perimeter electrode. The losses will thus be negligible compared to the loss rate through the entrance and exit guide of the trap.

To ensure that no weak spots in the trapping fields under the perimeter electrode remain, we have calculated the electric field strength at the microstructure surface for electrodes contacted as shown in Fig. 3.15c. The result is shown in Fig. 3.16. Clearly, the electric field strength is everywhere larger than the trap depth, and the holes in the trapping field are thus eliminated. Note the particularly large fields at the end of the electrodes at multiples of 1.6 mm in the figure. These are most probably the regions of highest electric field on the entire microstructure surface. It would thus be worthwhile trying to reduce these fields, for example by moving the ends of the electrodes at multiples of 1.6 mm slightly to the left.

3.6.6 Interface between the two halves of the trap

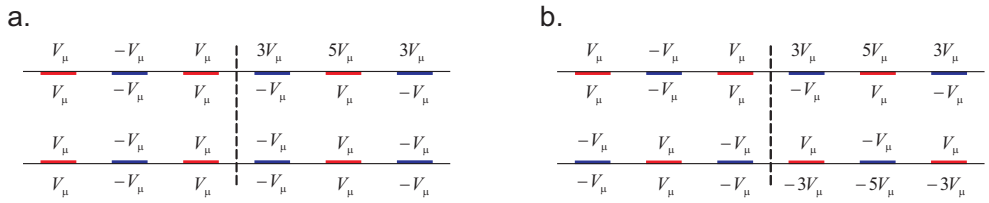

Figure 3.17: Realization of the interface between the two halves of the trap with independent microstructure voltages. All electrodes of a given polarity on either plate on either the right or the left side of the dashed line are interconnected. Two distinct configurations exist regarding the polarity of the last electrode on a given side of the trap, shown in **a** and in **b**. Configuration **b** allows a much higher offset field between the capacitor plates on one side of the trap for zero offset on the other side subject to the constraint that the voltage difference between neighboring electrodes never exceeds $2V_\mu$. Typical voltages applied are shown in the center, voltages to achieve a maximal offset field on the right are shown on the outside of the electrodes.

One final element of the trap microstructure design is worth mentioning before adding all the design elements together. As mentioned in section 3.3.2, the length of the trap is chosen to be equal to twice the width with the intent of applying independent voltages to the capacitor plates in two halves of the trap. This is easily achieved by contacting the set of microstructure electrodes on either half of the trap independently. However, this leads to two distinct variations as shown in Fig. 3.17. As explained in the figure, variation b has the advantage of allowing a much larger difference in offset voltage between the capacitor plates on the two sides of the trap. For the example in the figure, this is equal to $8V_\mu$,

allowing an offset field of 0.8 TDU on one side of the trap for an offset field of 0 TDU on the other side. However, applying these voltages severely distorts the trap confinement near the perimeter electrode. We note that for a microstructure with a smaller periodicity, the microstructure voltages will be proportionally reduced, and this equally reduces the maximal difference in offset field between the two halves of trap. To avoid this problem, it might be necessary to add additional independently contacted electrodes between the two sides of the capacitor plates.

3.6.7 Overall design of the trap microstructure

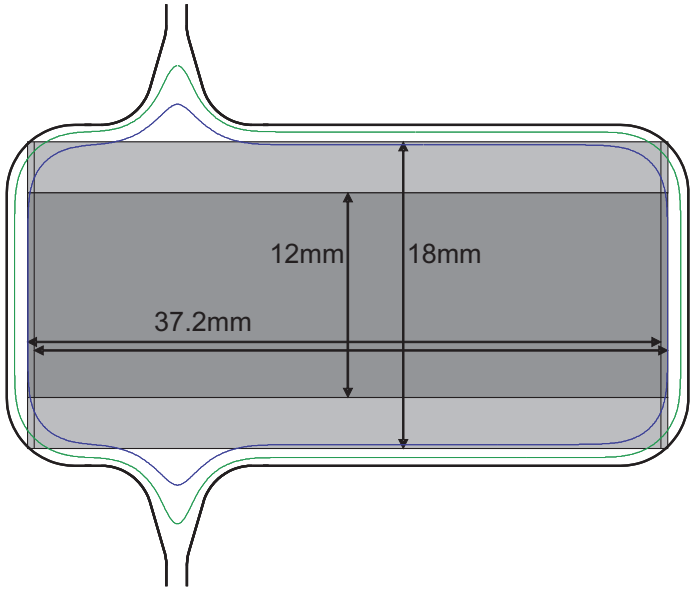

Figure 3.18: Subdivision of the microstructure surface, as explained in the text. The outer black line shows the position of the inner edge of the perimeter electrode. The green line is the set of points where the offset field due to the perimeter electrode on the capacitor plate surface is half the trap depth, the blue line is the set of points where the offset field is a quarter of the trap depth.

We are now finally ready to consider the microstructure plates as a whole. The surface of the microstructure plates can be subdivided into a number of different regions, depending in particular on which microstructure design elements described above need to be applied. This subdivision is shown in Fig. 3.18. The inner dark gray region is the central trap region, where the widths of the microstructure electrodes are determined by the microstructure taper described in section 3.6.4. The final tapered electrode on all four sides of the two capacitor plates has the opposite polarity as the perimeter electrode. Since the position of the positive and negative microstructure electrodes on the two plates are interchanged according to Fig. 3.17b, this causes the position of the central trap region to be shifted by 0.4 mm between the two capacitor plates. The central trap region ends 1.2 mm from the

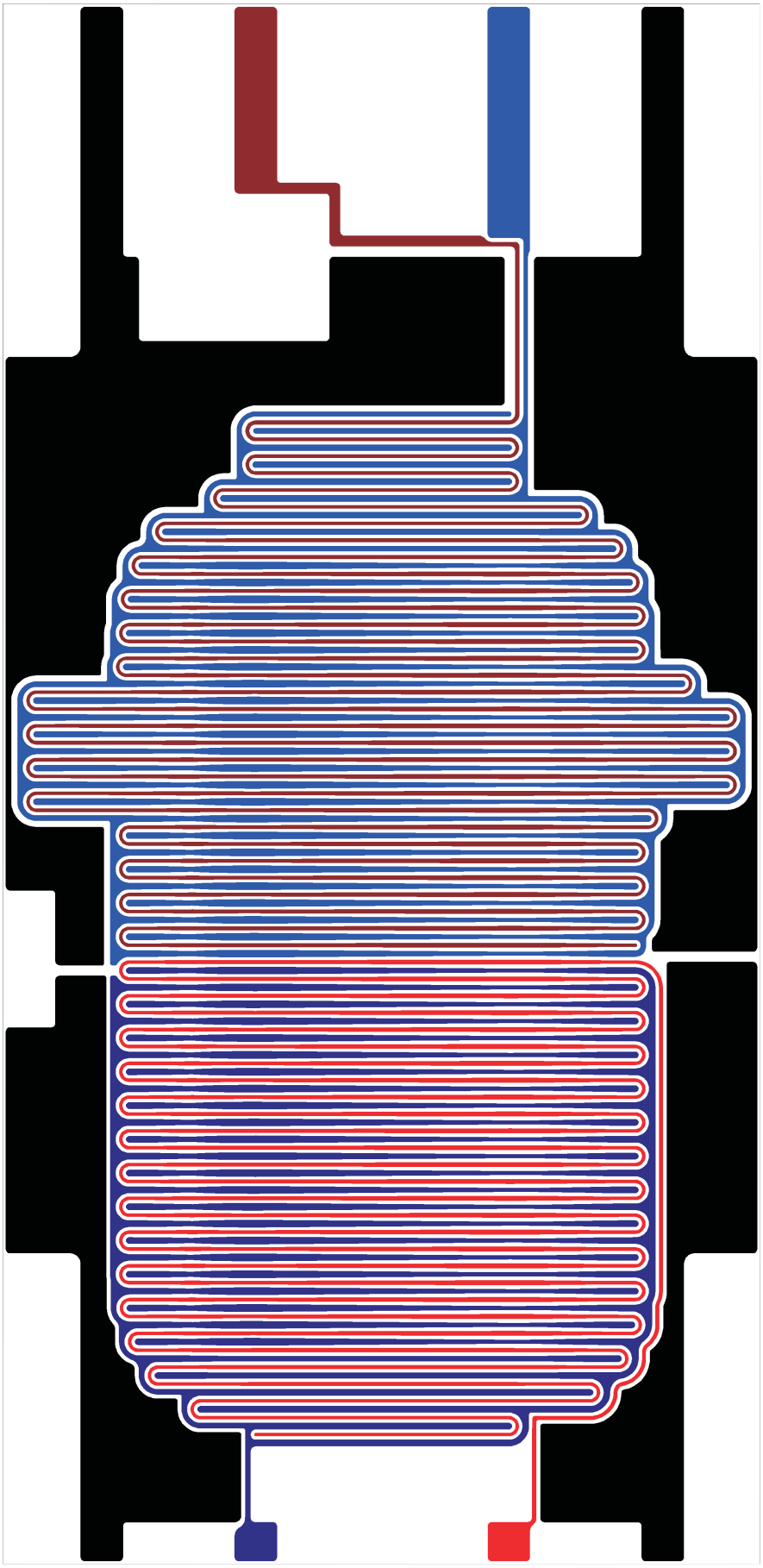

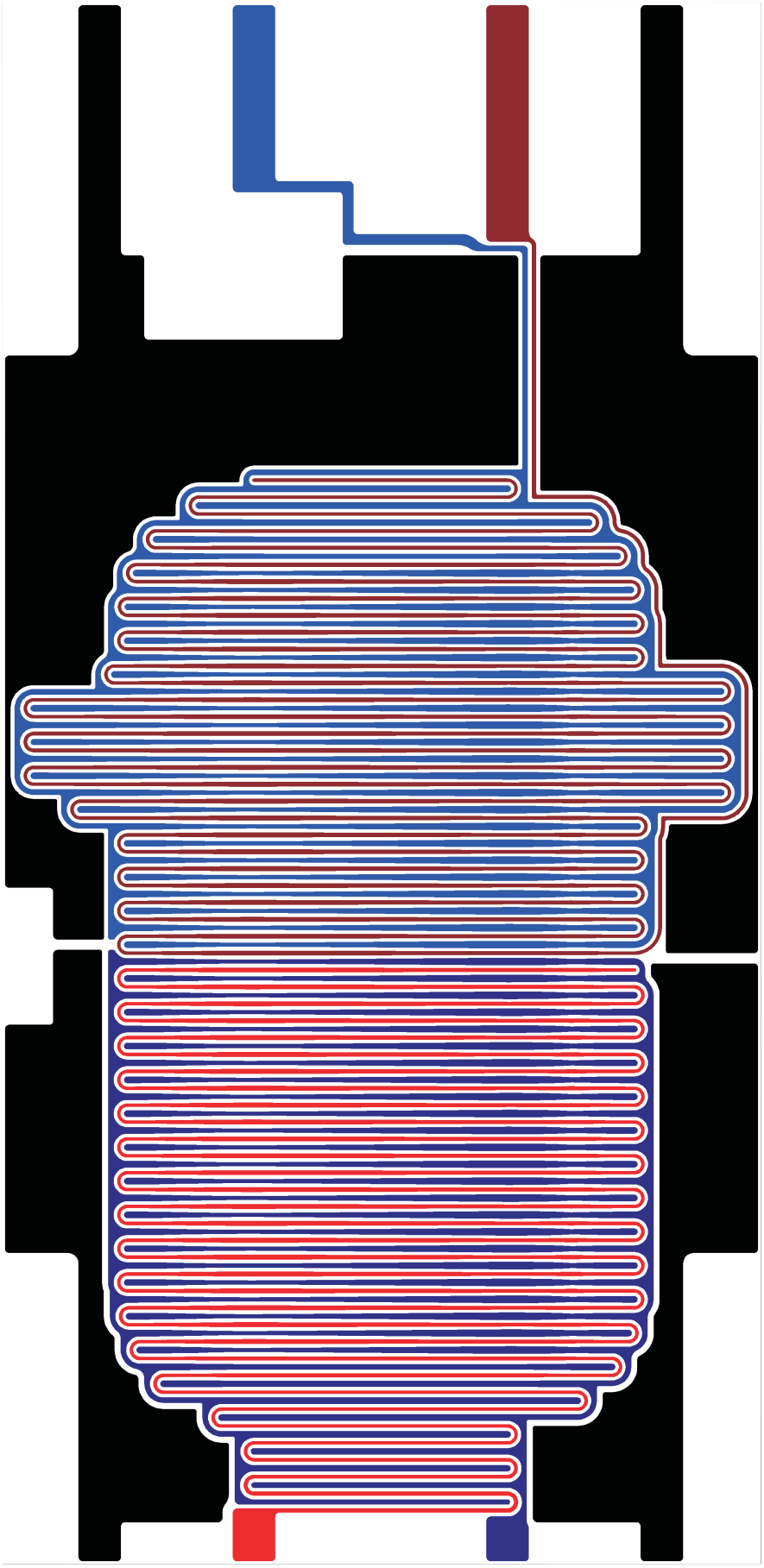

Figure 3.19: (previous two pages) Drawing of the two complete microstructure plates, with overall dimensions of 36 mm×74 mm. The electrodes with the same polarity as the perimeter electrode are colored red, those with opposite polarity are colored blue. The black electrodes surrounding the microstructure electrodes are generally grounded.

front edge of the perimeter electrode on one side of the trap and 1.6 mm from the edge on the other side.

Ending the microstructure taper over a millimeter away from the front edge of the perimeter electrode on the sides of the trap was probably a big mistake. The electric field along the microstructure electrodes probably drops off extremely rapidly once the taper ends and is then no longer sufficient to prevent Majorana flips in the region of low field above every second microstructure electrode. The four first low-field regions on the four sides of the two capacitor plates alone are sufficient to limit the trap lifetime to approximately 2 s. However, these losses only occur for molecules which are hot enough to surmount the electric field barrier of approximately 25% of the trap depth on the way to the low field region due to the perimeter electrode. Strong evidence for this is seen in the experiment. It would thus be necessary to continue the microstructure taper further towards the side of the trap. This is substantially complicated by the need to take into account the strong offset field due to the perimeter electrode in this region when choosing the electrode widths along the taper.

In the outer white region of Fig. 3.18, the widths of the microstructure electrodes are determined by the strength of the offset field due to the perimeter electrode as described in section 3.6.3. Additionally, the electrodes are of course contacted in this region as described in section 3.6.5. The contacting starts 2 mm behind the front edge of the perimeter electrode. In the light gray region, the electrode widths are interpolated between the widths at the edge of the dark gray and the white region.

The microstructure electrodes are surrounded by a final set of electrodes which are typically grounded. This is motivated by the fear that the outer edges of the capacitor plate electrodes might be particular sensitive to being opposed by macroscopic electrodes with a different voltage applied. This is probably not an issue for the present microstructure with a relatively large periodicity where the microstructure voltages are almost as large as the perimeter electrode voltage, but it might be relevant for smaller microstructure periodicity. The ground electrode also ensures that the electric field strength between the capacitor plates and the perimeter electrode approaches a value equal to the nominal trap depth, as discussed in Fig. 3.16.

A drawing of the complete microstructure plates is shown in Fig. 3.19. The overall plate dimensions are 36 mm×74 mm. The microstructure plates are held in place by being pressed from the back against four supports in the corners of the plates. As a result, the corners of the plates are kept electrode free. To contact the microstructure electrodes, the original plan was to continue the electrodes to the back of the plates with silver paint and contact them there. However, this was completely incompatible with high voltages. As an alternative, miniature clamps were machined to attach to the edges of the plates. A much

better solution might be to drill feedthroughs through the plates and contact them from behind as originally planned. However, this requires tools which are currently unavailable.

3.6.8 Electric fields from the combined perimeter and microstructure electrodes

As a final part to the section on the trap microstructure, we consider the electric fields resulting from the combination of the microstructure electrodes and the perimeter electrode. This is particularly useful to determine the existence of remaining electric field zeros in the trap. Due to the large difference in scale between the microstructure and the overall trap, an accurate simulation of the fields in the electric trap as a whole has not been performed to date. However, a relatively good understanding of the overall trap fields can be obtained by making use of the near periodicity in the center of the trap in the direction along the capacitor plates perpendicular to the microstructure. As a result, the trap fields can be simulated by considering a volume of just 0.4 mm×3 mm×24 mm. The 24 mm dimension is along the microstructure and extends 2 mm past the front edge of the perimeter electrode in both directions. Due to the near translation symmetry along the trap microstructure, this dimension can be simulated with a substantially reduced resolution. The contacting of the microstructure electrodes is not simulated. The 3 mm direction is between the capacitor plates. The 0.4 mm dimension ends at the center of two neighboring microstructure electrodes. As a result, the sides of the simulation volume in this direction are reflection planes.

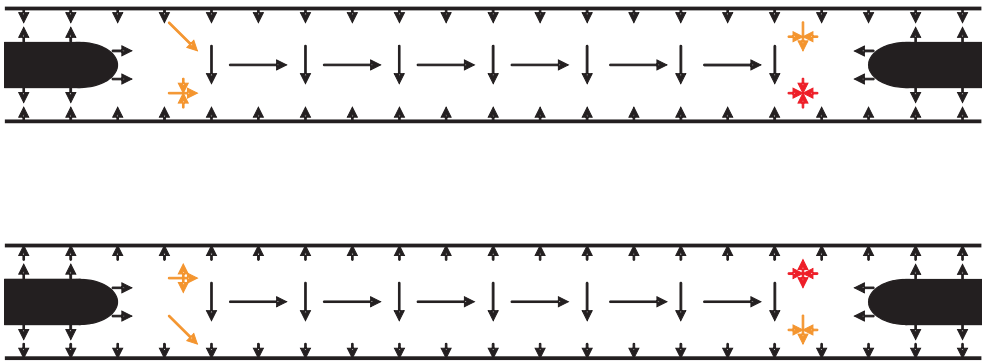

Figure 3.20: Direction field for the electric field in the central region of the trap. The images show a cut of the trap either centered above a microstructure electrode with the same polarity as the perimeter electrode (top) or a microstructure electrode with the opposite polarity as the perimeter electrode (bottom). Since both planes shown are approximate reflection planes near the center of the trap, the electric field component perpendicular to the planes is approximately zero. Between the planes, the electric field near the microstructure electrodes rotates from pointing away from the electrodes to pointing towards the electrodes, with the direction field otherwise remaining constant. We assume a positive voltage applied to the perimeter electrode. Further explanation is provided in the text.

To understand the electric field strength distributions obtained from the trap field simulation, it is instructive to construct an approximate direction field for the electric field vector in the trap, with the result shown in Fig. 3.20. The electric field is composed of two strong and two weak components. The strong components are the electric field pointing away from the perimeter electrode as well as the electric field pointing away from the positive polarity microstructure electrodes and towards the negative polarity microstructure electrodes. The weak components are the field between the capacitor plates due to an offset voltage between the plates and the field along the capacitor plates due to the microstructure taper.

Electric field zeros in the trap occur in locations where the various electric field components point in conflicting directions. Here, the critical areas are the corners of the diagrams in Fig. 3.20, indicated by the red and orange arrows. In three of the four corners denoted by the orange arrows, the electric field topology is such that the electric field switches direction along at most one dimension, but stays the same along the other dimension, allowing an electric field zero to be avoided. However, in the fourth corner denoted by the red arrows, the electric field switches direction along both dimensions. Since this is a topological feature of the electric fields, an electric field zero in the vicinity of the red arrows cannot be avoided without substantially changing the trap design. We note that in the plane shown, the electric potential near the electric field zero in the bottom diagram consists of a saddle point whereas in the top diagram, it consists of a local maximum. This is not a violation of Earnshaw's theorem since the electric potential also varies in the direction perpendicular to the plane.

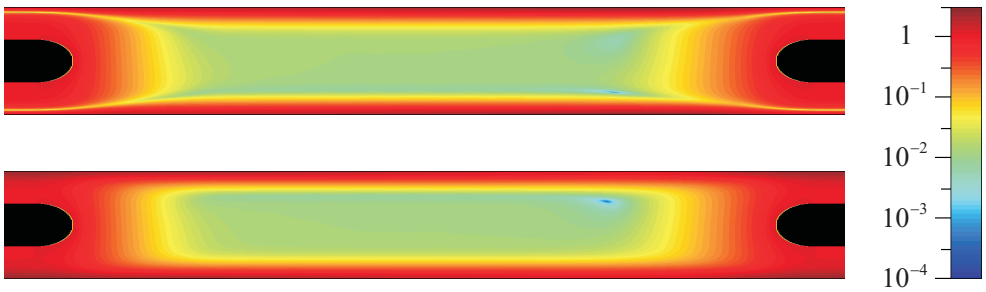

Figure 3.21: Electric field strength distribution in the same cuts of the trap as shown in Fig. 3.20. Here, voltages of $\pm V_\mu$ are applied to the microstructure electrodes, a voltage of $3V_\mu$ is applied to the perimeter electrode, and plate offset voltages of $+V_\mu/20$ and $-V_\mu/20$ are added to the microstructure voltages on the top and bottom capacitor plate, respectively.

The analysis of the electric field direction field is confirmed by the trap field simulation, with the electric field strength distribution for the same cuts of the trap as in Fig. 3.20 shown in Fig. 3.21. The only remaining electric field zeros are at the predicted locations. The field distribution also nicely shows the large region of homogeneous field in the center of the trap as well as the channels of low electric field above the electrode with the same polarity as the perimeter electrode under the perimeter electrode.

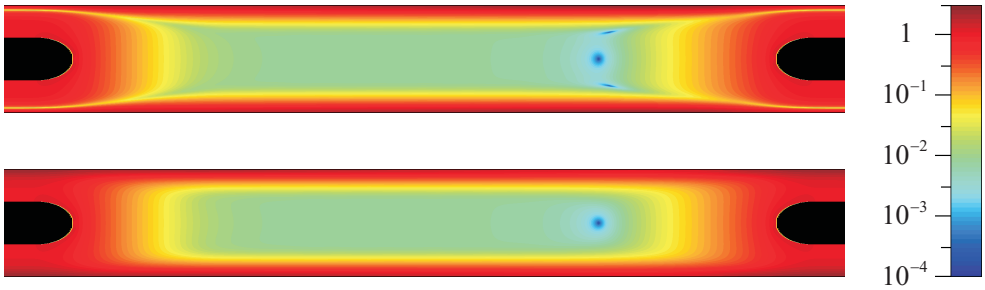

Figure 3.22: Electric field strength distribution for the trap as in Fig. 3.21 except that no offset voltage between the capacitor plates is applied. Here, a big electric field zero extends along the full length of one perimeter electrode at the center between the capacitor plates. The origin of this zero can easily be understood from Fig. 3.20.

A final instructive use of the trap field simulation is to consider the electric fields in the trap with the offset field between the capacitor plates set to zero. Naively, one might assume that an offset field between the plates is not necessary since the tapering of the microstructure already provides an offset field in the center of the trap as required to prevent Majorana losses. However, as shown by the field distributions in Fig. 3.22, for zero offset field between the plates the field along the microstructure and the field from the perimeter electrode will precisely cancel at some point in front of one perimeter electrode in the center between the capacitor plates. The resulting electric field zero extends along the full length of the perimeter electrode and is sufficient to reduce the trap lifetime to approximately 100 ms. Realizing the existence of this zero and adding the required high voltage supplies such that the voltages on the microstructure electrodes on the two capacitor plates could be set independently was the key step to establish an initial satisfactory operation of the trap.

3.7 Possibilities for improving the trap

The highly favorable properties of the trap based on the ideas developed in this chapter is illustrated by the substantial experimental achievements which have been realized with the trap [83, 82]. A number of ideas exist to improve the properties of the trap even further. Possibilities to improve the entrance and exit of the trap have already been explored in section 3.5.5. Here we discuss two additional ideas concerning a further increase in the trap lifetime and a further improvement of the homogeneity of the fields in the trap.

For molecules directly loaded into the electric trap, trap lifetimes on the order of 10 s have been observed [83]. Here, the scaling of the trap losses with the temperature of the molecules and the voltages applied to the trap electrodes strongly suggests that the losses are to a large part due to Majorana transitions. As discussed in section 3.6.8, a single electric field zero remains above every second microstructure electrode on both plates of the trap. Using the same molecule parameters as in section 3.6.4, a Stark splitting between

neighboring rotational sublevels of 200 MHz/(kV/cm) and a molecule velocity of 10 m/s, the simple estimate in section 3.2.4.2 predicts a Majorana loss rate for these zeros of $(20\,\mathrm{s})^{-1}$. However, the estimate in section 3.2.4.2 probably slightly underestimates the Majorana loss rate and uncertainties in the estimate easily account for the factor two difference to the measured trap loss rate. It is thus quite likely that the remaining electric field zeros above every second microstructure electrode are the main source of losses in the present trap.

The origin of the electric field zeros above every second microstructure electrode is basically as follows. In the center of the trap, the microstructure taper provides a field along the microstructure to plug the low-field channel above every second microstructure. Near the side of the trap, the perimeter electrode induced a much stronger field along the microstructure. On the side of the trap where the taper field and the perimeter field point in opposite directions, the field along the low-field channels must thus switch direction, and at these points electric field zeros occur. A possibility to increase the gradient of the electric field strength versus position at the electric field zeros and thereby reduce Majorana losses thus suggests itself as follows. Extending the microstructure taper closer to the perimeter electrode and even increasing the degree of taper near the electric field zeros would shift the zeros closer to the perimeter electrode. If the taper is then abruptly stopped or even reversed, the electric field along the low-field channels would switch directions much more quickly, as desired. In principle, a sufficient microstructure taper would shift the electric field zeros underneath the perimeter electrode, in which case they would essentially be eliminated entirely. However, considering that the maximum field along the low-field channel due to the perimeter electrode is approximately 10 times larger than the field along the low-field channel due to the microstructure taper, the fields which can be produced by the microstructure taper are clearly not strong enough for this to be possible.

A second point where a substantial improvement in the properties of the trap could be achieved is in the homogeneity of the fields in the trap center. As pointed out in the introduction, the current trap was designed with a focus on efficient trap loading and unloading and on reducing trap losses at the expense of the field homogeneity. Thus, the homogeneity of the trap fields could easily be improved by increasing the ratio of the transverse trap dimensions to the capacitor plate separation and the ratio of the capacitor plate separation to the microstructure periodicity. However, as noted in section 3.3.1, the former reduces the trap loading and unloading rate whereas the latter reduces the degree to which the microstructure can be tapered.

Making use of the experience with the present trap, it should be possible to reduce the microstructure periodicity while maintaining a sufficient microstructure taper to sufficiently suppress Majorana losses. This should allow the field inhomogeneity in the trap center due to the microstructure to be reduced to the point where it is negligible. Regarding the field inhomogeneity due to the perimeter electrode, increasing the ratio of the transverse trap dimensions to the capacitor plate separation would be unfortunate since the loading and unloading time of the present trap is already larger than optimal. However, a clever alternative exists based on modulating the microstructure width. In detail, this works as follows. Referring to Fig. 3.23, the width of the microstructure electrodes can be used

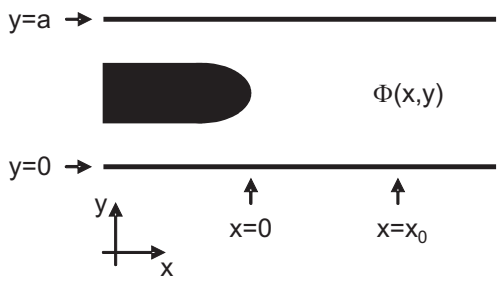

Figure 3.23: Sketch to help understand the compensation of the perimeter electrode field by varying the potential on the capacitor plate surface. The end of the perimeter electrode is located at $x = 0$, the capacitor plate surfaces are at $y = 0$ and at $y = a$. $\Phi(x, y)$ is the electric potential.

to effectively modulate the potential $\Phi(x, 0)$ and $\Phi(x, a)$ on the surface of the capacitor plates. If $\Phi(x, 0)$ and $\Phi(x, a)$ are constant for $x > x_0$ for some value of x_0, then the series expansion Eq. 3.15 can be used to express $\Phi(x, y)$ for $x > x_0$. The values of the coefficients in the series expansion depend both on the potential from the perimeter electrode as well as on the variation of the potential on the capacitor plate surface for $x < x_0$. The idea is then to use the variability in the potential on the capacitor plate surface to reduce the lead coefficients in the series expansion Eq. 3.15 to zero. The extremely rapid decay to zero of the remaining higher order terms in Eq. 3.15 would then ensure highly homogeneous fields for $x > x_0$.

A final point regarding the compensation of the perimeter field is that this may on first sight seem impossible since the perimeter electrode potential is much larger than the potential variation that can be achieved on the microstructure surface. However, since all potentials due to voltages applied on the left of Fig. 3.23 decay exponentially towards the right of Fig. 3.23, the potential from the perimeter electrode is substantially reduced at x_0 for a sufficiently large value of x_0. This allows relatively small voltages on the microstructure surface near x_0 to compensate the much larger perimeter electrode voltage.

Chapter 4

Experimental results

This chapter consists of the original previously unpublished version of the paper describing the first experimental results for optoelectrical Sisyphus cooling. After discussing the context of the results compared to other experiments, a brief description of the cooling scheme and the experimental setup is given. As noted in chapter 2, the cooling scheme slightly differs from the one originally proposed.

The main part of the paper discusses two data sets. The first data set consists of the unloading signal from the trap after cooling. The second data set consists of time of flight measurements from which velocity distributions for the molecules in the trap are derived. Comparison of the results with and without the radiation fields required for cooling applied provides irrefutable evidence for cooling.

The paper concludes with several appendices presenting further data and details of the experiment. In particular, the dependence of the trap unloading signal on both the unloading voltages and on the RF power during cooling is shown. These measurements also demonstrate that cooling takes place.

Publication: Sisyphus cooling of electrically trapped polyatomic molecules

M. Zeppenfeld, B.G.U. Englert, R. Glöckner, A. Prehn, M. Mielenz, C. Sommer, L.D. van Buuren, M. Motsch, and G. Rempe
substantially revised version published in Nature **491**, 570 (2012)

The rich internal structure and long-range dipole-dipole interactions establish polar molecules as unique instruments for quantum-controlled applications and fundamental investigations. Their potential fully unfolds at ultracold temperatures, where a plethora of effects is predicted in many-body physics [116, 87], quantum information science [30, 32], ultracold chemistry [11, 117], and physics beyond the standard model [41, 44]. These objectives have inspired the development of a wide range of methods to produce cold molecular ensembles [55, 64, 59, 100, 62, 118]. However, cooling polyatomic molecules to ultracold temperatures has until now seemed intractable. Here we report on the experimental realization of opto-electrical cooling [76], a paradigm-changing cooling and accumulation method for polar molecules. Its key attribute is the removal of a large fraction of a molecule's kinetic energy in each step of the cooling cycle via a Sisyphus effect, allowing cooling with only few dissipative decay processes. We demonstrate its potential by reducing the temperature of 10^6 CH_3F molecules by a factor of 5, with the phase-space density increased by a factor of 7, limited exclusively by our present setup. In contrast to other cooling mechanisms, our scheme proceeds in a trap, cools in all three dimensions, and works for a large variety of polar molecules. With no fundamental temperature limit anticipated down to the photon-recoil temperature in the nanokelvin range, our results eliminate the primary hurdle in producing ultracold polyatomic molecules. The low temperatures, large molecule numbers and long trapping times will allow an interaction-dominated regime to be attained, enabling collision studies and evaporative cooling to a molecular BEC. Our experiment thus opens up a route to quantum-gas physics with polyatomic molecules.

The ability to prepare ultracold molecular ensembles has an application potential akin to that of ultracold atoms some two decades ago. In fact, the association of KRb dimers [48] as well as the laser cooling of SrF [73] has brought fascinating physics within reach. However, both approaches are restricted to a highly specialized set of purely diatomic molecule species. In order to investigate fundamental physics based on relativistic effects near heavy nuclei or parity violation effects in chiral molecules, or to study molecules of astrophysical, biological, or chemical interest, a more general approach to preparing ultracold molecular ensemble is imperative. This holds in particular for the rich chemical variety of carbon-,

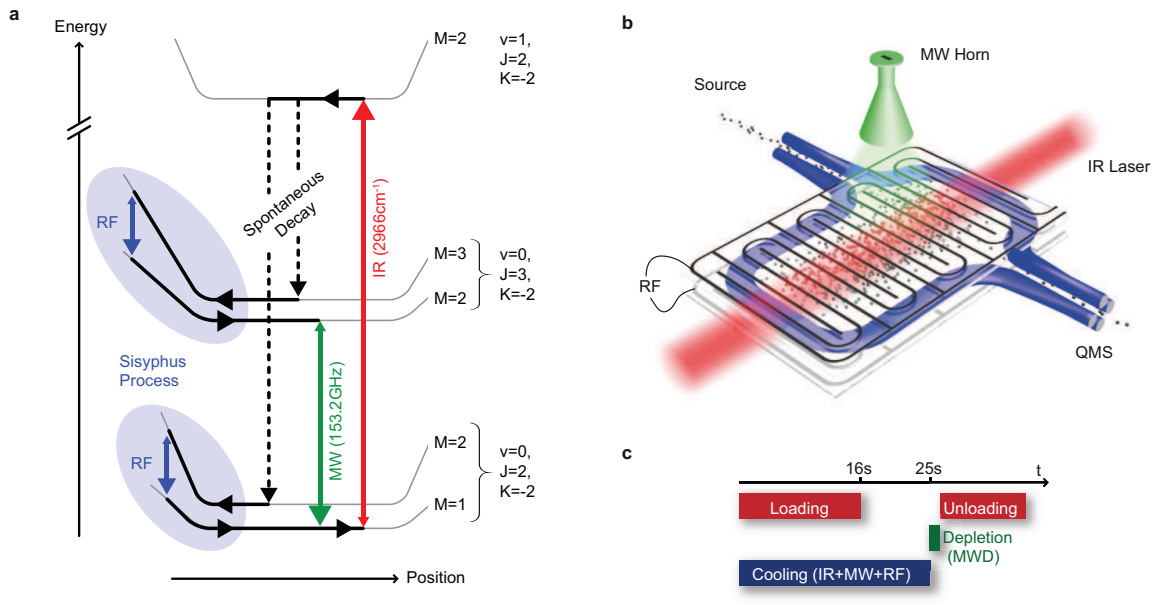

Figure 4.1: **Implementation of molecule cooling.** **a,** Radiation couples molecular states which experience a position-dependent potential energy in an electric trap as indicated. Molecules following the emphasized route lose more kinetic energy when entering the strong-field edge region of the trap than they regain when returning to the trap centre in a more weakly trapped state. Together with the unidirectionality of the optical pumping back to the strongly trapped states, this leads to cooling. **b,** During cooling the molecules are confined in a microstructured electric trap, with the IR, MW, and RF fields applied as indicated. **c,** Time sequence for loading and unloading of molecules, application of IR, MW, and RF fields for cooling, and realization of MW depletion for internal-state discrimination.

nitrogen-, or oxygen-based molecules for which the constituent atoms have not even been laser cooled. Devising a dissipative process to cool such molecules into the ultracold regime has been an exceedingly challenging problem. The standard approach for atoms, laser cooling, is impossible for the great majority of molecules due to the lack of suitable cycling transitions. Creating an artificial cycling transition via cavity cooling [70] has not been demonstrated despite substantial experimental [119] and theoretical [120, 121, 122] effort. Likewise, evaporative or sympathetic cooling to ultracold temperatures [123] is presently out of reach due to losses from inelastic collisions.

A particularly promising general framework to cool molecular ensembles is to replace the weak photon recoil in laser cooling with sufficiently strong forces to remove the entire molecule's kinetic energy in a single step [76, 80]. A first step towards this approach is the recent achievement of accumulation of NH molecules using a single-photon transition [79]. Here we present a full implementation of opto-electrical cooling [76], featuring accumulation and cooling. Energy is extracted by allowing molecules to move up and down an electric

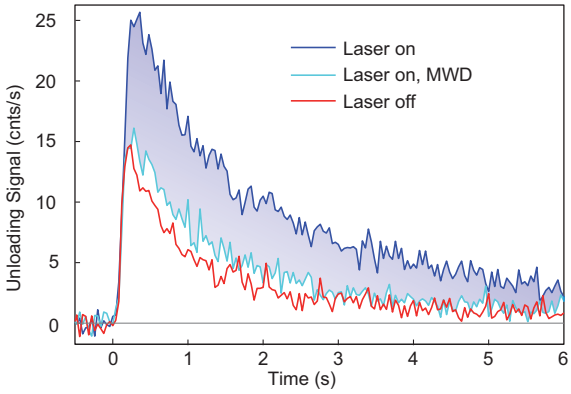

Figure 4.2: **Trap unloading signal.** We show the signal for the experimental cooling cycle (top) as well as for the same cycle but with either the IR laser left off (bottom) or the MW depletion (MWD) applied (middle). Cooling results in an increased signal and a slower decay. The laser-off signal (as well as the MWD signal) shows the background from molecules in uncooled rotational states. The shaded region represents the unloading signal in the states of interest (the state-discriminated unloading signal).

field gradient in different states with differing Stark energies while dissipation to remove entropy is provided by a spontaneous vibrational decay. The scheme is applicable to all molecules with strong electric-field interaction and pure ro-vibrational states, and thus constitutes a general method for cooling molecules to ultracold temperatures.

Reducing the temperature over several orders of magnitude requires the cooling cycle to be repeated many times, and consequently, control being maintained over the internal molecular state. This is achieved using the level scheme shown in Fig. 4.1a. An electric trap with a homogeneous electric field in the trap centre and strongly increasing fields near the trap boundary leads to a position-dependent potential energy for the relevant molecular states as shown. We label states with vibrational quantum number v and symmetric-top rotational quantum numbers J, K, M as $|v; J, -K, M\rangle$ [97]. For a parallel vibrational transition with $\Delta K = 0$, the state $|1; 2, 2, 2\rangle$ decays to the four rotational $v = 0$ states shown, with decay to the $|0; 3, 2, 1\rangle$ state ignored due to the small Clebsch-Gordan coefficient of $\frac{1}{63}$. Coupling the weakly trapped $|0; 2, 2, 1\rangle$ and $|0; 3, 2, 2\rangle$ states with microwave (MW) radiation and driving the $|0; 2, 2, 1\rangle$ to $|1; 2, 2, 2\rangle$ transition with an infrared (IR) laser results in optical pumping to the strongly trapped $|0; 2, 2, 2\rangle$ and $|0; 3, 2, 3\rangle$ states. Adding a radio-frequency (RF) to couple neighbouring M-sublevels in strong electric fields completes the opto-electrical cooling cycle. Losses to the untrapped $M = 0$ states are avoided by coupling the neighbouring M-sublevels with the RF at a slow rate compared to the optical pumping (see appendix A and C). Note that Stark detuning due to the electric fields plays a key role in selectively addressing only the desired IR and MW transitions (see appendix E).

During cooling, molecules are confined in a microstructured electric trap [83] depicted in Fig. 4.1b. The experimental cycle to prepare and detect a sample of cooled molecules

	RF	MW +IR	E_{unload} (kV/cm)	$\langle v_z \rangle$ (m/s)	T (mK)	N (cnts)	$N/\langle v_z \rangle^3$ (s^3/m^3)
No Cooling	-	-	40	8.1	268	44.9	0.085
Acc. 1	-	x	40	9.3	358	98.6	0.121
Acc. 2	-	x	10	6.6	176	34.5	0.122
Cooling	x	x	10	4.3	77	48.2	0.587

Table 4.1: **Experimental parameters and derived results** for the reference measurement, the two accumulation measurements and the cooling measurement. All variables are defined in the text. The values in the final column are proportional to the molecule phase-space density, showing an increase by a factor of 7.

is shown in Fig. 4.1c. After the cooling cycle, we apply a MW depletion (MWD) pulse to obtain an internal-state-discriminated signal with the quadrupole mass spectrometer (QMS). Details are provided in the methods section.

As a first result, Fig. 4.2 shows the raw averaged QMS trap unloading signal for three variations of the experimental cycle. Compared to leaving the laser off, the cooling sequence increases the integrated unloading signal by almost a factor of three. Considering that only an estimated 10 % of molecules enter the trap in the states $|0;2,2,M\rangle$ and $|0;3,2,M\rangle$ addressed by the laser, this clearly demonstrates a dissipative process which increases the molecular phase-space density. Moreover, the laser-off signal decays by half in about 1 s whereas the difference in signal with and without the MWD (the shaded region, corresponding to molecules in $J = 2$ and $J = 3$) decays by half in about 2 s. Considering that colder molecules have a longer trap lifetime [83], this is first evidence for cooling. Adding the MWD reduces the unloading signal almost back to the level with the IR laser off. In addition to illustrating the efficiency of the MWD in eliminating molecules in the states $J = 2$ and $J = 3$, this implies that almost all of the signal increase due to the laser is from molecules ending up in the rotational states $|0;2,2,2\rangle$ and $|0;3,2,3\rangle$. The tail of the trap unloading signal thus represents an almost state-selected source of polar molecules.

For a direct proof of cooling, we analyze the velocity distribution of molecules unloaded from the trap using time-of-flight measurements. We perform four variations of the experimental sequence with the varied experimental parameters shown in table 4.1. First, the experimental cycle is carried out with all IR, MW, and RF fields (except the MWD) left off as reference measurement without cooling. Here, the molecules experience purely conservative forces inside the trap. Adding the IR and MW fields results in accumulation of molecules. Molecules entering the trap in the weakly trapped states $|0;2,2,1\rangle$ and $|0;3,2,2\rangle$ are pumped to the strongly trapped $|0;2,2,2\rangle$ and $|0;3,2,3\rangle$ states. Finally, the RF is added to realize the complete cooling cycle. The unloading electric field strength, E_{unload}, is set for optimal unloading signal (see appendix C) for all except the second accumulation measurement. This 'accumulation 2' measurement is performed with the same voltages as for the cooling to account for filtering effects during unloading. A lower unloading potential eliminates hotter molecules and a higher potential inhibits colder molecules

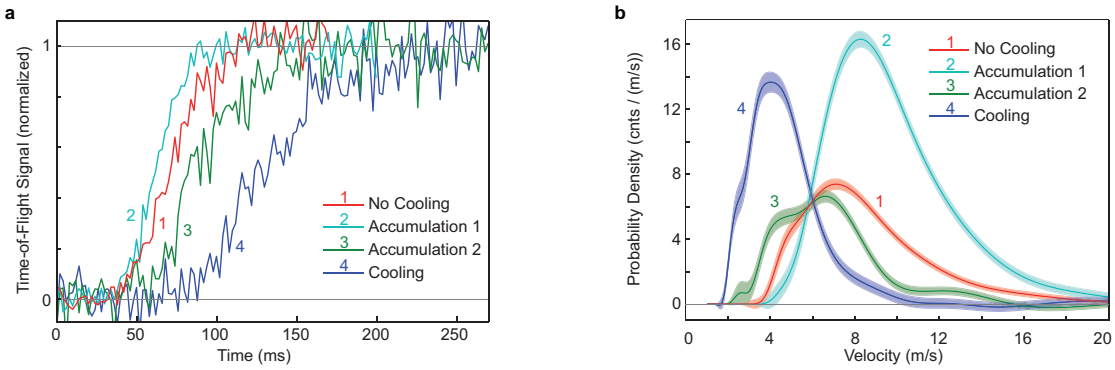

Figure 4.3: **Demonstration of opto-electrical cooling. a,** Rising edge of the normalized state-discriminated trap unloading signal for the four variations of the experimental sequence. **b,** Molecular velocity distributions derived from the rising-edge signals shown in (**a**) taking into account the number of detected molecules. Cooling results in a substantially increased signal below 6 m/s, clearly demonstrating that a dissipative cooling process has taken place. The shaded regions represent the 1σ statistical error.

from finding the exit hole.

The normalized rising-edge time-of-flight signals for the four measurements are shown in Fig. 4.3a and the derived velocity distributions, filtered via convolution with a Gaussian, are shown in Fig. 4.3b. As expected, the two measurements with $E_{\text{unload}} = 40\,\text{kV/cm}$ show the hottest molecules, with a peak velocity around 8 m/s. Adding the IR and MW radiation for accumulation results in over twice the molecule signal compared to 'no cooling'. Interestingly, the average velocity for the molecules for 'no cooling' is slightly lower. This most probably occurs since without accumulation molecules remain in the trap in the more weakly trapped states $|0;2,2,1\rangle$ and $|0;3,2,2\rangle$. Slow molecules in such states more easily find the trap exit than in more strongly trapped states. Reducing E_{unload} to 10 kV/cm for 'accumulation 2' results in strong velocity filtering of the trapped molecules. Below 5 m/s the signal even increases since these molecules are no longer restricted from leaving the trap unlike at higher unloading fields.

Adding the RF for the complete cooling cycle leads to the slowest velocity distribution with the peak velocity reduced to 4 m/s and with a clear signal increase compared to the low-E_{unload} accumulation measurement: the molecules have been cooled. Note that the only difference to the second accumulation measurement is the presence of the RF, which, without the optical pumping, causes strong trap losses.

For each time-of-flight measurement, we calculate the mean longitudinal velocity $\langle v_z \rangle$ and estimate the molecular temperature T via $\frac{1}{2}k_B T = \frac{1}{2}m\langle v_z \rangle^2$, with the results shown in table 4.1. Note that $\langle v_z \rangle$ is representative of the velocity in all three dimensions in the trap due to mixing of the velocity components [76, 83]. Compared to the first accumulation measurement, the cooling results in a reduction in temperature by a factor of 4.6. As a measure of the trap molecule density, we use the difference N in QMS counts with

and without the MWD during unloading per experimental cycle, extrapolated from the plateau value of the time-of-flight measurements. $N = 30$ corresponds to approximately 10^6 molecules in the trap. Compared to no cooling, the number of molecules for cooling even slightly increases. To estimate the increase in phase-space density, we multiply the number of detected molecules with the inverse of the mean velocity cubed, this quantity increasing by a total factor of 6.9. Interestingly, the two accumulation measurements show practically the same value, consistent with a uniform density in velocity-space below the trap cut-off energy.

Continuing the opto-electrical cooling to lower temperatures requires a number of limiting technical issues to be resolved. Most severely, residual inhomogeneities of the electric field in the trap, possibly due to surface charges, increasingly perturb the molecule motion for decreasing temperatures, preventing further cooling. Other issues are the low detector efficiency and the slow vibrational decay of CH_3F (see appendix F).

The present experimental results bring key applications of ultracold polar molecules within reach. First, the increased molecular phase-space density improves the sensitivity for high-resolution spectroscopy and collision experiments. Second, the lower temperature allows loading of molecules into more weakly confining microwave [124] or optical traps which can hold molecules in their rotational ground state, a prerequisite for achieving quantum degeneracy. Finally, our chip-like trap and guide architecture facilitates hybrid quantum systems for quantum information processing with cold molecules [32].

Methods Summary

The initial sample of molecules is generated by velocity filtering [100] from a liquid-nitrogen cooled source loaded into the electric trap [83] via a quadrupole guide. Molecules are continuously loaded into the trap for 16 s and stored for an additional 9 s. During the entire cooling cycle, the IR, MW, and RF fields for cooling are applied and the trap electric-field depth E_{trap} is set to 60 kV/cm. For cooling over a wide range in temperature several RF frequencies are used which are reduced over time. Detection is performed by guiding the molecules to the QMS via a second quadrupole guide.

For internal-state-discriminating measurement, a MWD pulse consisting of various MW frequencies near 153 GHz is applied during the last second before trap unloading every 2^{nd} cooling sequence. This mixes all M-sublevels of the $J = 2$ and $J = 3$ states, leaving only the unaffected background from molecules in other states in the trap. The unloading signal difference with and without the MWD constitutes the state-discriminated cooling signal for one experimental cycle.

The selection of CH_3F as molecule species is based on favourable properties for trap loading and detection. Large rotational constants and sufficient vapour pressure down to almost 100 K allow efficient velocity filtering with an adequate fraction ($\sim 10\,\%$) of molecules in the rotational states used for cooling. Low contributions from other molecules at the atomic mass 34 of CH_3F results in very low background for the QMS detection. For dissipation, the approximately 15 Hz spontaneous decay rate of the most suited parallel

vibrational v_1 symmetric C-H stretch mode is sufficient. A description of the IR and MW radiation sources required for CH_3F [125] is provided in appendix B.

Appendix A: Detailed Cooling Scheme

The illustration of the opto-electrical cooling cycle in Fig. 4.1a in the main text includes only the molecular states and transitions directly involved in the cooling scheme. Fig. 4.4 shows an expanded version of the cooling cycle where we consider all the decay channels from the $v = 1$ to the $v = 0$ states as well as transitions to lower M-sublevels driven by the RF fields. A careful consideration of the additional decay channels and RF transitions shows that their role in the cooling cycle can be marginalized.

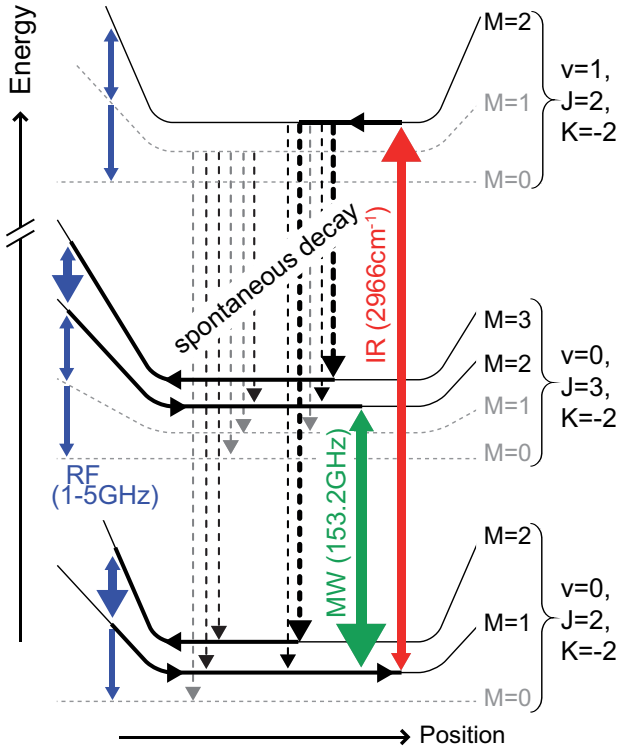

Figure 4.4: **Detailed energy-level diagram.** As described in the main text, molecules are cooled by following the emphasized route. Gray lines indicate various potential loss channels which are avoided as described in the text.

The selection rules $\Delta J = 0, \pm 1$, $\Delta K = 0$ and $\Delta M = 0, \pm 1$ for a parallel vibrational transition additionally result in spontaneous decay to the $|0; 2, 2, 1\rangle$, $|0; 3, 2, 2\rangle$, and $|0; 3, 2, 1\rangle$ states. Decay to the first two of these states does not constitute a loss channel since these states are already coupled to the excited state by the much stronger optical pumping. Although decay to the $|0; 3, 2, 1\rangle$ state leads to losses, the Clebsch-Gordan coefficient for this decay channel is only $\frac{1}{63}$ relative to the total decay rate. Due to the small

number of spontaneous decays required for cooling, this loss channel can be ignored in the present experiment. Therefore, only the spontaneous decay to the $|0;2,2,2\rangle$ and $|0;3,2,3\rangle$ states indicated in Fig. 4.1a in the main text is relevant to the cooling scheme.

The other major potential loss channel is the RF field which causes transitions to lower M-sublevels. These losses can be made arbitrarily small using a sufficiently low RF coupling rate, as discussed in the following. Suppose the transition rate from the strongly trapped states ($|0;2,2,2\rangle$ and $|0;3,2,3\rangle$) to the more weakly trapped states ($|0;2,2,1\rangle$ and $|0;3,2,2\rangle$) via the RF is γ_{RF} and the rate of optical pumping back to the strongly trapped states is γ_{IR}. For $\gamma_{\mathrm{RF}} \ll \gamma_{\mathrm{IR}}$, the fraction of molecules in the states $|1;2,2,2\rangle$, $|0;2,2,1\rangle$, and $|0;3,2,2\rangle$ is proportional to $\gamma_{\mathrm{RF}}/\gamma_{\mathrm{IR}}$ and the transition rate to the (potential) loss channels $|1;2,2,1\rangle$, $|0;2,2,0\rangle$, and $|0;3,2,1\rangle$ via the RF is proportional to $\gamma_{\mathrm{RF}} \times (\gamma_{\mathrm{RF}}/\gamma_{\mathrm{IR}})$. This compares to a cooling rate proportional to γ_{RF}. Therefore, by choosing a sufficiently weak RF intensity, the loss rate due to the RF can be made arbitrarily small compared to the cooling rate.

Appendix B: Details of the Experimental Setup

IR radiation at $2966\,\mathrm{cm}^{-1}$ to drive the $J = 2$, $\Delta J = 0$ transition of the v_1 vibrational band is produced by a CW optical parametric oscillator locked to a frequency comb. Line assignments and frequency values published in Ref. [125] are verified with saturation spectroscopy at sub-MHz resolution using a multi-pass Herriot cell and validated via combination differences between the $|v;J,K\rangle$ and $|v;J+1,K\rangle$ states. The 400 mW of IR power illuminates the trap from the side (as shown in Fig. 4.1b in the main text), driving the $|0;2,2,1\rangle$ to $|1;2,2,2\rangle$ transition with an estimated rate on the order of 100 Hz.

To couple the $v = 0$, $J = 2$ and $J = 3$ states, MW radiation at 153.2 GHz is generated by duodectupling (x12) the output of a frequency synthesizer. On the order of 3 mW MW power radiate from a MW horn antenna onto the front of the trap. During the cooling cycle the effective power is reduced by applying the MW with a 2% duty cycle, providing sufficient MW intensity to drive the narrowband $|0;2,2,1\rangle$ to $|0;3,2,2\rangle$ transition. For efficient MW depletion we require the full 100% duty cycle.

RF to couple neighbouring rotational M-sublevels is applied directly to the microstructure electrode contact leads. Naturally occurring electric resonances are exploited to inject sufficient RF power.

Appendix C: Optimization of Experimental Parameters

In this section we discuss the methods used to obtain the optimum experimental parameters for the unloading electric field strength and the intensity of the RF cooling fields.

Unloading Electric Field Strength

For detection, molecules are extracted from the trap via an electric quadrupole which guides the molecules to a quadrupole mass spectrometer (see Ref. [83] for details of the experimental setup). For a molecule with a fixed velocity, the probability of entering the guide increases with decreasing electric guiding field: higher field strengths produce a steeper guiding potential resulting in a narrower exit channel. Therefore, slower molecules are not efficiently extracted from the electric trap at high unloading fields whereas faster molecules are lost from the experiment at lower unloading fields due to weaker confinement. Consequently, a single set of unloading voltages is not suitable for unloading different molecule ensembles with different temperatures; instead, the unloading voltages must be adjusted to the temperature of the molecules.

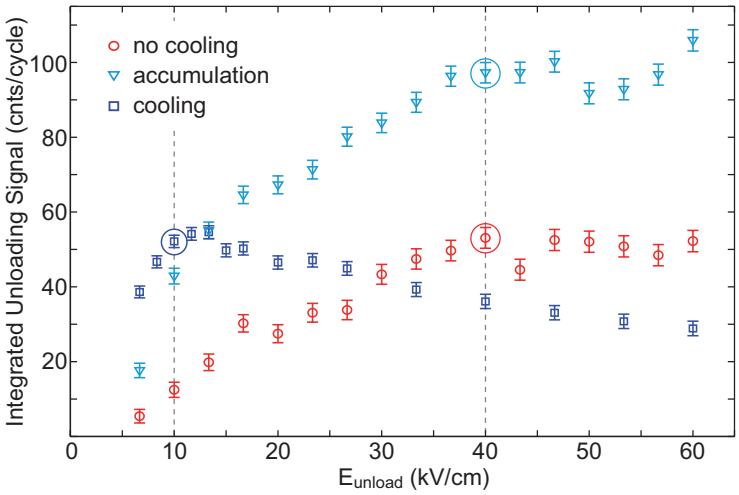

Figure 4.5: **Optimization of the unloading electric field strength.** The integrated unloading signal is measured as a function of the unloading electric field strength for no cooling (red circles), accumulation (cyan triangles), and cooling (blue squares). Circles indicate the optimum unloading electric fields which were chosen for the time-of-flight measurements, with the electric field value for "accumulation" and "no cooling" being the same.

Fig. 4.5 shows scans of the integrated unloading signal as a function of the unloading electric field strength for the three experimental settings as described in the main text: no cooling, accumulation, and cooling. Since accumulation only increases the density without reducing the velocity of the molecules, the shapes of "no cooling" and "accumulation" are very similar, indicating a similar velocity distribution with only an increased particle number in the case of "accumulation". The most significant difference occurs for "cooling" where a dramatic shift of the maximum is observed. For low unloading fields, the unloading signal in the case of "cooling" clearly exceeds "accumulation" due to the increased number of slow molecules. Vice versa, the absence of fast molecules in the case of "cooling" compared to "accumulation" results in a reduced signal at higher unloading fields. For an

optimal unloading signal for each experimental variation we chose an unloading electric field strength above which the signal does not significantly increase, i.e., 40 kV/cm for "no cooling" and "accumulation", and 10 kV/cm for "cooling".

RF Optimization

For efficient cooling, optimization of the power of the RF cooling fields (i.e., the RF fields driving the Sisyphus cooling transition) is required. On the one hand, if the RF power is too weak, the cooling cycle is not sufficiently fast and the molecules are not cooled. On the other hand, if the RF power is too high, trap losses occur due to pumping to untrapped $M = 0$ states. To determine the optimum RF power for cooling we have performed power scans for the different RF frequencies used in the cooling scheme. One representative power scan showing the characteristics of such a scan is shown in Fig. 4.6. Here, we vary the power of all RF frequencies simultaneously about the optimum value. To identify the cooled molecules we apply a strong 1 GHz RF field after the cooling cycle. This RF field serves as a temperature filter by eliminating molecules with sufficient energy to enter the high-field trapping regions with a Stark splitting of 1 GHz between neighbouring M-sublevels.

As expected, with all RF frequencies turned off no cooling occurs resulting in strong depletion by the 1 GHz filter and thus a low signal. For high relative RF powers we see losses caused by depletion due to the strong RF cooling fields. At the optimum point, the RF cooling fields are weak enough to not cause depletion but strong enough to efficiently cool the molecules such that they are not depleted by the 1 GHz filter.

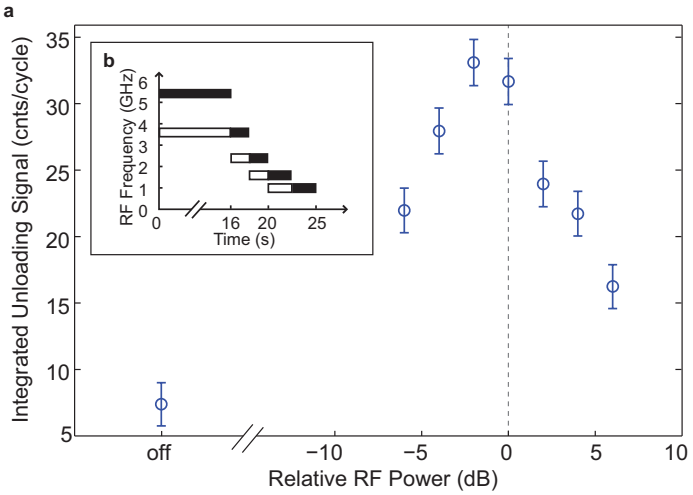

Figure 4.6: **Optimization of the RF power settings.** In this representative scan the RF power of all frequencies is changed simultaneously. The 0 dB point marks the optimum RF power used for the measurements presented in the main text. Unloading was carried out at $E_{\mathrm{unload}} = 10\,\mathrm{kV/cm}$. The inset shows the succession of RF frequencies applied to the trap during the cooling cycle. The filled bars indicate a higher RF intensity.

Appendix D: Signal Enhancement

Due to low detection efficiency, extracting a velocity distribution using a time-of-flight measurement requires an optimized data acquisition strategy to increase the signal per cycle. This is achieved by reducing the background from high rotational states and exploiting the full capacity of the unloading signal.

Elimination of High Rotational States

For the reduction of background from molecules in non-contributing uncooled rotational states we apply a weak 20 MHz RF field during the first 18 s of the cooling sequence. This radiation couples neighbouring rotational M-sublevels, thereby inducing trap losses by sequentially reducing the electric-field alignment of the molecules down to $M = 0$. The rotational states that participate in the cooling cycle remain practically unaffected, for two reasons. First, the power of the 20 MHz RF field is chosen such that the optical re-pumping to higher M states as part of the cooling cycle compensates the RF coupling. Second, for a symmetric rotor, the Stark splitting between neighbouring M-sublevels decreases with increasing J. The frequency of the RF field is chosen such that the coupling only occurs in trap regions with weak electric fields [83]. Therefore, the lower lying ($J = 2$ and 3) cooled rotational states are less affected by the 20 MHz RF field than higher rotational J states, due to the larger Stark splitting.

Improving the Data Acquisition Rate

Instead of using only the first rising edge of the unloading signal, the quadrupole guide to the QMS is repeatedly switched on and off during each trap unloading. This allows to record several time-of-flight profiles (rising edges) per experimental cycle which are summed up. In addition to improving the data acquisition rate, this results in a rising edge which represents an average over the velocity distribution of molecules leaving the trap at different times after the unloading process has started.

Appendix E: Choice of Transition Frequency

A key challenge in realizing the cooling scheme is to avoid transitions to states that are not involved in the cooling cycle. Separation of desired from undesired transitions is nontrivial due to the Stark broadening in the electric fields. Therefore, the IR and MW frequencies need to be carefully chosen such that only desired transitions are driven, independent of the position of the molecules in the trap. Note that the Stark broadening is on the order of a few 100 MHz, small compared to a trap depth of $\sim$30 GHz.

The M-sublevels of a given rovibrational $|v; J, -K\rangle$ state have very similar Stark shifts in both the $v = 0$ and the $v = 1$ state. In non-zero fields, all $\Delta M = -1$ transitions occur at a red-detuned frequency compared to the zero-field frequency, the $\Delta M = 0$ transitions

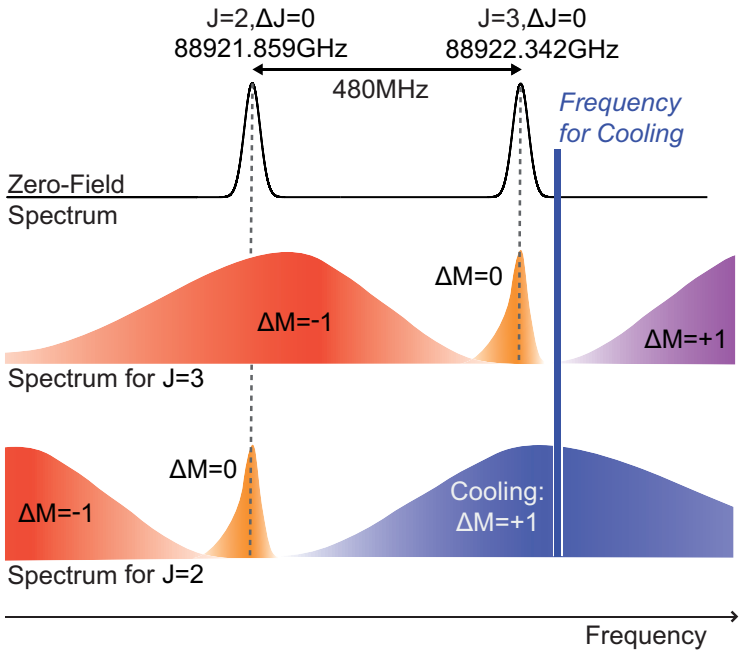

Figure 4.7: **Sketch of the IR spectrum in an inhomogeneous electric field.** The shaded areas indicate the approximate Stark-broadened transitions. The frequency of the IR laser is set such that it drives the required $\Delta M = +1$ cooling-transition between $J = 2$ states, but does not drive any transitions between $J = 3$ states.

occur near the zero-field frequency, and the $\Delta M = +1$ transitions are blue detuned (see Fig. 4.7). Avoiding the $\Delta M = -1$ and $\Delta M = 0$ transitions is achieved by blue detuning the IR field from the zero-field frequency.

However, since the transition used in the experiment ($|0;2,2\rangle$ to $|1;2,2\rangle$) lies within the Q-branch of the v_1 band, one also has to consider the $\Delta J = 0$ transitions between other rovibrational states. Specifically, the zero-field frequency of the $\Delta J = 0$ transition from the rovibrational $|0;3,2\rangle$ state is only 480 MHz blue detuned from the $|0;2,2\rangle$ to $|1;2,2\rangle$ transition, as shown in Fig. 4.7. Driving the $|0;3,2\rangle$ to $|1;3,2\rangle$ transition leads to losses via decay to the $J = 4$ state. As a solution, we blue detune the IR laser by 20 MHz from the $|0;3,2\rangle$ to $|1;3,2\rangle$ transition and set the offset field in the trap such that the $|0;2,2,1\rangle$ to $|1;2,2,2\rangle$ transition is Stark shifted by 500 MHz. This avoids unwanted $\Delta M = 0$ transitions since the differential Stark shift between the $|0;3,2,M\rangle$ and $|1;3,2,M\rangle$ states is sufficiently small and also inhibits undesired $\Delta M = 1$ transitions between the $J = 3$ states since the differential Stark shift between the $|0;3,2,M\rangle$ and $|1;3,2,M+1\rangle$ states in the offset field of the trap is sufficiently large.

Regarding the MW transition, the fact that the $|0;2,2,1\rangle$ and $|0;3,2,2\rangle$ states have the same first-order Stark shift offers an easy solution. All other transitions between states with $J = 2$ and $J = 3$ starting from states involved in the scheme have a non-zero first-order differential Stark shift. Therefore, by tuning the MW essentially to the zero-field

frequency of the $|0;2,2,1\rangle$ to $|0;3,2,2\rangle$ transition, only the desired transition is driven in the offset fields present almost everywhere in the trap.

Appendix F: Technical Limitations of the Current Setup

Continuing the opto-electrical cooling to lower temperatures requires a number of limiting technical issues to be resolved. Most severely, residual inhomogeneities of the electric field in the trap, possibly due to surface charges, increasingly perturb the molecule motion for decreasing temperatures. Evidence for such inhomogeneities comes from the observation of strong trap losses for microstructure fields below 20 kV/cm. Thus, for the $E_{\mathrm{unload}} = 10\,\mathrm{kV/cm}$ measurements, the microstructure electrode voltages are only reduced to the equivalent of 20 kV/cm and only the trap perimeter-electrode and guide voltages are ramped down further. Continuation of the cooling cycle to lower temperatures requires more homogeneous fields which can be achieved with improved microstructures. As a second issue, low detector count rates for the present measurements complicated further optimization of the cooling sequence due to poor statistics. This would be solved by improving the detection efficiency, e.g. with laser-based ionization of the molecules. Alternatively, using other molecules with faster decaying excited states or other sources of molecules would boost the signal. Finally, note that the strong Fermi resonance for CH_3F between the v_1 and $2v_5$ vibrational modes leads to additional losses during cooling due to decay to the first excitation of the v_5 mode. Based on the IR intensity of the v_5 band [126], this decay rate is around $1-2\,\mathrm{Hz}$, competing with the 15 Hz spontaneous decay rate to the vibrational ground state. This clearly is not a general problem for other molecule species.

Chapter 5

Outlook

In this thesis, we have described the realization of optoelectrical Sisyphus cooling, allowing us to substantially reduce the temperature of an ensemble of cold methyl fluoride molecules. Particular emphasis was placed on the design of a microstructured electric trap which was essential for the cooling to work. This trap can be continuously loaded from a quadrupole guide, provides a large trap depth, and allowed a record lifetime for trapped molecules to be achieved. Moreover, tunable homogeneous electric fields can be applied in a large fraction of the trap volume, allowing transitions between molecular rotational sublevels to be selectively addressed.

While the temperatures achieved so far – 77 mK for the results presented in chapter 4 and 29 mK for the results presented in ref. [82] – are still relatively high, optoelectrical cooling provide a clear perspective for reaching sub millikelvin temperatures. In ref. [82], reaching lower temperatures was mainly limited by relatively strong losses during cooling, resulting in decreasing signals such that optimizing the cooling process became increasingly difficult. Here, increasing the trap lifetime would allow more time for cooling, allowing losses to be reduced. A number of molecules have faster vibrational decay rates than methyl fluoride, allowing faster cooling.

A variety of possibilities to boost the molecule signal exist as well. Trap voltages could possibly be increased by a factor two, resulting in four times higher signal. The present detection efficiency for molecules is on the order of 10^{-4}, providing a big opportunity for improvement. As discussed in chapter 3, the present trap depth is possibly a factor four lower than it could be. Fixing this could increase the signal by as much as a factor of 256. Successfully implementing any one of these improvements should be sufficient to reach sub millikelvin temperatures.

A substantial increase in the number of trapped molecules can also be obtained by loading the microstructured trap from a higher-density source of molecules. For this purpose, a buffergas source of molecules has been set up in our lab [58, 118]. In addition to increasing the number of molecules, this should allow a wider variety of molecule species to be used.

The flux of molecules from a buffergas source can be substantially increased by operating it in the hydrodynamic regime [57]. However, this generates a molecular beam with a high

forward velocity. Loading such a beam into a trap requires the beam to be decelerated. Deceleration techniques demonstrated in the past discussed in chapter 1 are all pulsed, eliminating the advantage that our trap can be loaded continuously. This has motivate us to develop a new continuous deceleration technique for molecules which makes use of the centrifugal force on a rotating disk. Here, first results have been submitted for publication [66].

The tunable homogeneous fields in the microstructured trap promise exciting perspectives regarding manipulation and control of the internal molecular state. A first example is the state-discriminating measurement by driving microwave or infrared transitions to untrapped states discussed in chapter 4. The frequency dependence of losses induced by microwave or infrared radiation provides information about the electric field distribution in the trap. Due to the narrow field distribution, transitions between individual rotational sublevels can be addressed. This should allow the population in individual rotational sublevels to be determined. Moreover, optical pumping into a single rotational sublevel should be possible.

Optical pumping of molecules into a reduced number of internal states would constitutes internal state cooling. A template for such a scheme has been provided by the demonstration of internal state cooling of molecular ions [127, 128]. At first glance, transferring these results to neutral molecules might seem impossible. Thus, while optical pumping using a vibrational transition is used just as in our experiments, coupling between rotational levels relies on blackbody radiation. This results in an extremely slow cooling rate and would lead to transitions to untrapped states for electrically trapped polar molecules.

The homogeneous fields in our electric trap allow transitions between rotational sublevels to be driven individually rather than collectively as is the case for broadband blackbody radiation. Moreover, the transition rate can be orders of magnitudes faster than for blackbody radiation. By rapidly switching the microwave frequency, a large number of rotational states can be addressed simultaneously. Thus, in our present experiments, on the order of 10 transitions have been driven simultaneously, and it should be possible to drive hundreds of transitions simultaneously. This would allow the molecule population from hundreds of internal states to be pumped into a single state.

Internal state cooling could lead to a substantial increase in signal for our present experiments. Moreover, state-pure ensembles of heavier molecules might be generated despite a large number of internal states being thermally populated initially.

Danksagung

An dieser Stelle möchte ich mich bei allen bedanken, die zum Gelingen meiner Doktorarbeit beigetragen haben.

An erster Stelle möchte ich mich bei meiner Familie und insbesondere bei meinen Eltern bedanken. Zum erfolgreichen Werdegang eines Physikers gehört viel mehr als nur die Promotion.

Wissenschaftlich möchte ich mich an erster Stelle bei meinem Doktorvater Gerhard Rempe bedanken. Insbesondere dafür, dass er mir riesiges Vertrauen geschenkt hat, neue oft wilde Ideen und Ansätze zu verfolgen, wobei häufig lange Zeit nicht klar war, ob sie funktionieren würden. Hierbei hat er mich immer mit allen nötigen Mitteln unterstützt.

Als Nächstes möchte ich Pepijn Pinkse danken der meine Arbeit in den ersten Jahren meiner Promotion betreut hat und mich in die faszinierende Welt der kalten Moleküle eingeführt hat. Zusammen mit Gerhard Rempe hat er mir ein Problem für meine Promotion gestellt das es mir erlaubt hat sämtliche meiner Fähigkeiten als Physiker unter Beweis zu stellen. Er hat sich immer viel Zeit genommen, um über Theorie und Experiment zu diskutieren.

Barbara Englert möchte ich danken für die tatkräftige Zusammenarbeit am Experiment. Sie hat sich als erste Doktorandin überzeugen lassen an dem Projekt mitzuarbeiten, lange bevor klar war, dass es funktioniert. Nur durch ihren großen Einsatz hat sich das Experiment so schnell realisieren lassen.

Auch Michael Motsch möchte ich danken der lange Zeit mit mir zusammen gekämpft hat, um eine Methode zu finden, um Moleküle zu ultrakalten Temperaturen zu kühlen. Die kreative Atmosphäre, die durch den regen Austausch von Ideen entstanden ist, hat wesentlich zum Entstehen der Idee des optoelektrischen Kühlens beigetragen. Durch gemeinsame Diskussionen haben wir viele Details des Kühlprozesses ausgearbeitet.

Rosa Glöckner und Alexander Prehn möchte ich danken für ihren Beitrag am Experiment und für die gute Atmosphäre im Labor. Bei ihnen ist das Experiment in sehr guten Händen um weiterhin tolle Ergebnisse zu erzielen.

Bei meinem ehemaligen ersten Diplomanden Manuel Mielenz bedanke ich mich für seinen Beitrag beim Aufbauen der Falle. Auch für so manchen Spaß außerhalb der Arbeit möchte ich danken. Martin Ibrügger möchte ich danken für seinen Beitrag am Experiment im letzten Jahr.

Den anderen jetzigen und ehemaligen Mitarbeitern am Molekülexperiment, Sotir Chervenkov, Xing Wu, Christian Sommer, Laurens van Buuren, Thomas Gantner, Thomas Rieger, Sebastian Pohle, und Markus Schenk danke ich für die gemeinsame Begeisterung für kalte Moleküle. Des Weiteren danke ich für die gute Arbeitsatmosphäre, für die gemeinsame Freude an schönen Ergebnissen und das Lachen über anderes, wenn es gerade keine neuen Ergebnisse gibt.

Unseren Technikern Josef Bayerl, Franz Denk, Helmuth Stehbeck, und Thomas Wiesmeier danke ich für ihren unverzichtbaren Beitrag beim Aufbau des Experiments. Insbesondere Josef Bayerl möchte ich danken der so manch eine verrückte Idee durch seine technische Zeichnungen der Realität einen großen Schritt näher gebracht hat.

Stephan Ritter möchte ich danken für den ein oder anderen guten Ratschlag aus seiner Erfahrung als Wissenschaftler. Stephan Dürr danke ich für seine Bereitschaft Auskunft aus seinem großen Wissensschatz über Physik zu geben. Bei allen Mitgliedern der Arbeitsgruppe von Prof. Rempe bedanke ich mich für die gute Arbeitsatmosphäre und für verschiedene Hilfeleistungen Groß und Klein.

Meinem Bruder möchte ich danken für die vielen Jahre, die wir während meiner Promotion in bester Atmosphäre zusammengewohnt haben. Zuletzt möchte ich mich bei allen Leuten bedanken, die mit mir während meiner Promotion auf schönen Touren in den Bergen unterwegs waren, und insbesondere bei meinem Tourenpartner Axel Paulczinsky. Ohne die Erholung in den Bergen wäre aus meiner Doktorarbeit nie etwas geworden.

List of Publications

A Continuous Centrifuge Decelerator for Polar Molecules
S. Chervenkov, X. Wu, J. Bayerl, A. Rohlfes, T. Gantner, M. Zeppenfeld, and G. Rempe
Submitted for publication

Sisyphus cooling of electrically trapped polyatomic molecules
M. Zeppenfeld, B.G.U. Englert, R. Glöckner, A. Prehn, M. Mielenz, C. Sommer, L.D. van Buuren, M. Motsch, and G. Rempe
Nature **491**, 570 (2012)

Storage and Adiabatic Cooling of Polar Molecules in a Microstructured Trap
B. Englert, M. Mielenz, C. Sommer, J. Bayerl, M. Motsch, P.W.H. Pinkse, G. Rempe, and M. Zeppenfeld
Phys. Rev. Lett. **107**, 263003 (2011)

Velocity-selected molecular pulses produced by an electric guide
C. Sommer, M. Motsch, S. Chervenkov, L.D. van Buuren, M. Zeppenfeld, P.W.H. Pinkse, and G. Rempe
Phys. Rev. A **82**, 013410 (2010)

Cavity-Enhanced Rayleigh Scattering
M. Motsch, M. Zeppenfeld, P.W.H. Pinkse, and G. Rempe
New J. Phys. **12**, 063022 (2010)

Calculating the Fine Structure of a Fabry-Perot Resonator using Spheroidal Wave Functions
M. Zeppenfeld and P.W.H. Pinkse
Opt. Expr. **18**, 9580 (2010)

Opto-Electrical Cooling of Polar Molecules
M. Zeppenfeld, M. Motsch, P.W.H. Pinkse, and G. Rempe
Phys. Rev. A **80**, 041401(R) (2009)

Solutions to Maxwell's Equations using Spheroidal Coordinates
M. Zeppenfeld
New J. Phys. **11**, 073007 (2009)

Collisional effects in the formation of cold guided beams of polar molecules
M. Motsch, C. Sommer, M. Zeppenfeld, L.D. van Buuren, P.W.H. Pinkse, and G. Rempe
New J. Phys. **11**, 055030 (2009)

Cold guided beams of water isotopologs
M. Motsch, L.D. van Buuren, C. Sommer, M. Zeppenfeld, G. Rempe, and P.W.H. Pinkse
Phys. Rev. A **79**, 013405 (2009)

Spectroscopy of the $\tilde{A}^1A_2 \leftarrow \tilde{X}^1A_1$ transition of formaldehyde in the 30140-30790 cm^{-1} range: the $2_0^1 4_0^3$ and $2_0^2 4_0^1$ rovibrational bands
M. Motsch, M. Schenk, M. Zeppenfeld, M. Schmitt, W. Leo Meerts, P.W.H. Pinkse, and G. Rempe
J. Mol. Spec. **252**, 25-30 (2008)

Internal-state thermometry by depletion spectroscopy in a cold guided beam of formaldehyde
M. Motsch, M. Schenk, L.D. van Buuren, M. Zeppenfeld, P.W.H. Pinkse, and G. Rempe
Phys. Rev. A **76**, 061402(R) (2007)

Doppler-Free Spectroscopy of Weak Transitions: An Analytical Model Applied to Formaldehyde
M. Zeppenfeld, M. Motsch, P.W.H. Pinkse, and G. Rempe
Appl. Phys. B **89**, 475 (2007)

Bibliography

[1] A.E. Leanhardt, T.A. Pasquini, M. Saba, A. Schirotzek, Y. Shin, D. Kielpinski, D.E. Pritchard, and W. Ketterle. Cooling Bose-Einstein Condensates Below 500 Picokelvin. *Science*, 301:1513–1515, 2003.

[2] M.H. Anderson, J.R. Ensher, M.R. Matthews, C.E. Wieman, and E.A. Cornell. Observation of Bose-Einstein Condensation in a Dilute Atomic Vapor. *Science*, 269:198–201, 1995.

[3] F. Diedrich, J.C. Bergquist, W.M. Itano, and D.J. Wineland. Laser Cooling to the Zero-Point Energy of Motion. *Phys. Rev. Lett.*, 62:403–406, 1989.

[4] A.M. Kaufman, B.J. Lester, and C.A. Regal. Cooling a Single Atom in an Optical Tweezer to Its Quantum Ground State. *Phys. Rev. X*, 2:041014, 2012.

[5] A. Reiserer, C. Nölleke, S. Ritter, and G. Rempe. Ground-State Cooling of a Single Atom at the Center of an Optical Cavity. *Phys. Rev. Lett.*, 110:223003, 2013.

[6] M. Poot and H.S.J. van der Zant. Mechanical systems in the quantum regime. *Phys. Rep.*, 511:273–335, 2012.

[7] T.J. Kippenberg and K.J. Vahala. Cavity Opto-Mechanics. *Opt. Expr.*, 15:17172–17205, 2007.

[8] J. Chan, T.P.M. Alegre, A.H. Safavi-Naeini, J.T. Hill, A. Krause, S. Gröblacher M. Aspelmeyer, and O. Painter. Laser cooling of a nanomechanical oscillator into its quantum ground state. *Nature*, 478:89–92, 2011.

[9] I. Buluta, S. Ashhab, and F. Nori. Natural and artificial atoms for quantum computation. *Rep. Prog. Phys.*, 74:104401, 2011.

[10] M.D. Di Rosa. Laser-cooling molecules. *Eur. Phys. J. D*, 31:395–402, 2004.

[11] R.V. Krems. Cold controlled chemistry. *Phys. Chem. Chem. Phys.*, 10:4079–4092, 2008.

[12] M.T. Bell and T.P. Softley. Ultracold molecules and ultracold chemistry. *Mol. Phys.*, 107:99–132, 2009.

[13] P.F. Weck and N. Balakrishnan. Quantum dynamics of the Li+HF←H+LiF reaction at ultralow temperatures. *J. Chem. Phys.*, 122:154309, 2005.

[14] P.F. Weck and N. Balakrishnan. Reactivity enhancement of ultracold $O(^3P)+H_2$ collisions by van der Waals interactions. *J. Chem. Phys.*, 123:144308, 2005.

[15] G. Quéméner and N. Balakrishnan. Cold and ultracold chemical reactions of F+HCl and F+DCl. *J. Chem. Phys.*, 128:224304, 2008.

[16] R.V. Krems. Molecules near absolute zero and external field control of atomic and molecular dynamics. *Int. Rev. Phys. Chem.*, 24:99–118, 2005.

[17] L. Scharfenberg, K.B. Gubbels, M. Kirste, G.C. Groenenboom, A. van der Avoird, G. Meijer, and S.Y.T. van de Meerakker. Scattering of Stark-decelerated OH radicals with rare-gas atoms. *Eur. Phys. J. D*, 65:189–198, 2011.

[18] M. Kirste, X. Wang, C. Schewe, G. Meijer, K. Liu, A. van der Avoird, L.M.C. Janssen, K.B. Gubbels, G.C. Groenenboom, and S.Y.T. van de Meerakker. Quantum-State Resolved Bimolecular Collisions of Velocity-Controlled OH with NO Radicals. *Science*, 338:1060–1063, 2012.

[19] B.C. Sawyer, B.K. Stuhl, D. Wang, M. Yeo, and J. Ye. Molecular Beam Collisions with a Magnetically Trapped Target. *Phys. Rev. Lett.*, 101:203203, 2008.

[20] L.P. Parazzoli, N.J. Fitch, P.S. Żuchowski, J.M. Hutson, and H.J. Lewandowski. Large Effects of Electric Fields on Atom-Molecule Collisions at Millikelvin Temperatures. *Phys. Rev. Lett.*, 106:193201, 2011.

[21] M. Strebel, T.-O. Müller, B. Ruff, F. Stienkemeier, and M. Mudrich. Quantum rainbow scattering at tunable velocities. *Phys. Rev. A*, 86:062711, 2012.

[22] A.B. Henson, S. Gersten, Y. Shagam, J. Narevicius, and E. Narevicius. Observation of Resonances in Penning Ionization Reactions at Sub-Kelvin Temperatures in Merged Beams. *Science*, 338:234–238, 2012.

[23] S. Willitsch, M.T. Bell, A.D. Gingell, S.R. Procter, and T.P. Softley. Cold Reactive Collisions between Laser-Cooled Ions and Velocity-Selected Neutral Molecules. *Phys. Rev. Lett.*, 100:043203, 2008.

[24] A.D. Gingell, M.T. Bell, J.M. Oldham, T.P. Softley, and J.N. Harvey. Cold chemistry with electronically excited Ca^+ Coulomb crystals. *J. Chem. Phys.*, 133:194302, 2010.

[25] F.H.J. Hall and S. Willitsch. Millikelvin Reactive Collisions between Sympathetically Cooled Molecular Ions and Laser-Cooled Atoms in an Ion-Atom Hybrid Trap. *Phys. Rev. Lett.*, 109:233202, 2012.

[26] K. Okada, T. Suganuma, T. Furukawa, T. Takayanagi, M. Wada, and H.A. Schuessler. Cold ion–polar-molecule reactions studied with a combined Stark-velocity-filter–ion-trap apparatus. *Phys. Rev. A*, 87:043427, 2013.

[27] S. Ospelkaus, K.-K. Ni, D. Wang, M.H.G. de Miranda, B. Neyenhuis, G. Quéméner, P.S. Julienne, J.L. Bohn, D.S. Jin, and J. Ye. Quantum-State Controlled Chemical Reactions of Ultracold Potassium-Rubidium Molecules. *Science*, 327:853–857, 2010.

[28] K.-K. Ni, S. Ospelkaus, D. Wang, G. Quéméner, B. Neyenhuis, M.H.G. de Miranda, J.L. Bohn, J. Ye, and D.S. Jin. Dipolar collisions of polar molecules in the quantum regime. *Nature*, 464:1324–1328, 2010.

[29] M.H.G. de Miranda, A. Chotia, B. Neyenhuis, D. Wang, G. Quéméner, S. Ospelkaus, J. L. Bohn, J. Ye, and D.S. Jin. Controlling the quantum stereodynamics of ultracold bimolecular reactions. *Nat. Phys.*, 7:502–507, 2011.

[30] D. DeMille. Quantum Computation with Trapped Polar Molecules. *Phys. Rev. Lett.*, 88:067901, 2002.

[31] M. Ortner, Y.L. Zhou, P. Rabl, and P. Zoller. Quantum information processing in self-assembled crystals of cold polar molecules. *Quant. Inf. Proc.*, 10:793–829, 2011.

[32] A. André, D. DeMille, J.M. Doyle, M.D. Lukin, S.E. Maxwell, P. Rabl, R.J. Schoelkopf, and P. Zoller. A coherent all-electrical interface between polar molecules and mesoscopic superconducting resonators. *Nature Phys.*, 2:636–642, 2006.

[33] P. Rabl, D. DeMille, J.M. Doyle, M.D. Lukin, R.J. Schoelkopf, and P. Zoller. Hybrid Quantum Processors: Molecular Ensembles as Quantum Memory for Solid State Circuits. *Phys. Rev. Lett.*, 97:033003, 2006.

[34] D.I. Schuster, L.S. Bishop, I.L. Chuang, D. DeMille, and R.J. Schoelkopf. Cavity QED in a molecular ion trap. *Phys. Rev. A*, 83:012311, 2011.

[35] C.M. Tesch and R. de Vivie-Riedle. Quantum Computation with Vibrationally Excited Molecules. *Phys. Rev. Lett.*, 89:157901, 2002.

[36] K. Hosaka, H. Shimada, H. Chiba, H. Katsuki, Y. Teranishi, Y. Ohtsuki, and K. Ohmori. Ultrafast Fourier Transform with a Femtosecond-Laser-Driven Molecule. *Phys. Rev. Lett.*, 104:180501, 2010.

[37] Q. Wei, S. Kais, B. Friedrich, and D. Herschbach. Entanglement of polar symmetric top molecules as candidate qubits. *J. Chem. Phys.*, 135:154102, 2011.

[38] N. Hinkley, J.A. Sherman, N.B. Phillips, M. Schioppo, N.D. Lemke, K. Beloy, M. Pizzocaro, C.W. Oates, and A.D. Ludlow. An Atomic Clock with 10^{-18} Instability. *Science*, 2013.

[39] E.D. Commins. Electric Dipole Moments of Leptons. *Adv. At., Mol., Opt. Phys.*, 40:1–55, 1999.

[40] B.C. Regan, E.D. Commins, C.J. Schmidt, and D. DeMille. New Limit on the Electron Electric Dipole Moment. *Phys. Rev. Lett.*, 88:071805, 2002.

[41] E.A. Hinds. Testing Time Reversal Symmetry Using Molecules. *Phys. Scr.*, T70:34, 1997.

[42] D. DeMille, F. Bay, S. Bickman, D. Kawall, L. Hunter, Jr. D. Krause, S. Maxwell, and K. Ulmer. Search for the electric dipole moment of the electron using metastable PbO. *AIP Conf. Proc.*, 596:72–83, 2001.

[43] J.J. Hudson, B.E. Sauer, M.R. Tarbutt, and E.A. Hinds. Measurement of the Electron Electric Dipole Moment Using YbF Molecules. *Phys. Rev. Lett.*, 89:023003, 2002.

[44] J.J. Hudson, D.M. Kara, I.J. Smallman, B.E. Sauer, M.R. Tarbutt, and E.A. Hinds. Improved measurement of the shape of the electron. *Nature*, 473:493–496, 2011.

[45] M.R. Tarbutt, B.E. Sauer, J.J. Hudson, and E.A. Hinds. Design for a fountain of YbF molecules to measure the electron's electric dipole moment. *New J. Phys.*, 15:053034, 2013.

[46] W.C. Campbell, C. Chan, D. DeMille, J.M. Doyle, G. Gabrielse, Y.V. Gurevich, P.W. Hess, N.R. Hutzler, E. Kirilov, B. O'Leary, E.S. Petrik, B. Spaun, and A.C. Vutha. Advanced cold molecule electron EDM. *Eur. Phys. J. Web Conf.*, 57:02004, 2013.

[47] A. Fioretti, D. Comparat, A. Crubellier, O. Dulieu, F. Masnou-Seeuws, and P. Pillet. Formation of Cold Cs_2 Molecules through Photoassociation. *Phys. Rev. Lett.*, 80:4402–4405, 1998.

[48] K.K. Ni, S. Ospelkaus, M.H.G. de Miranda, A. Pe'er, B. Neyenhuis, J.J. Zirbel, S. Kotochigova, P.S. Julienne, D.S. Jin, and J. Ye. A high phase-space-density gas of polar molecules. *Science*, 322:231–235, 2008.

[49] M. Viteau, A. Chotia, M. Allegrini, N. Bouloufa, O. Dulieu, D. Comparat, and P. Pillet. Optical Pumping and Vibrational Cooling of Molecules. *Science*, 321:232–234, 2008.

[50] I. Manai, R. Horchani, H. Lignier, P. Pillet, D. Comparat, A. Fioretti, and M. Allegrini. Rovibrational Cooling of Molecules by Optical Pumping. *Phys. Rev. Lett.*, 109:183001, 2012.

[51] S.A. Rangwala, T. Junglen, T. Rieger, P.W.H. Pinkse, and G. Rempe. Continuous source of translationally cold dipolar molecules. *Phys. Rev. A*, 67:043406, 2003.

[52] M. Motsch, C. Sommer, M. Zeppenfeld, L.D. van Buuren, P.W.H. Pinkse, and G. Rempe. Collisional effects in the formation of cold guided beams of polar molecules. *New J. Phys.*, 11:055030, 2009.

[53] M. Motsch, M. Schenk, L. D. van Buuren, M. Zeppenfeld, P. W. H. Pinkse, and G. Rempe. Internal-state thermometry by depletion spectroscopy in a cold guided beam of formaldehyde. *Phys. Rev. A*, 76:061402(R), 2007.

[54] B. Bertsche and A. Osterwalder. State-selective detection of velocity-filtered ND_3 molecules. *Phys. Rev. A*, 82:033418, 2010.

[55] J.D. Weinstein, R. DeCarvalho, T. Guillet, B. Friedrich, and J.M. Doyle. Magnetic trapping of calcium monohydride molecules at millikelvin temperatures. *Nature*, 395:148–150, 1998.

[56] S.E. Maxwell, N. Brahms, R. deCarvalho, D.R. Glenn, J.S. Helton, S. V. Nguyen, D. Patterson, J. Petricka, D. DeMille, and J.M. Doyle. High-Flux Beam Source for Cold, Slow Atoms or Molecules. *Phys. Rev. Lett.*, 95:173201, 2005.

[57] D. Patterson and J.M. Doyle. Bright, guided molecular beam with hydrodynamic enhancement. *J. Chem. Phys.*, 126:154307, 2007.

[58] L.D. van Buuren, C. Sommer, M. Motsch, S. Pohle, M. Schenk, J. Bayerl, P.W.H. Pinkse, and G. Rempe. Electrostatic Extraction of Cold Molecules from a Cryogenic Reservoir. *Phys. Rev. Lett.*, 102:033001, 2009.

[59] H.L. Bethlem, G. Berden, and G. Meijer. Decelerating Neutral Dipolar Molecules. *Phys. Rev. Lett.*, 83:1558–1561, 1999.

[60] E. Narevicius, A. Libson, C.G. Parthey, I. Chavez, J. Narevicius, U. Even, and M.G. Raizen. Stopping supersonic oxygen with a series of pulsed electromagnetic coils: A molecular coilgun. *Phys. Rev. A*, 77:051401(R), 2008.

[61] A.W. Wiederkehr, H. Schmutz, M. Motsch, and F. Merkt. Velocity-tunable slow beams of cold O_2 in a single spin-rovibronic state with full angular-momentum orientation by multistage Zeeman deceleration. *Mol. Phys.*, 110:1807–1814, 2012.

[62] R. Fulton, A.I. Bishop, and P.F. Barker. Optical Stark Decelerator for Molecules. *Phys. Rev. Lett.*, 93:243004, 2004.

[63] S. Merz, N. Vanhaecke, W. Jäger, M. Schnell, and G. Meijer. Decelerating molecules with microwave fields. *Phys. Rev. A*, 85:063411, 2012.

[64] M. Gupta and D. Herschbach. A Mechanical Means to Produce Intense Beams of Slow Molecules. *J. Phys. Chem. A*, 103:10670–10673, 1999.

[65] M. Strebel, F. Stienkemeier, and M. Mudrich. Improved setup for producing slow beams of cold molecules using a rotating nozzle. *Phys. Rev. A*, 81:033409, 2010.

[66] S. Chervenkov, X. Wu, J. Bayerl, A. Rohlfes, T. Gantner, M. Zeppenfeld, and G. Rempe. A Continuous Centrifuge Decelerator for Polar Molecules. *Submitted for publication*, 2013.

[67] B.K. Stuhl, M.T. Hummon, M. Yeo, G. Quéméner, J.L. Bohn, and J. Ye. Evaporative cooling of the dipolar hydroxyl radical. *Nature*, 492:396–400, 2012.

[68] J.T. Bahns, W.C. Stwalley, and P.L. Gould. Laser cooling of molecules: A sequential scheme for rotation, translation, and vibration. *J. Chem. Phys.*, 104:9689, 1996.

[69] M. Weitz and T.W. Hänsch. Frequency-independent laser cooling based on interferometry. *Europhys. Lett.*, 49:302, 2000.

[70] V. Vuletić and S. Chu. Laser Cooling of Atoms, Ions, or Molecules by Coherent Scattering. *Phys. Rev. Lett.*, 84:3787, 2000.

[71] M. Kowalewski, G. Morigi, P.W.H. Pinkse, and R. de Vivie-Riedle. Cavity sideband cooling of trapped molecules. *Phys. Rev. A*, 84:033408, 2011.

[72] I.S. Averbukh and Y. Prior. Laser Cooling in an Optical Shaker. *Phys. Rev. Lett.*, 94:153002, 2005.

[73] E.S. Shuman, J.F. Barry, and D. DeMille. Laser cooling of a diatomic molecule. *Nature*, 467:820–823, 2010.

[74] J.F. Barry, E.S. Shuman, E.B. Norrgard, and D. DeMille. Laser Radiation Pressure Slowing of a Molecular Beam. *Phys. Rev. Lett.*, 108:103002, 2012.

[75] D.E. Pritchard. Cooling Neutral Atoms in a Magnetic Trap for Precision Spectroscopy. *Phys. Rev. Lett.*, 51:1336–1339, 1983.

[76] M. Zeppenfeld, M. Motsch, P.W.H. Pinkse, and G. Rempe. Opto-Electrical Cooling of Polar Molecules. *Phys. Rev. A*, 80:041401(R), 2009.

[77] F. Robicheaux. A proposal for laser cooling of OH molecules. *J. Phys. B*, 42:195301, 2009.

[78] S.Y.T. van de Meerakker, R.T. Jongma, H.L. Bethlem, and G. Meijer. Accumulating NH radicals in a magnetic trap. *Phys. Rev. A*, 64:041401(R), 2001.

[79] J. Riedel, S. Hoekstra, W. Jäger, J.J. Gilijamseand S.Y.T. van de Meerakker, and G. Meijer. Accumulation of Stark-decelerated NH molecules in a magnetic trap. *Eur. Phys. J. D*, 65:161–166, 2011.

[80] E. Narevicius, S.T. Bannerman, and M.G. Raizen. Single-photon molecular cooling. *New J. Phys.*, 11:055046, 2009.

[81] C.H.R. Ooi, K.-P. Marzlin, and J. Audretsch. Laser cooling of molecules via single spontaneous emission. *Eur. Phys. J. D*, 22:259–267, 2003.

[82] M. Zeppenfeld, B.G.U. Englert, R. Glöckner, A. Prehn, M. Mielenz, C. Sommer, L.D. van Buuren, M. Motsch, and G. Rempe. Sisyphus cooling of electrically trapped polyatomic molecules. *Nature*, 491:570–573, 2012.

[83] B.G.U. Englert, M. Mielenz, C. Sommer, J. Bayerl, M. Motsch, P.W.H. Pinkse, G. Rempe, and M. Zeppenfeld. Storage and Adiabatic Cooling of Polar Molecules in a Microstructured Trap. *Phys. Rev. Lett.*, 107:263003, 2011.

[84] J. van Veldhoven, J. Küpper, H.L. Bethlem, B. Sartakov, A.J.A. van Roij, and G. Meijer. Decelerated molecular beams for high-resolution spectroscopy. *Eur. Phys. J. D*, 31:337–349, 2004.

[85] S. Gerlich, L. Hackermüller, K. Hornberger, A. Stibor, H. Ulbricht, M. Gring, F. Goldfarb, T. Savas, M. Müri, M. Mayor, and M. Arndt. A Kapitza-Dirac-Talbot-Lau interferometer for highly polarizable molecules. *Nat. Phys.*, 3:711–715, 2007.

[86] M. Baranov, Ł. Dobrek, K. Góral, L. Santos, and M. Lewenstein. Ultracold Dipolar Gases – a Challenge for Experiments and Theory. *Phys. Scr.*, T102:74, 2002.

[87] A. Micheli, G.K. Brennen, and P. Zoller. A toolbox for lattice-spin models with polar molecules. *Nature Phys.*, 2:341–347, 2006.

[88] H.J. Metcalf and P. van der Straten. *Laser Cooling and Trapping*. Springer, Berlin, 1999.

[89] H.L. Bethlem, G. Berden, F.M.H. Crompvoets, R.T. Jongma, A.J.A. van Roij, and G. Meijer. Electrostatic trapping of ammonia molecules. *Nature*, 406:491–494, 2000.

[90] T. Rieger, T. Junglen, S.A. Rangwala, P.W.H. Pinkse, and G. Rempe. Continuous loading of an electrostatic trap for polar molecules. *Phys. Rev. Lett.*, 95:173002, 2005.

[91] J. Söding, R. Grimm, and Y.B. Ovchinnikov. Gravitational laser trap for atoms with evanescent-wave cooling. *Opt. Commun.*, 119:652–662, 1995.

[92] G.N. Price, S.T. Bannerman, K. Viering, E. Narevicius, and M.G. Raizen. Single-Photon Atomic Cooling. *Phys. Rev. Lett.*, 100:093004, 2008.

[93] S.J. Wark and G.I. Opat. An electrostatic mirror for neutral polar molecules. *J. Phys. B*, 25:4229, 1992.

[94] D.R. Lide, editor. *CRC Handbook of Chemistry and Physics*. CRC Press, Boca Raton, FL, 71st edition, 1990.

[95] M.E. Jacox. "Vibrational and Electronic Energy Levels of Polyatomic Transient Molecules" in NIST Chemistry WebBook. `http://webbook.nist.gov`.

[96] M.J. Frisch *et. al.* Gaussian 03, Revision B.03. Gaussian, Inc., Pittsburgh PA, 2003.

[97] W. Gordy and R.L. Cook. *Microwave Molecular Spectra*. John Wiley & Sons Inc, 1984.

[98] M. Kirste, B.G. Sartakov, M. Schnell, and G. Meijer. Nonadiabatic transitions in electrostatically trapped ammonia molecules. *Phys. Rev. A*, 79:051401(R), 2009.

[99] S. Hoekstra, J.J. Gilijamse, B. Sartakov, N. Vanhaecke, L. Scharfenberg, S.Y.T. van de Meerakker, and G. Meijer. Optical Pumping of Trapped Neutral Molecules by Blackbody Radiation. *Phys. Rev. Lett.*, 98:133001, 2007.

[100] T. Junglen, T. Rieger, S.A. Rangwala, P.W.H. Pinkse, and G. Rempe. Slow ammonia molecules in an electrostatic quadrupole guide. *Eur. Phys. J. D*, 31:365–373, 2004.

[101] M.H. Anderson, W. Petrich, J.R. Ensher, and E.A. Cornell. Reduction of light-assisted collisional loss rate from a low-pressure vapor-cell trap. *Phys. Rev. A*, 50:R3597–R3600, 1994.

[102] K.M. O'Hara, S.R. Granade, M.E. Gehm, T.A. Savard, S. Bali, C. Freed, and J.E. Thomas. Ultrastable CO_2 Laser Trapping of Lithium Fermions. *Phys. Rev. Lett.*, 82:4204–4207, 1999.

[103] P.A. Willems and K.G. Libbrecht. Creating long-lived neutral-atom traps in a cryogenic environment. *Phys. Rev. A*, 51:1403–1406, 1995.

[104] J.E. Bjorkholm. Collision-limited lifetimes of atomic traps. *Phys. Rev. A*, 38:1599, 1988.

[105] C.R. Monroe, E.A. Cornell, C.A. Sackett, C.F. Myatt, and C.E. Wieman. Measurement of Cs-Cs Elastic Scattering at T=30μK. *Phys. Rev. Lett.*, 70:414, 1993.

[106] S. Bali, K.M. O'Hara, M.E. Gehm, S.R. Granade, and J.E. Thomas. Quantum-diffractive background gas collisions in atom-trap heating and loss. *Phys. Rev. A*, 60:R29, 1999.

[107] H.C.W. Beijerinck. Rigorous calculation of heating in alkali-metal traps by background gas collisions. *Phys. Rev. A*, 61:033606, 2000.

[108] T.A. Savard, K.M. O'Hara, and J.E. Thomas. Laser-noise-induced heating in far-off resonance optical traps. *Phys. Rev. A*, 56:R1095, 1997.

[109] C. Henkel and M. Wilkens. Heating of trapped atoms near thermal surfaces. *Europhys. Lett.*, 47:414, 1999.

[110] J.W. Russell, C.D. Needham, and J. Overend. Vibrational Intensities. XV. Error Treatment and Its Application to the Methyl Halides. *J. Chem. Phys.*, 45:3383, 1966.

[111] S.Y. Buhmann, M.R. Tarbutt, S. Scheel, and E.A. Hinds. Surface-induced heating of cold polar molecules. *Phys. Rev. A*, 78:052901, 2008.

[112] J. D. Jackson. *Classical Electrodynamics*. John Wiley & Sons, Inc., third edition, 1998.

[113] I.N. Sneddon. *Mixed boundary value problems in potential theory*. Wiley, 1966.

[114] R.C. Peach. A General Approach to the Electrostatic Problem of the SAW Interdigital Transducer. *IEEE Trans. Sonics and Ultrasonics*, 28:96–104, 1981.

[115] S.V. Biryukov and V.G. Polevoi. The electrostatic problem for the SAW interdigital transducers in an external electric field. I. A general solution for a limited number of electrodes. *IEEE Trans. Ultrason., Ferroel., and Freq. Ctrl.*, 43:1150–1159, 1996.

[116] K. Góral, L. Santos, and M. Lewenstein. Quantum Phases of Dipolar Bosons in Optical Lattices. *Phys. Rev. Lett.*, 88:170406, 2002.

[117] P.S. Żuchowski and J.M. Hutson. Low-energy collisions of NH_3 and ND_3 with ultracold Rb atoms. *Phys. Rev. A*, 79:062708, 2009.

[118] C. Sommer., L.D. van Buuren, M. Motsch, S. Pohle, J. Bayerl, P.W.H. Pinkse, and G. Rempe. Continuous guided beams of slow and internally cold polar molecules. *Faraday Discuss.*, 142:203–220, 2009.

[119] M. Motsch, M. Zeppenfeld, P.W.H. Pinkse, and G. Rempe. Cavity-enhanced Rayleigh scattering. *New J. Phys.*, 12:063022, 2010.

[120] D. Nagy, J.K. Asbóth, P. Domokos, and H. Ritsch. Self-organization of a laser-driven cold gas in a ring cavity. *Europhys. Lett.*, 74:254–260, 2006.

[121] M. Zeppenfeld and P.W.H. Pinkse. Calculating the fine structure of a Fabry-Perot resonator using spheroidal wave functions. *Opt. Expr.*, 18:9580–9591, 2010.

[122] A. Xuereb, P. Domokos, P. Horak, and T. Freegarde. Cavity cooling of atoms: within and without a cavity. *Eur. Phys. J. D*, 65:273–278, 2011.

[123] M. Lara, J. Bohn, D. Potter, P. Soldán, and J.M. Hutson. Ultracold Rb-OH Collisions and Prospects for Sympathetic Cooling. *Phys. Rev. Lett.*, 97:183201, 2006.

[124] D. DeMille, D.R. Glenn, and J. Petricka. Microwave traps for cold polar molecules. *Eur. Phys. J. D*, 31:375–384, 2004.

[125] G. Graner and G. Guelachvili. Extensive high-resolution study of the crowded rovibrational CH_3F spectrum around $3000\,cm^{-1}$. *J. Mol. Spec.*, 89:19–41, 1981.

[126] J.H. Newton and W.B. Person. Dipole moment derivatives and infrared intensities. II. Polar tensors in methyl halide molecules. *The Journal of Chemical Physics*, 64:3036, 1976.

[127] P.F. Staanum, K. Højbjerre, P.S. Skyt, A.K. Hansen, and M. Drewsen. Rotational laser cooling of vibrationally and translationally cold molecular ions. *Nat. Phys.*, 6:271–274, 2010.

[128] T. Schneider, B. Roth, H. Duncker, I. Ernsting, and S. Schiller. All-optical preparation of molecular ions in the rovibrational ground state. *Nat. Phys.*, 6:275–278, 2010.